NASA Contractor Report 3003

Validation of Scramjet Exhaust Simulation Technique at Mach 6

H. B. Hopkins, W. Konopka,
and J. Leng

NASA

NASA Contractor Report 3003

Validation of Scramjet Exhaust Simulation Technique at Mach 6

H. B. Hopkins, W. Konopka,
and J. Leng
Grumman Aerospace Corporation
Bethpage, New York

NASA

National Aeronautics
and Space Administration

Scientific and Technical
Information Office

1979

TABLE OF CONTENTS

LIST OF ILLUSTRATIONS

LIST OF ILLUSTRATIONS (Cont)

LIST OF TABLES

SYMBOLS

Ar   argon atom

a   sound speed

Br   bromine atom

C   carbon atom

C_p specific heat at constant pressure

C_v specific heat at constant volume

F   fluorine atom

Freon 12   dichlorodifluoromethane (CCl_2F_2)

Freon 13B1 bromotrifluoromethane ($CBrF_3$)

H   enthalpy; also hydrogen atom

h   static enthalpy

K   Kelvin temperature scale, also relaminarization parameter

k   prefix "kilo" (10^3)

M   Mach number ($\equiv U/a$)

M-O-C   method of characteristics

m   unit of length (meter); also prefix "milli" (10^{-3})

N   nitrogen atom; also unit of force (Newton)

O   oxygen atom

P   pressure

Q   heat transfer rate

R   specific gas constant

R_e Reynolds number ($= \dfrac{\rho U X}{\mu}$)

T   temperature

U   velocity

X	distance measured along detonation tube and combustor axis (vehicle roll axis); also mole fraction of a chemical specie
$\overline{X}$	nondimensional distance ($\equiv X/Y_3$)
Y	vehicle yaw axis
$\overline{Y}$	nondimensional distance ($\equiv Y/Y_3$)
Z	vehicle pitch axis
α	angle of attack
β	inlet ramp angle
γ	ratio of specific heats, c_p/c_v
θ	flow angle relative to X axis
μ	prefix "micro" (10^{-6}), also viscosity
ν	kinematic viscosity
ρ	density
ϕ	equivalence ratio

Subscripts

o	refers to total (stagnation) condition
1	refers to an arbitrary thermodynamic state point; also initial, unburned gas conditions in driven tube
2	refers to an arbitrary thermodynamic state point
3	refers to combustor exit plane
4	refers to unexpanded, high pressure driver gas
5	refers to stagnation condition or region behind reflected shock wave in detonation tube
∞	refers to undisturbed free stream
i	refers to i^{th} chemical specie; also internal flow
T_1	total or stagnation conditions upstream of a shock wave
T_2	total or stagnation conditions downstream of a shock wave

1. INTRODUCTION AND SUMMARY

Current design philosophy for hydrogen-fueled, scramjet-powered hypersonic aircraft results in configurations with strong couplings between the engine plume and vehicle aerodynamics. As seen in the sketch below, the aft portion of the vehicle will be utilized as the expansion nozzle for the scramjet, and the resulting exhaust gas impingement will play a major role in determining the aerodynamic forces and mements on the vehicle. In order to assess the impingement effects during wind tunnel experiments, the correct thermodynamics as well as aerodynamics of the exhaust gases must be reproduced.
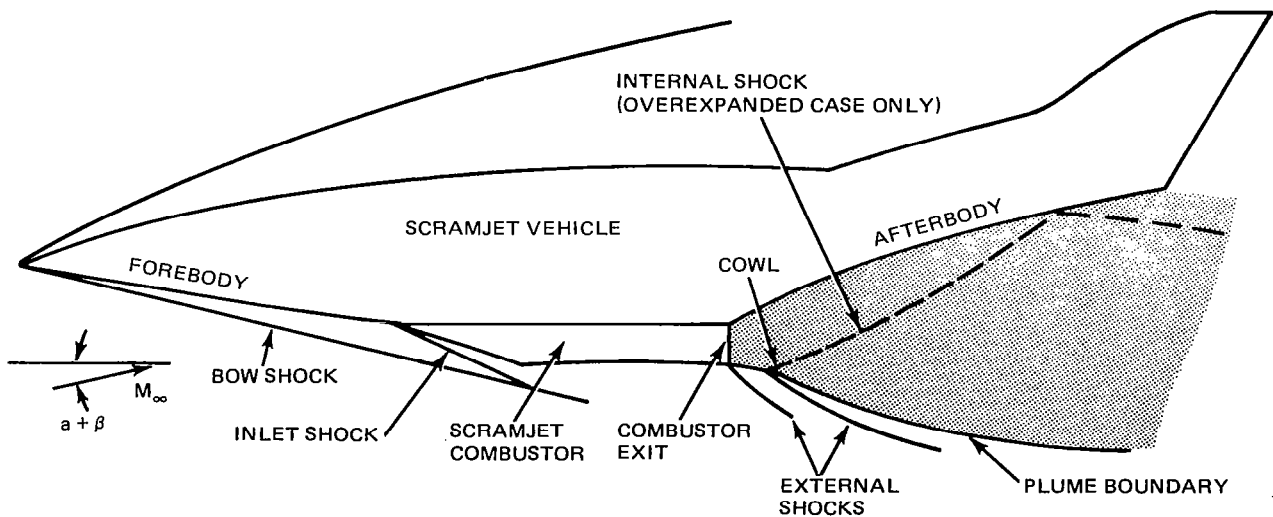
The method of using the detonation tube simulator to achieve a near exact simulation of the exhaust plume to validate cool substitute gases with properties that would allow them to behave in a manner similar to the real reacting engine exhaust is discussed in Ref. 1. This concept was shown to be valid for the Mach 8 flight case in Ref. 2. Present research has extended the proof of concept to the Mach 6 flight case, and has obtained data to provide a "bench mark" for comparison of theoretical methods currently under development (Ref. 3).

This report describes the Mach 6 experiments and associated analysis. Pressure and heat transfer measurements were obtained over a simulated cowl, and over an afterbody inclined at both 0 and 20° to the exit nozzle centerline. Scramjet combustor exit plane conditions were duplicated for the Mach 6 case, and results were compared with those obtained for a substitute gas mixture of 50% Argon and 50% Freon 13B1. Shock waves were purposely introduced into the exit flow for some runs by placing wedges at the cowl exit and nozzle sidewall. Time exposure glow photographs were obtained of the shock wave locations.

Results were excellent. For the shock-free flows the normalized pressure distributions obtained in the combustion flow are in almost exact agreement with those obtained in the substitute gas flow and with two-dimensional method of characteristics calculations where such comparisons were valid. In the cases for which strong shock waves were introduced into the flows the agreement among combustion gas, substitute gas, and calculations was very good, although the shock wave from the cowl in the substitute gas flow appears to impinge on the afterbody slightly upstream of the combustion gas impingement point. Heat transfer measurements indicate a turbulent boundary layer exists over the afterbody with very high heating rates in the region of the nozzle exit plane. In our previous tests at $M_{\infty} = 8$ (Ref. 2) heat transfer measurements indicated the boundary layer was laminar.

To study further some of the phenomena associated with the Mach 6 flight condition, an extension was granted to the original contract for "Validation of Scramjet Exhaust Simulation Technique at Mach 6". The extension had two objectives. The first objective was to examine theoretically and experimentally the effects of different substitute gas mixtures on the impingement location of a shock wave propagating across

the exhaust flow field. The calculated impingement location for various substitute mixtures showed very little effect of gas composition. The constancy of shock location was verified by experiment with one substitute gas composed of Freon 12 and Argon.

The other objective was to examine, by experiment, the influence on afterbody heating rate distributions of simulated combustion nozzle separators. The experiments were made using both the substitute and combustion gases for various separator positions. The results of these experiments show a wake structure which increases the heating rate by approximately 40% over the local heating rate without the separator. This result is consistent for both gases but is only evident for $\overline{X}$ greater than .78, since for more upstream locations the wake is too narrow relative to the spatial resolution of the instrumentation.

Use of commercial products or names of manufacturers in this report does not constitute official endorsement of such products or manufacturers, either expressed or implied, by the National Aeronautics and Space Administration.

2. DETONATION TUBE SIMULATOR

The Grumman detonation tube simulator used for the measurement of exhaust flows is capable of giving nearly correct chemistry and total enthalpy for the hydrogen/air combustion system throughout the hypersonic cruise flight regime (Ref. 1). Reynolds numbers can easily be maintained at flight values by running at elevated pressures with both combustion and substitute gases. A schematic of the detonation tube facility is shown in Fig. 1. It consists of a 6.1 meter long, 7.62 cm inside diameter driver section initially separated by a metallic diaphragm from a 10 meter long, 12.7 cm inside diameter driven tube. The driven tube is terminated by a supersonic nozzle designed to produce a flow that will match the expected exit plane conditions of the proposed scramjet engine. The nozzle exhausts into a 1.83 meter diameter, 3.66 meter long test section. The test section can be evacuated prior to a run to any desired pressure down to 5×10^{-5} torr*. The facility has been designed to handle combustible hydrogen mixtures safely. Various interlocks and leak detection devices are incorporated into the automatic gas handling system. Details of this system may be found in Ref. 4. A photograph of the facility is shown in Fig. 2.

Mounted within the test section and mated to the supersonic nozzle is the model afterbody. The present experiments were carried out on two different configurations,

---

* 1 torr. = 133.3 Pa

DRIVER TUBE

DOUBLE
DIAPHRAGM
STATION

DRIVEN TUBE

VACUUM
GATE VALVE

NOZZLE

MODEL

WINDOWS

VACUUM SYSTEM

1.52m

2.13m

6.1m

10.1m

TRACKS
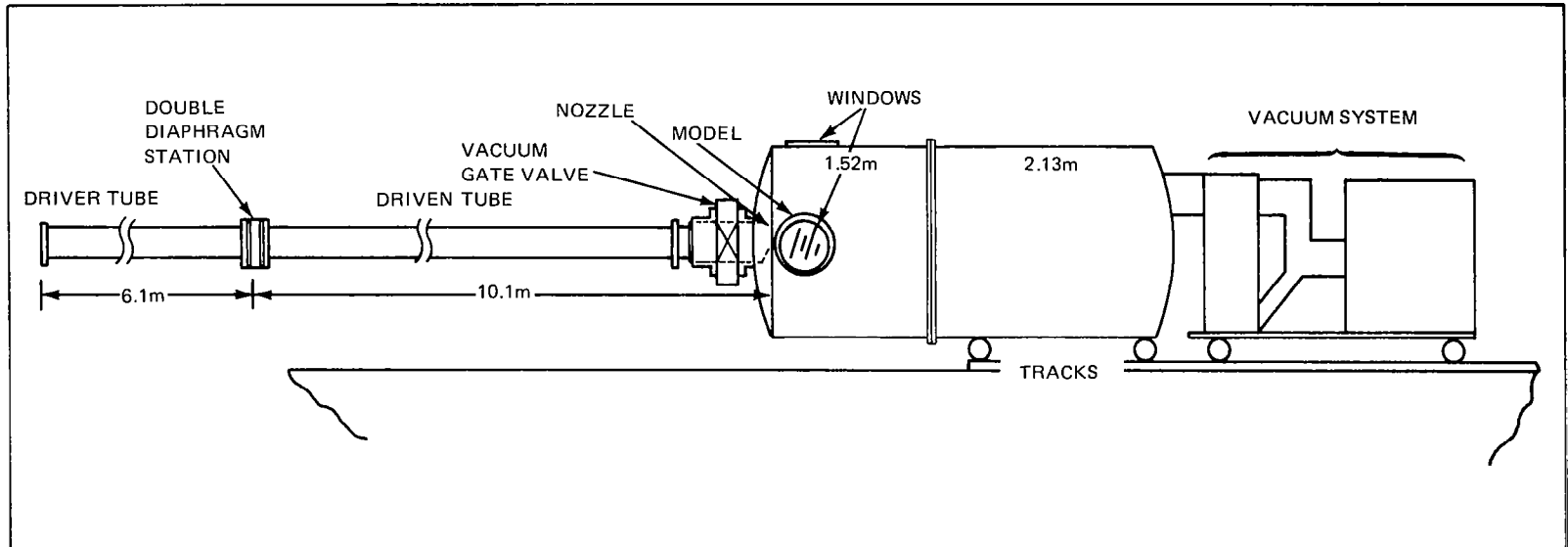
Fig. 1 Detonation Tube Simulator Schematic

4
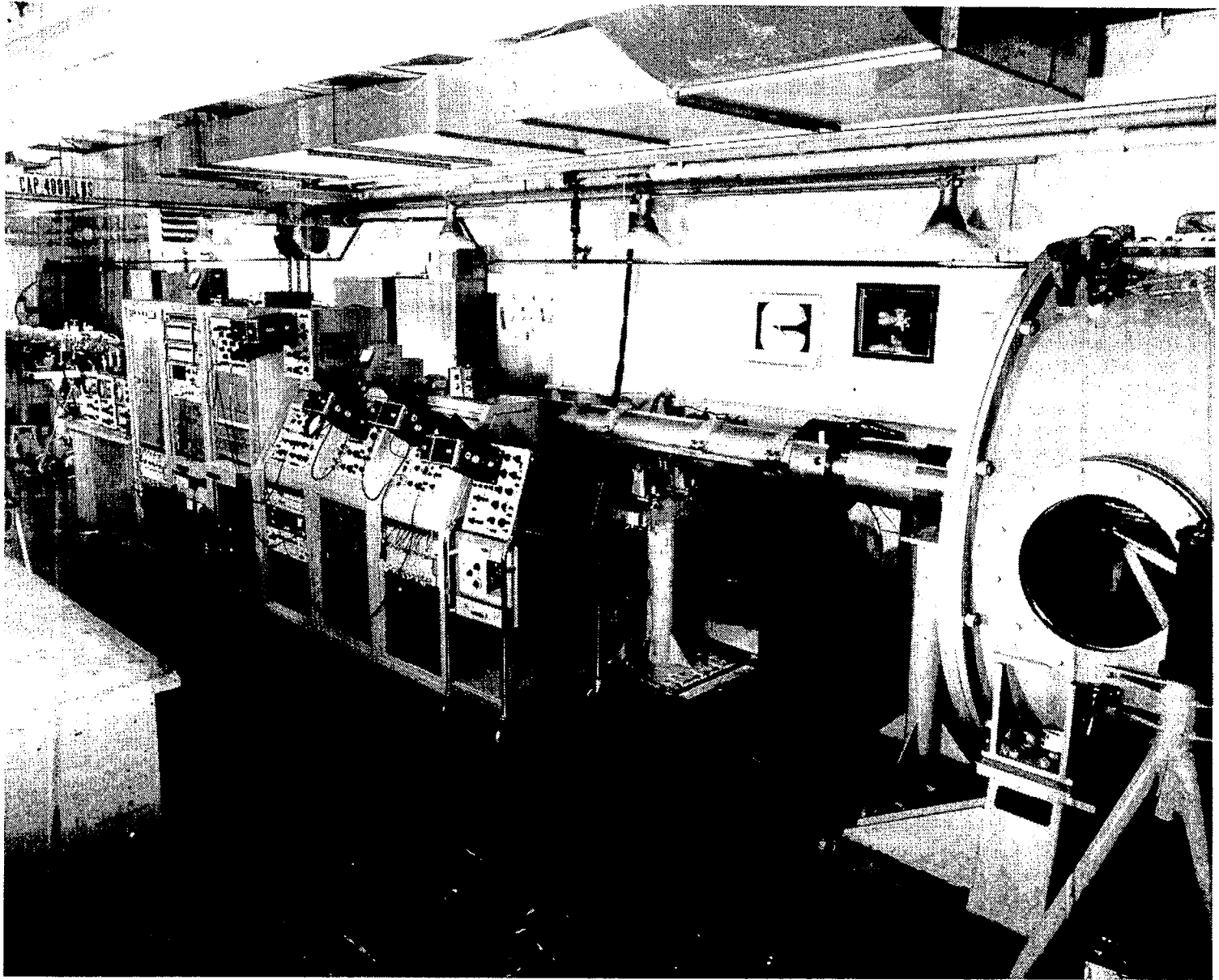
Fig. 2 Photograph of Detonation Tube Simulator

a 20° afterbody surface and a 0° afterbody surface. For each configuration 1/20 scale pressure and heat transfer models were constructed. Details of the models are given in Figs. 3 through 12. The backward-running detonation technique was used exclusively for the current experiments. This technique was developed specifically for the simulation of hydrogen/oxygen rocket engine plumes and is described in detail in Refs. 1 and 4. The running conditions for the present tests are given in Table 4.

For running the inert substitute gases in the detonation tube we run the facility as a conventional reflected shock tunnel, as described in Ref. 2. The stagnation conditions of the substitute gas are determined by the strength of the incident shock wave and the initial pressure in the driven tube, both of which may be easily controlled. The stagnation conditions are given in Table 5 herein.

DETONATION TUBE/COMBUSTOR NOZZLE DESIGN

To duplicate the exit flow of the scramjet combustor in the detonation tube facility, a two-dimensional supersonic nozzle was employed. The Mach number of the supersonic combustion ramjet (SCRJ) exhaust gas at the combustor exit plane for the $M_\infty = 6$ flight condition is quite low (≈ 1.7, see Table 2, Ref. 1). This means the throat-to-exit plane area ratios of the detonation tube combustor nozzle must be small (≈ 1.4). Because the throat area of the detonation tube nozzle cannot exceed approximately 10% of cross-sectional area of the detonation tube, the nozzle and consequently the scale of the afterbody model involved also must be about 1/20 scale, in contrast to the 1/8 scale experiments at $M_\infty = 8$ of Ref. 2. Our nozzle was designed to duplicate the nozzle and model being constructed for substitute gas experiments at NASA Langley Research Center so that the two test programs would be directly comparable. Nozzle coordinates were supplied to us by Langley personnel and are listed in Fig. 3 together with a drawing of the nozzle contour. Since this nozzle was designed for a substitute gas mixture of 50% Freon 13B1 and 50% Argon, we checked its suitability for use with combustion gas. We calculated the flow field through the nozzle using the M-O-C computer program of Ref. 5 with detonation tube combustion gas properties generated by the computer program of Ref. 6. The difference in the nozzle exit plane Mach number distribution between the substitute gas and combustion was insignificant.

NOTE: DIMENSIONS IN CENTIMETERS
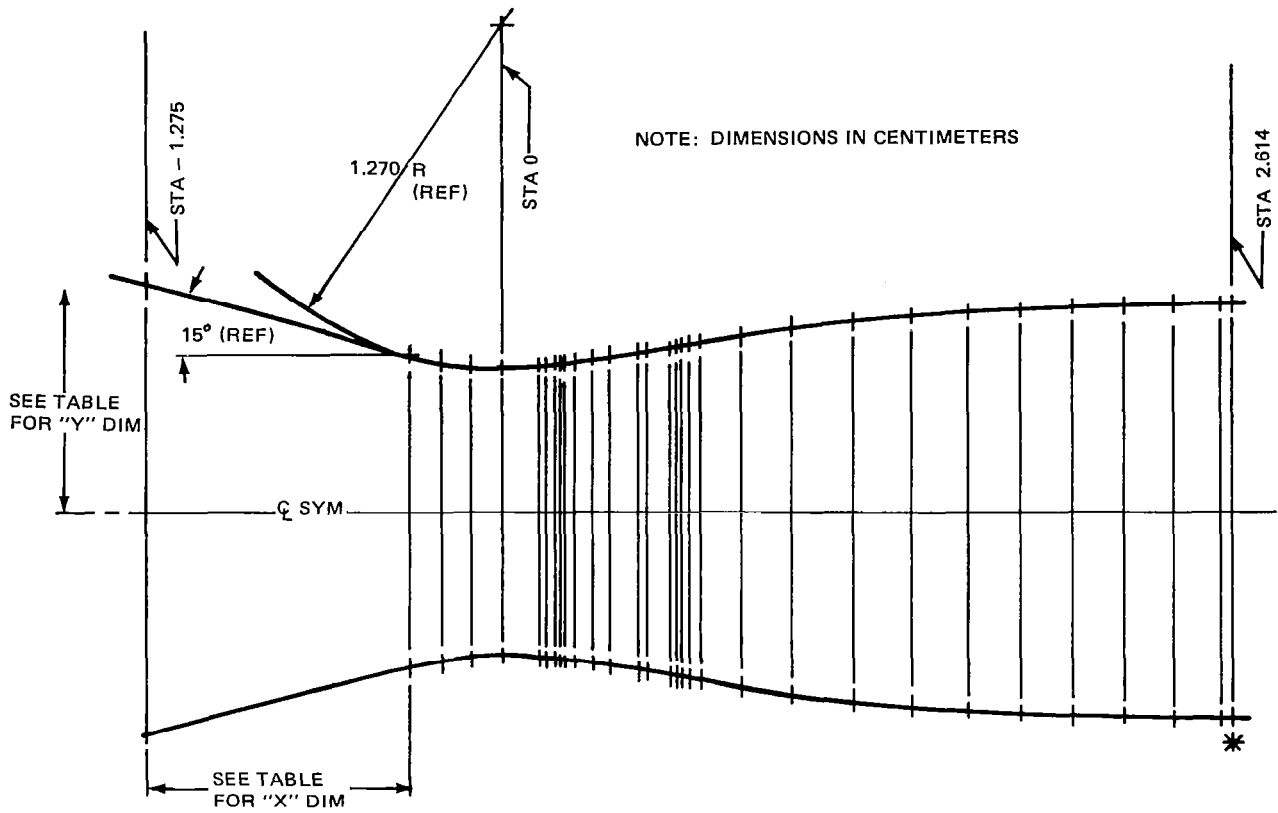
X(cm)	Y(cm)	X(cm)	Y(cm)	X(cm)	Y(cm)
-1.2751	.8344	.2558	.5621	.8552	.6515
- .3287	.5809	.3205	.5702	1.0345	.6749
- .2205	.5570	.3820	.5786	1.2494	.6985
- .1107	.5425	.4813	.5933	1.4628	.7178
0	.5377	.5100	.5977	1.6612	.7323
.1267	.5484	.6012	.6121	1.8487	.7432
.1511	.5507	.6210	.6154	2.0361	.7516
.1824	.5537	.6408	.6187	2.2200	.7572
.2007	.5558	.6713	.6236	2.3973	.7605
.2177	.5575	.7094	.6297	2.5646	.7620
				2.6142	.7620

Fig. 3 Two-Dimensional Contoured Nozzle for Simulating M_∞ = 6 SCRJ Exhaust Flow

7

$\math{C_L}$ NOZZLE

$\math{C_L}$ NOZZLE

0° POSITION/AFTERBODY MODEL

20° POSITION/AFTERBODY MODEL
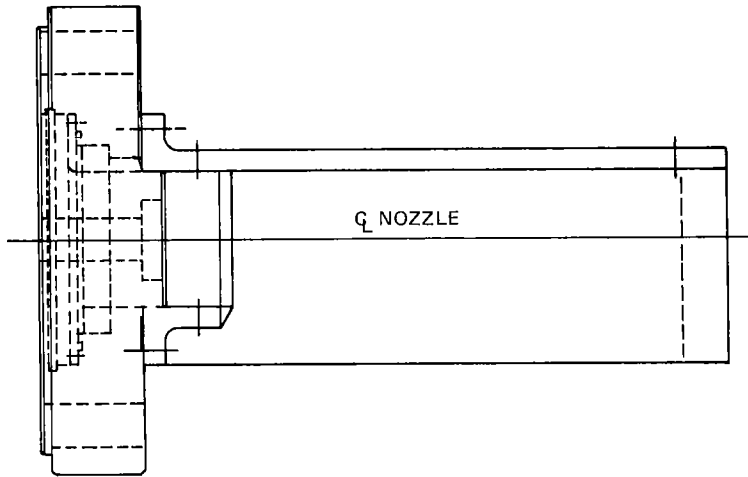
8
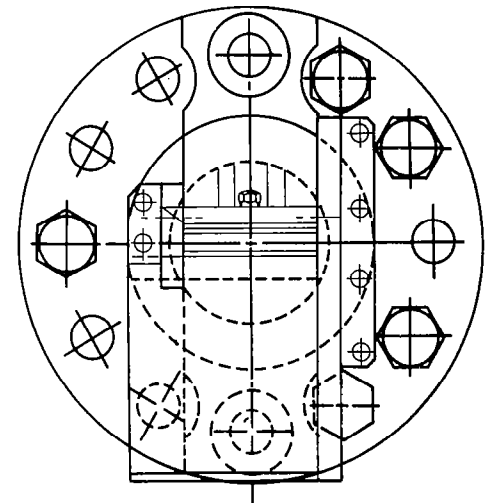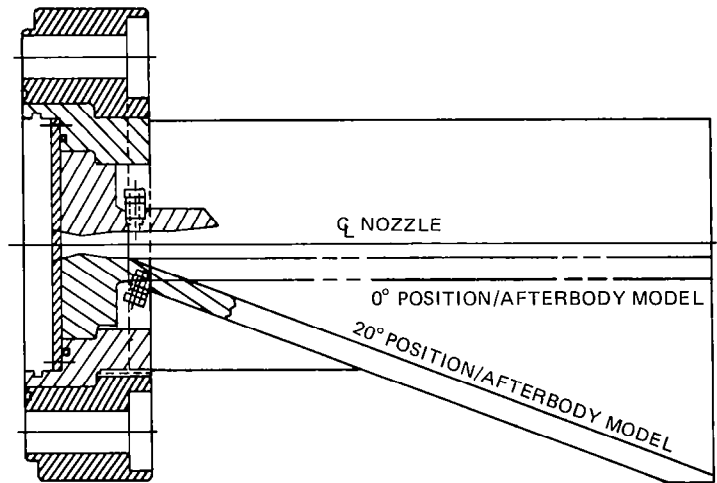
Fig. 4   Drawing of Nozzle and Model Assembly for Simulating $M_\infty = 6$ SCRJ Exhaust Flow
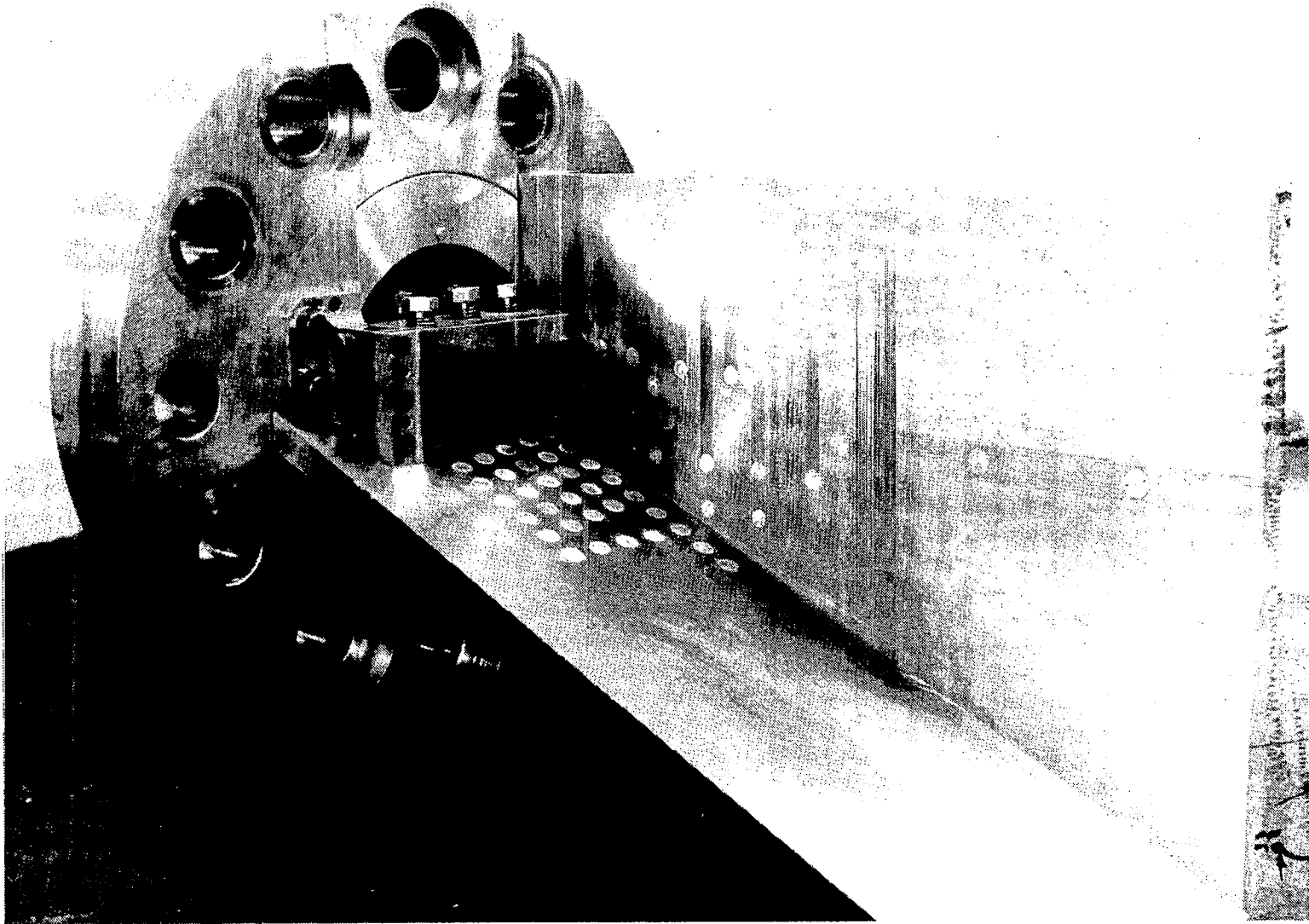
Fig. 5 Photograph of 20° Afterbody Model Assembly
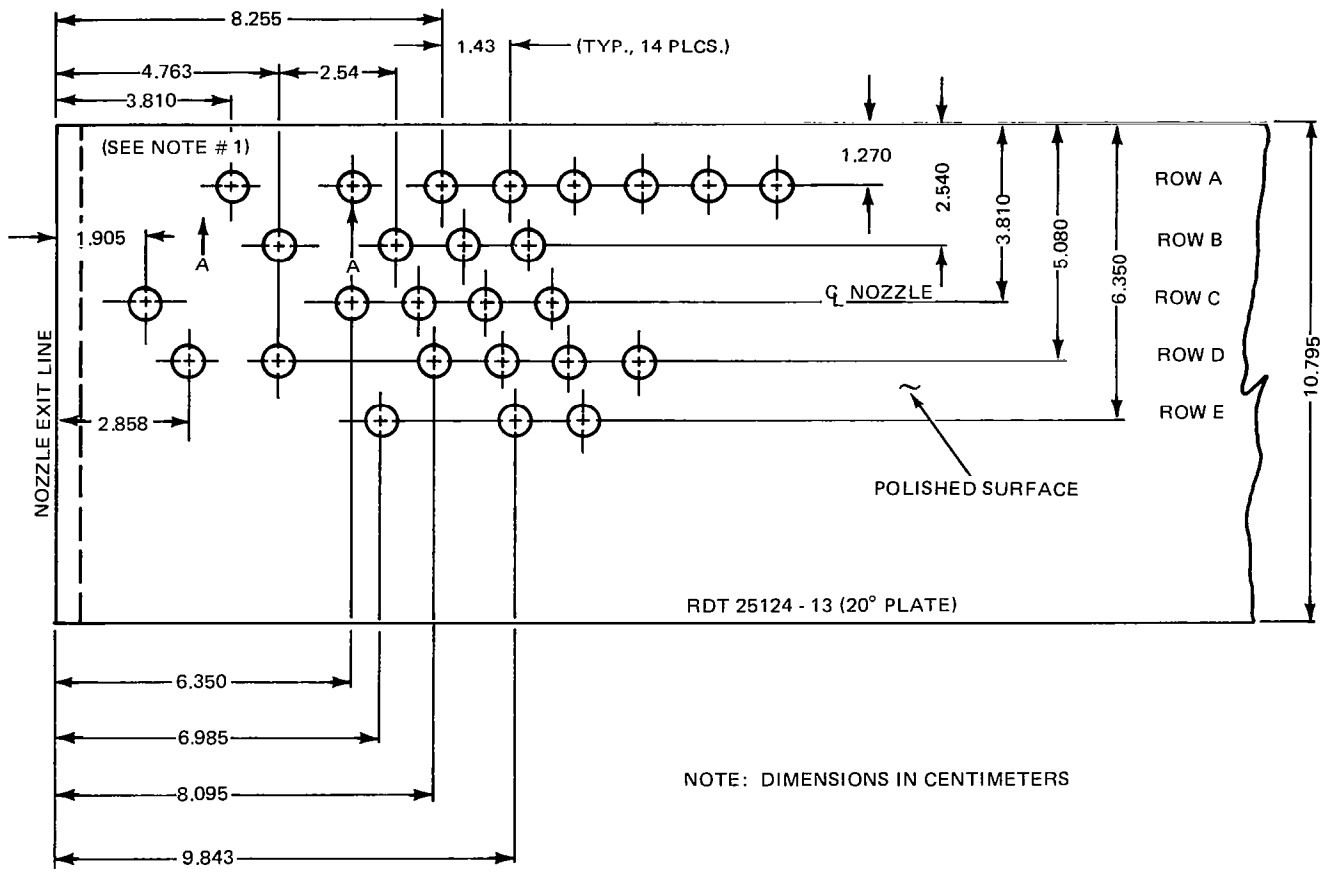
Fig. 6 Drawing of 20° Afterbody Pressure Plate

10
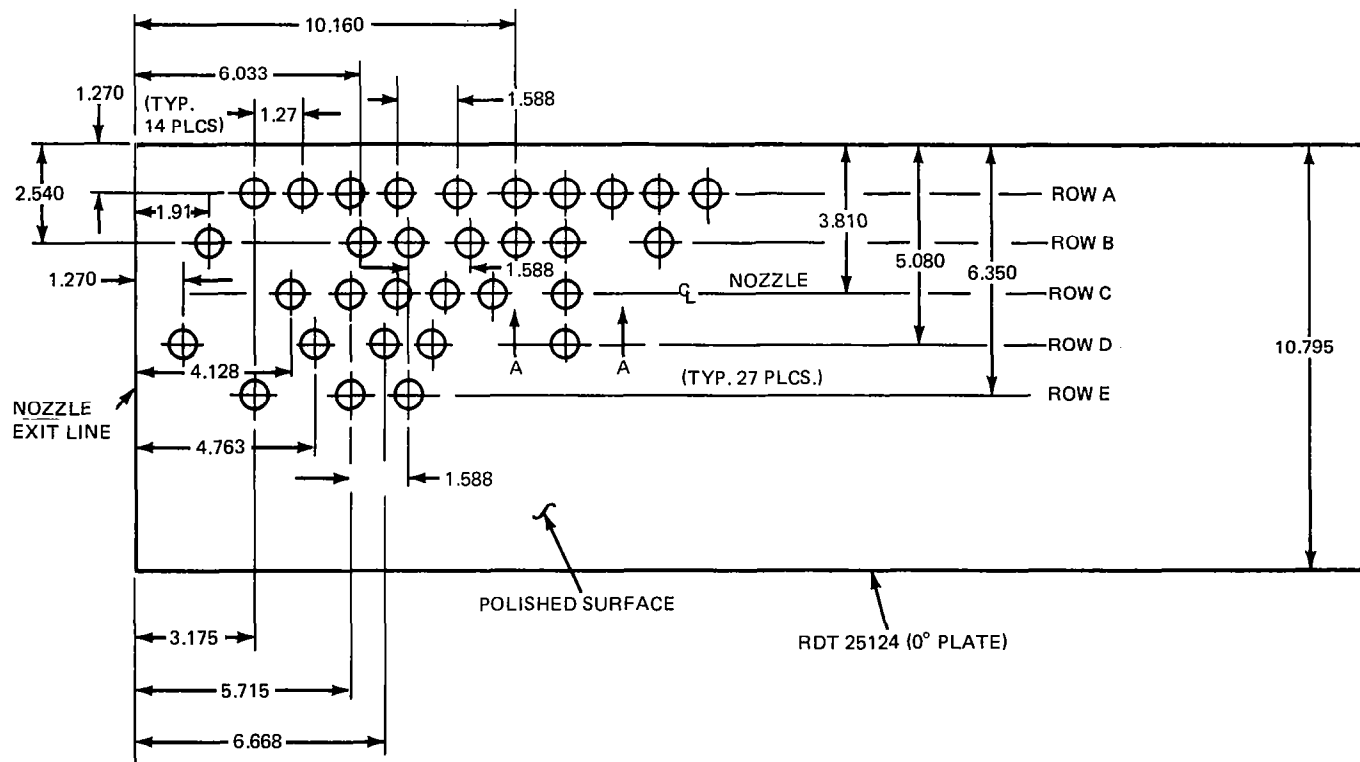
Fig. 7 Drawing of 0° Afterbody Pressure Plate

NOTE: DIMENSIONS IN CENTIMETERS

11

POLISHED SURFACE

NOZZLE

NOZZLE EXIT LINE

RDT 25124-11 (REFLECTION PLATE)
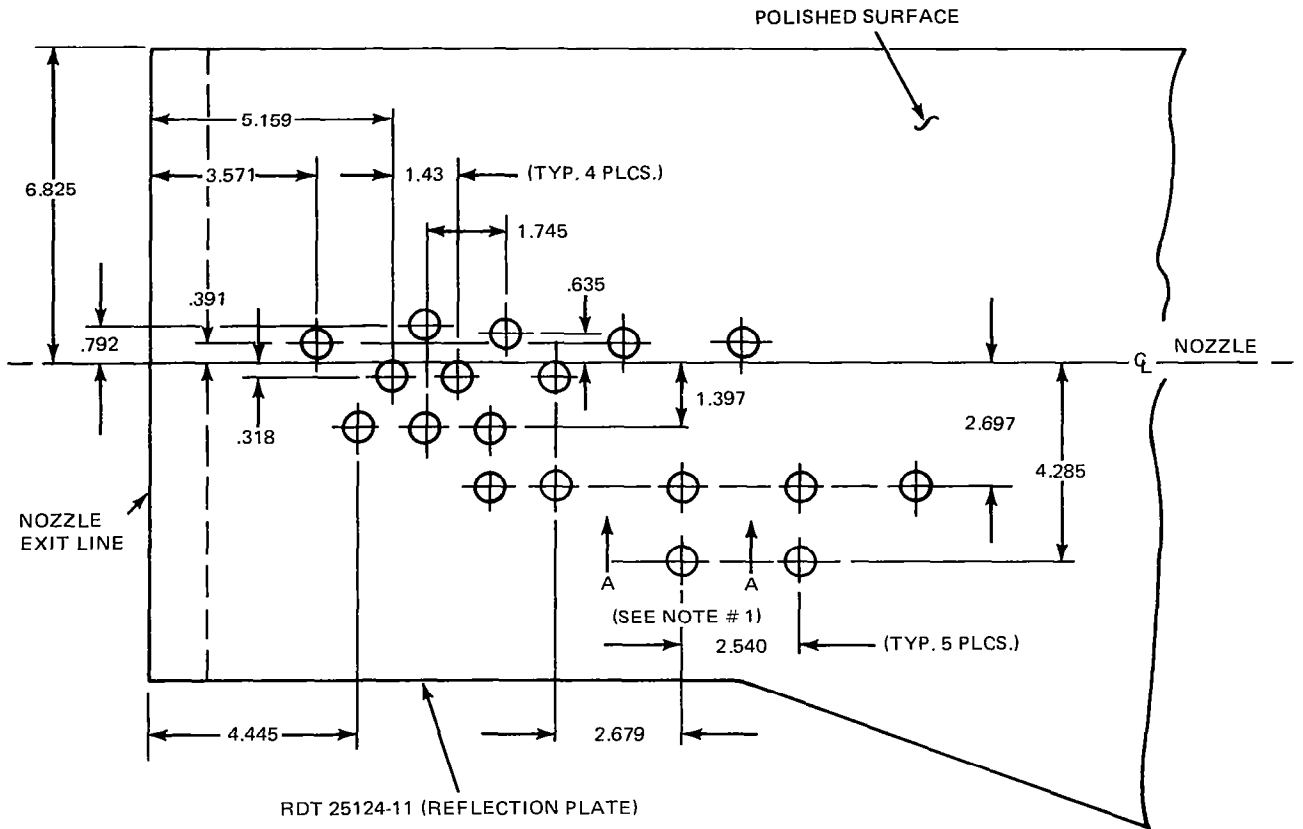
NOTE: DIMENSIONS IN CENTIMETERS

Fig. 8 Drawing of Reflection Plane Pressure Plate

12
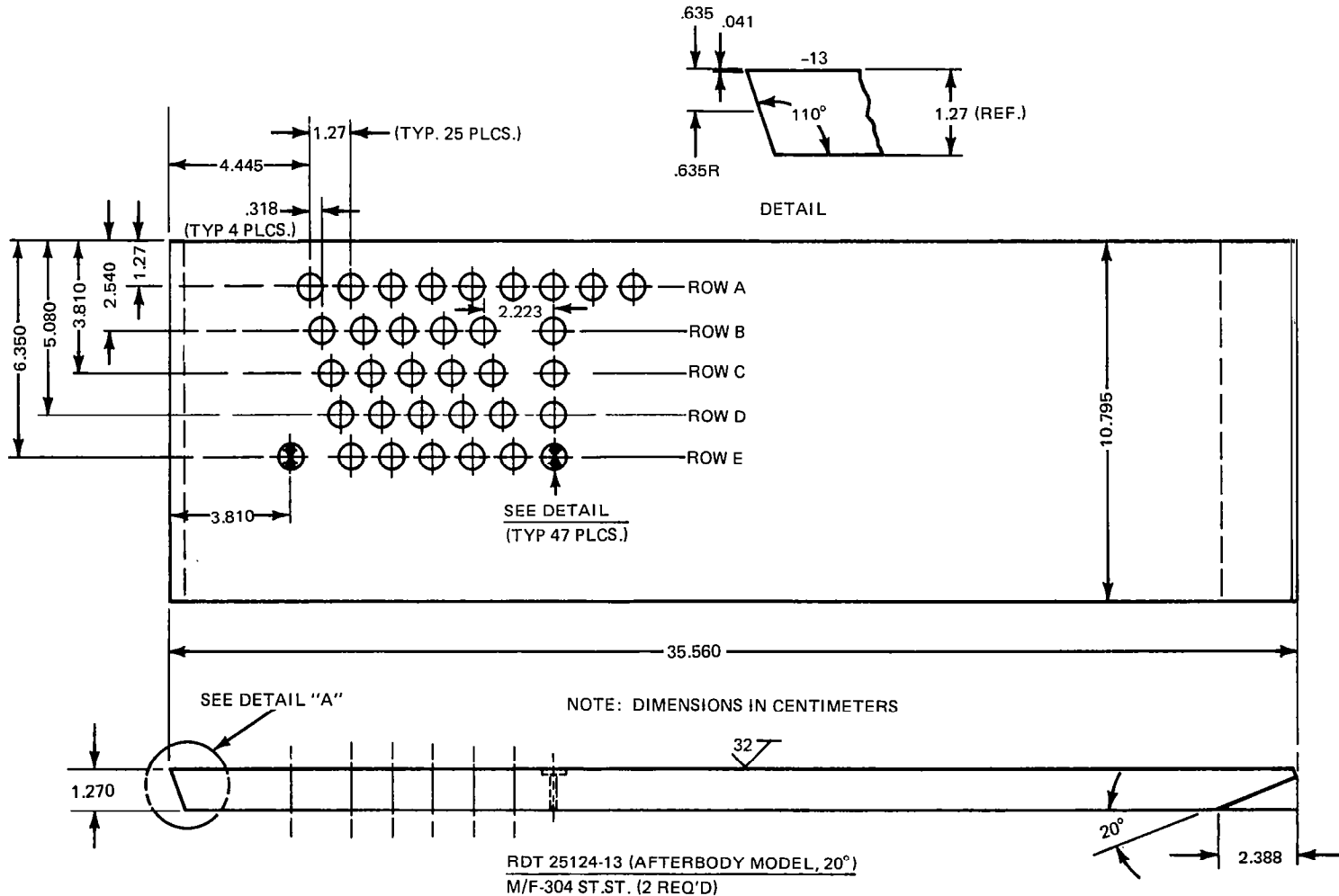
Fig. 9 Drawing of 20° Afterbody Heat Transfer Plate
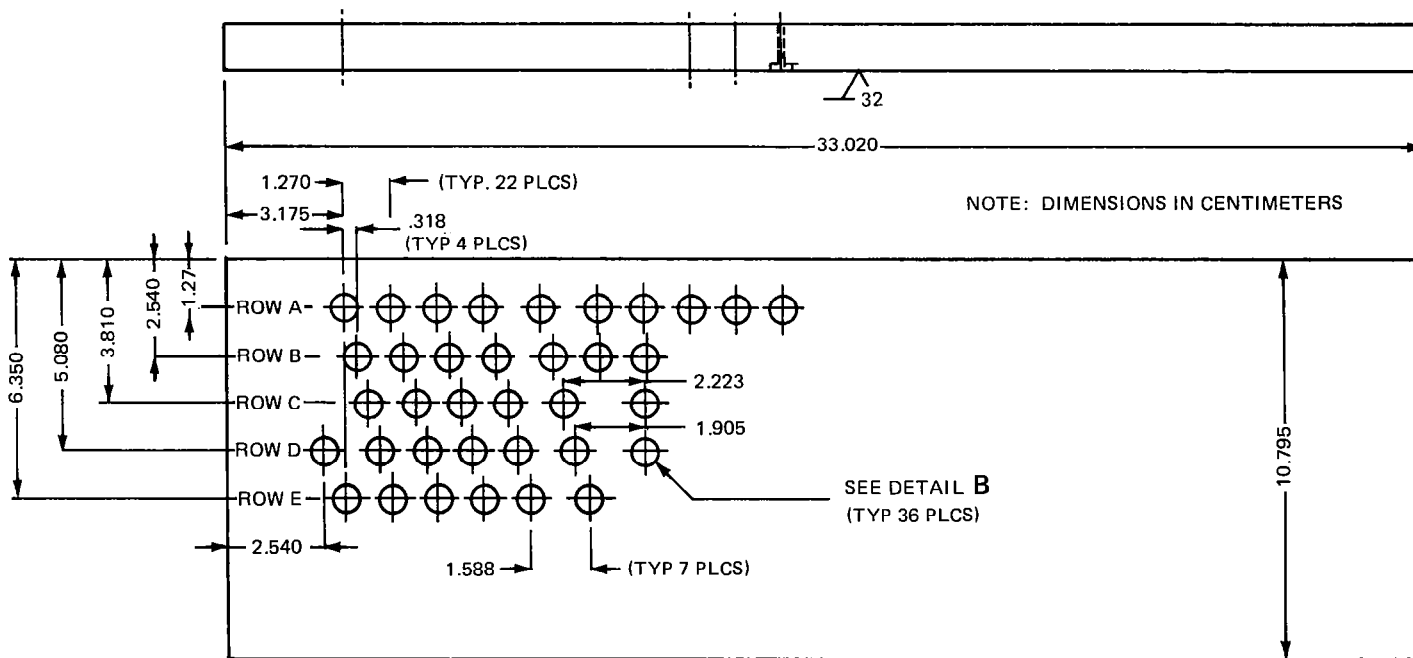
RDT 25124-15 (AFTERBODY MODEL, 0°)

M/F 304 St. ST. (2 REQD)

Fig. 10 Drawing of 0° Afterbody Heat Transfer Plate

14
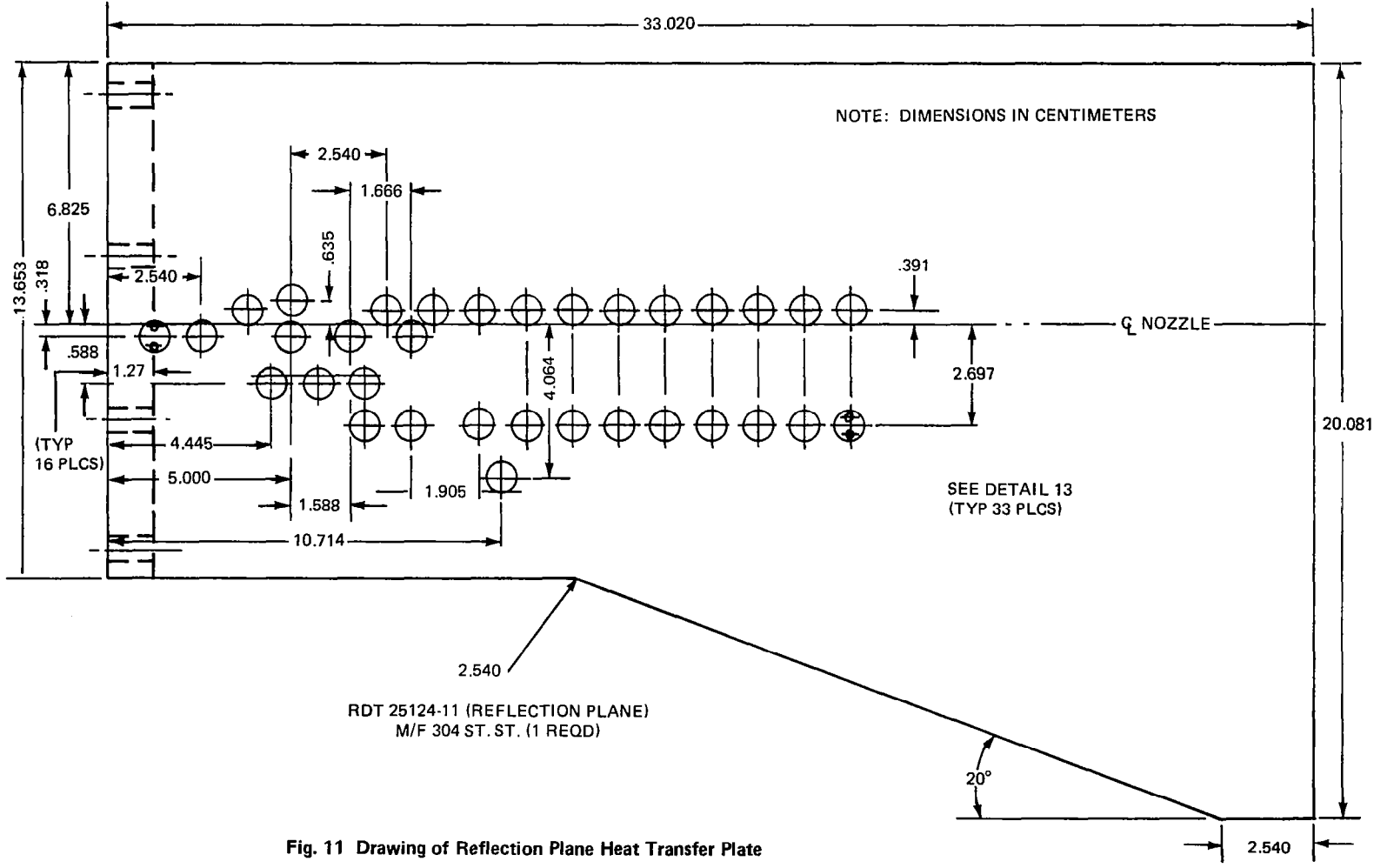
Fig. 11 Drawing of Reflection Plane Heat Transfer Plate

15

COWL AND AFTERBODY MODEL DESIGN

Two afterbody configurations were employed for the present tests: one parallel to the nozzle centerline (called the 0° afterbody) and the other inclined at an angle of 20° to the nozzle centerline. Each configuration consisted of two flat plates: one for mounting pressure transducers and one for heat transfer gauges. One cowl configuration was used with both the afterbody configurations, and was machined as an integral part of the nozzle. Provision was made for mounting shock wave generators on the cowl lip. With the 0° afterbody a shock generator inclined 3° to the nozzle axis was used. With the 20° afterbody the shock generator was inclined 19° to the nozzle axis.

One side of the model assembly consisted of an instrumented reflection plane, extending the entire length of the afterbody from the nozzle exit plane. Instrumentation included both heat transfer and pressure transducers. The other side of the model consisted of a short side plate extending from the nozzle exit plane to the cowl lip. The side plate had provision for shock wave generators to be mounted on its trailing edge. The side shock generator was a 15° wedge for use with the 0° afterbody, and a 20° wedge for use with the 20° afterbody. Figure 4 is a drawing showing the significant dimensions of the nozzle and afterbody model. Figure 5 is a photograph showing the model assembled with the 20° afterbody. Figures 6 through 11 are detailed drawings of the afterbody and reflection plane plates showing all the heat transfer and pressure transducer locations.

For the first part of the contract extension, simulated combustor nozzle separators were installed in our nozzle. They extended from the subsonic portion of the nozzle to the combustor exit plane, and had a zero-camber, transonic airfoil cross-section. They were made in two halves and could be located at any position across the width of the nozzle. The nominal positions were at 1/3 and 2/3 of the nozzle width, thus dividing the 3:1 (width to height) combustor exit plane into three 1:1 segments. Figure 12 is a sketch of these separators and shows their installation in the nozzle. Figure 13 is a photograph of the installation.

To study the near-field effects of the wakes of these separators, additional instrumentation had to be added to the 20° afterbody heat transfer model. The new instrumentation consisted of 13 additional heat transfer gauges and 7 new pressure transducers. Their locations are shown shaded in Fig. 9.
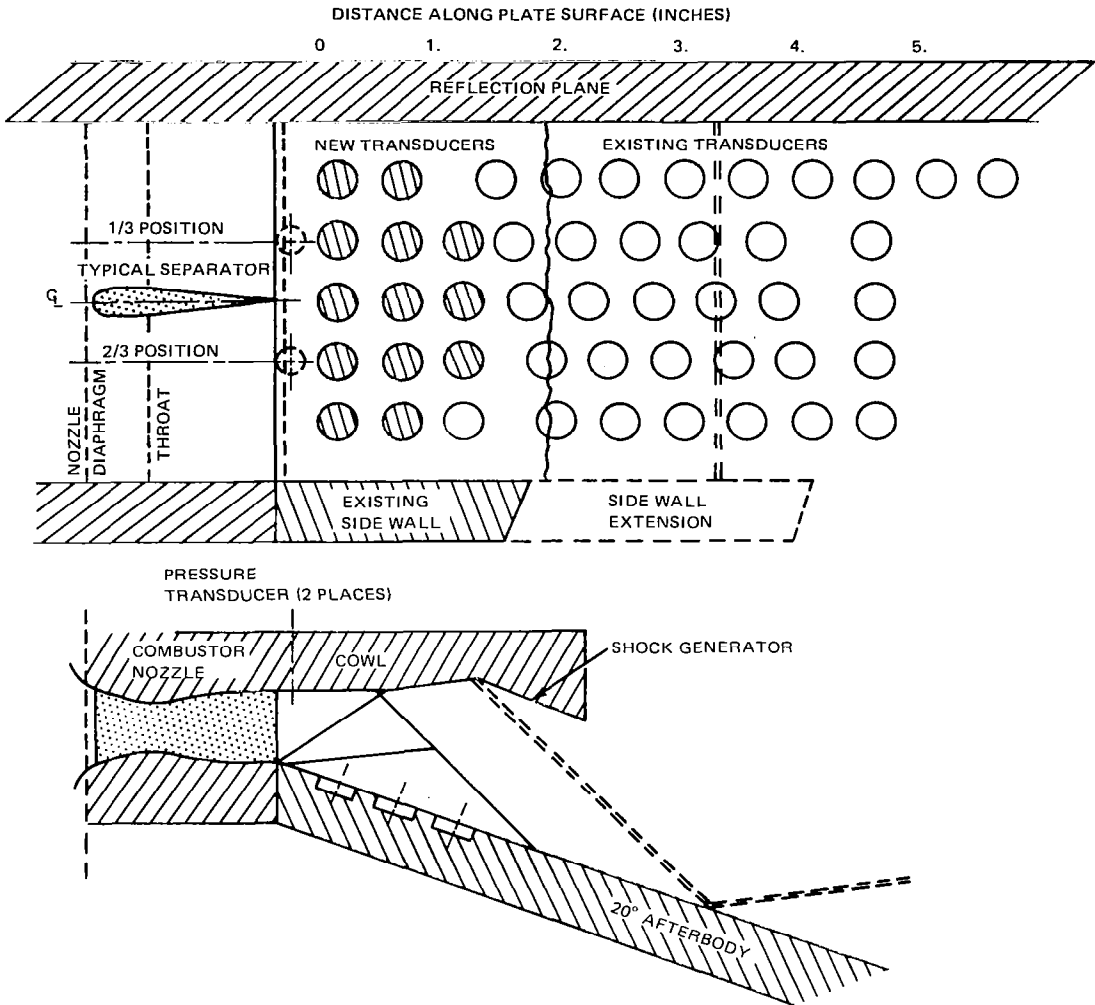
Fig. 12   Sketch Showing Nozzle Separators and Their Installation
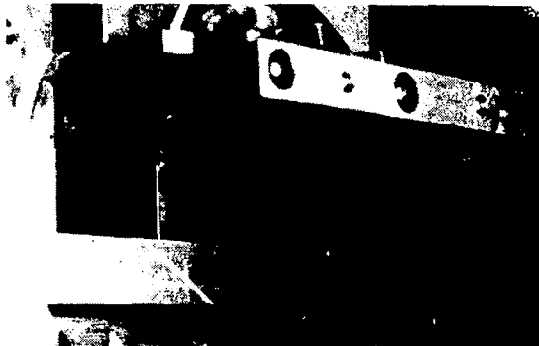
Fig. 13 Photograph of Nozzle Separators Installed in M_∞ = Nozzle (Afterbody Removed).

One side effect of the separators was that their finite thickness (0.533 cm; 0.210 inch) decreased the throat area of our combustor nozzle and consequently increased the nozzle exit Mach number. All heat transfer data taken with sectors in place had to be corrected for these changes in nozzle exit conditions. The correction procedure is described in the Experimental Results Section (5).

The second part of the contract extension consisted of measuring the cowl shock wave impingement location on the 20° afterbody in different substitute gas flows. In order to ensure that the shock wave and its impingement location were completely within a two-dimensional flow region, the nozzle side plate, which originally extended to the cowl lip $(X/Y_3 = 3.12)$, was extended beyond the expected impingement location to $X/Y_3 = 6.62.$

INSTRUMENTATION

Model heating rates were measured with thin film transducers, Ref. (7). These gauges, when used without taking into account changes in substrate properties with temperature, have a range of 0 to 50 cal/cm^2 sec and an accuracy of $\pm7\%$ in this range. When corrections are made for changes in substrate properties (Ref. 8), the useful range is increased to 500 cal/cm^2 sec with an accuracy of $\pm15\%$. For this work all but a few of the combustion heating rates measured on the 20° afterbody and about half of the points on the 0° afterbody were in the 500 cal/cm^2 sec range. Those heating rates above 500 cal/cm^2 sec were corrected by extrapolating the correction curve and are therefore subject to greater error. All data taken using the substitute gas are in the most accurate range. Scatter of the data for the substitute gas runs and most of the combustion runs should be assigned to turbulence and not gauge accuracy.

Model pressures were measured with semiconductor strain gauge pressure transducers while tunnel operating pressures and impact pressure were obtained with piezoelectric pressure transducers. Both gauges are described in Ref. 2 and their performance characteristics are outlined in Table 1. The spatial resolution for detecting shock location is superior for the heat transfer gauge. This advantage plus the lower cost per unit were the reasons for using heat gauges for determining shock locations before committing pressure instrumentation.

TABLE 1 MEASUREMENT ACCURACY

Tunnel Parameter		Accuracy	Range
P_1	Tunnel Driven Initial Pressure	$\pm 689 \ N/m^2$	$0 \rightarrow 6.89 \times 10^5 \ N/m^2$
P_4	Tunnel Driver Initial Pressure	$\pm 1.38 \times 10^5 \ N/m^2$	$0 \rightarrow 1.38 \times 10^7 \ N/m^2$
P_5	Stagnation Pressure	$\pm 3.10 \times 10^5 \ N/m^2$	$0 \rightarrow 1.38 \times 10^7 \ N/m^2$
U_{inc}	Incident Wave Speed	$\pm 30 \ m/sec$	$0 \rightarrow 900 \ m/sec$
P_{T_2}	Impact Pressure	$\pm 6.89 \times 10^4 \ N/m^2$	$0 \rightarrow 6.89 \times 10^6 \ N/m^2$
Q	Heat Transfer Rate	$\pm 7\%$	$0 \rightarrow 50 \ gm \ cal/cm^2 sec$

All model data were recorded on a 35-channel FM multiplex recorder system after suitable signal conditioning. Data were digitized one channel at a time by an A/D converter and a time average of the signal during the tunnel test time was obtained from this digital information. A more detailed description of the data acquisition and reduction system appears in Ref. 2. Major components of the system are outlined in Table 2.

SPATIAL RESOLUTION OF HEAT TRANSFER GAUGE IN THE Z DIRECTION

Our heat transfer gauges have an active area defined by a span of 0.762 cm (perpendicular to the flow) and a chord of 0.159 cm (parallel to the flow). Each measured heating rate was the average over this area. Therefore, strong gradients in the spanwise z direction produce measured heating rates smaller than the peak value. For the experiments performed under the contract extension it was not possible to reorient the instrumentation (rotate the gauges 90°); with the existing gradients in the y direction such reorientation would have been of doubtful value. In order to assess the probable impact of limited gauge resolution, the following discussion may be helpful.

Given a rectangular perturbation in heating rate such as:
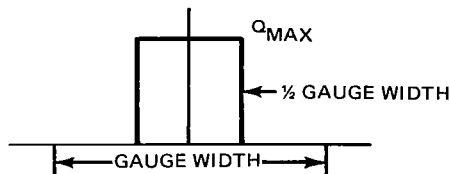
TABLE 2 INSTRUMENTATION AND DATA RECORDING EQUIPMENT

Pressure Transducers		
Manufacturer	Model No.	Max Range
Kuhlite	VQS-250-200	1.38×10^6 N/m^2
Kuhlite	VQL-250-20	1.38×10^5 N/m^2
Kuhlite	VQH-250-5	3.45×10^4 N/m^2
Kistler	603 L	1.03×10^7 N/m^2
Kistler	607	4.13×10^8 N/m^2
Data Recording and Reduction		
Honeywell	7600 tape recorder	1.5 MHz bandwidth
D.C.S.	Gov-3 VCO's	±2v, ±32' kHz
D.C.S.	GMA-5, line drivers	–
D.C.S.	GFD-14, discriminators	±10v, ±16 kHz
Hewlett-Packard	A/D converter	12 bit, 50 μ sec/word
Hewlett-Packard	21 MX computer	–
Texas Instruments	700 ASR terminal and cassette tape drive	

a linear averaging of heating rate over the gauge gives a result 50% lower than the peak. Obviously, this average is in greater error for narrower perturbations. For high heating rates as in the combustion gas case the problem is further complicated by the temperature dependence of the gauge substrate properties, which makes the equations relating the heating rate to time and temperature nonlinear. Averaging of such high rates gives an even lower result for the peak heating rate. However, this additional error is small compared to the error caused by spatial resolution alone.

FLOW VISUALIZATION

Glow photographs, i.e., those taken by the light of the flow, gave low contrast prints (Figs. 14 and 15) when no shock generators were used. When the top shock generator or top and side generators were used a bright region in the position of the shock could be seen (Figs. 16 and 17). These photos, taken with Polaroid PN type 55 film with a 135 mm lens or with a 254 mm lens, show shock locations for the combustion runs, but the contrast is still quite low and the visible plume appears to fill the entire test section. Schlieren photos could not be made in this configuration since the reflection plane is in the schlieren optical path.

3. DETONATION TUBE RUNNING CONDITIONS

SHOCK TUBE MIXTURE DEVELOPMENT

Any one of a number of initial fuel mixtures may be used to achieve a proper simulation of the scramjet exhaust. For each of these mixtures there is an appropriate initial pressure and incident shock speed that will yield the correct pressure, enthalpy, and chemistry in the stagnation region.

Our first attempts used an initial fuel mixture of hydrogen and air. Runs made using this mixture had a large time delay between the arrival of the incident shock at the end wall and the formation of a detonation wave. There was burning of the mixture at shock arrival, seen by the large increase in pressure and noise, but that the detonation wave was not established until much later (see Fig. 25). Efforts to shorten this delay by increasing incident shock velocity had no consistent effect until the incident
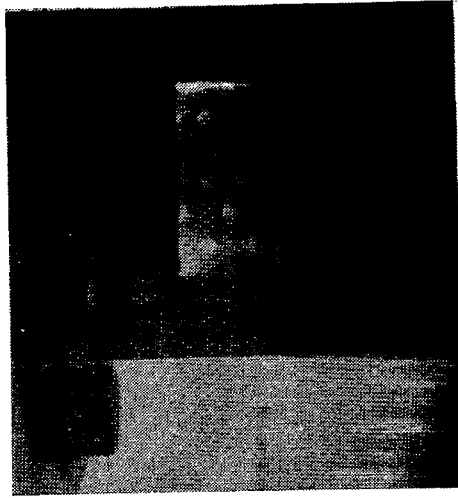
Fig. 14 Glow Photograph, Top View, 0° Afterbody Model with No Shock Generators
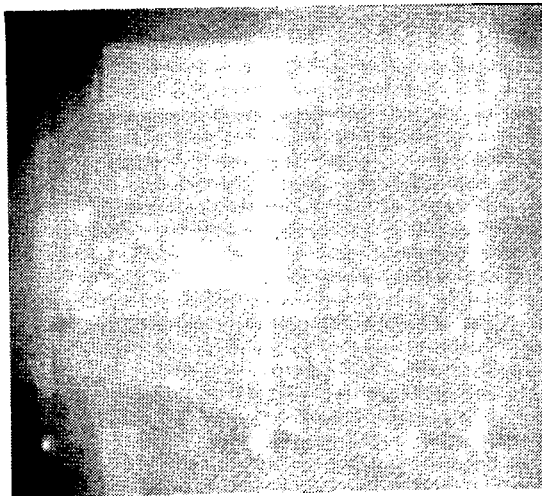
Fig. 15 Glow Photograph, Side View, 0° Afterbody Model with No Shock Generators
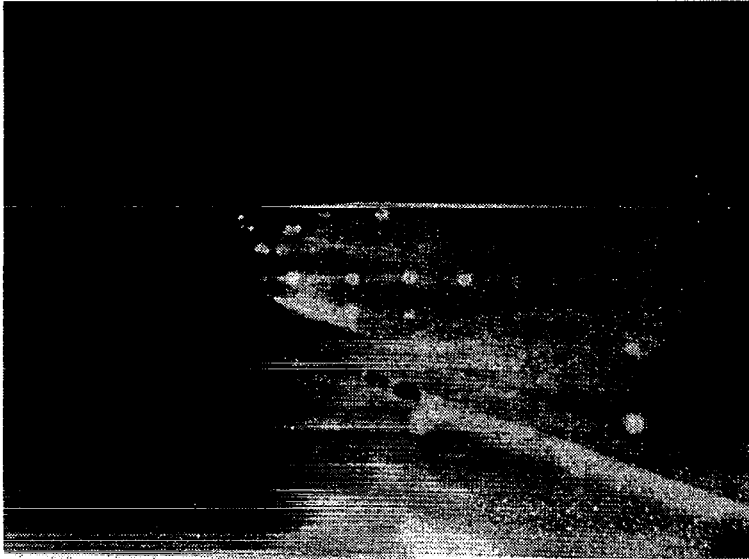
Fig. 16   Glow Photograph, Side View, 20° Afterbody Model with Top (Cowl) Shock Wave Generator
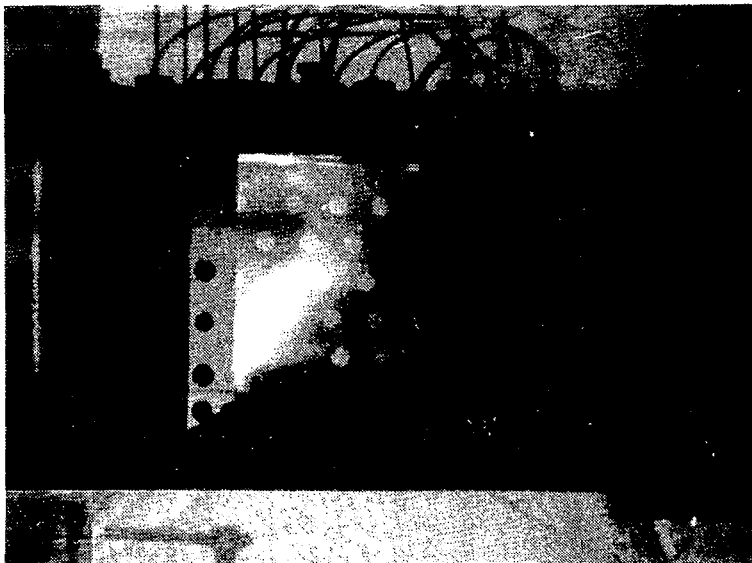
Fig. 17   Glow Photograph, Top View, 20° Afterbody Model with
Top and Side Shock Wave Generators

23

wave became strong enough to cause ignition of the incident shock, what we call a front-running detonation. We also tried starting the detonation with two spark plugs rather than one, with the hope that a more uniform ignition source would shorten the delay time. This also had no consistent effect. At this point we decided to investigate other mixtures.

In previous scramjet simulation of the $M_\infty = 8$ condition (Ref. 2), we used a fuel which had all of the oxidizer in the form of nitrous oxide. For the $M_\infty = 6$ condition this fuel required high initial pressures and low incident shock velocities which make shock tube operation difficult. Nevertheless, a series of runs was made with nitrous oxide substituted for various amounts of oxygen in the fuel. None of these runs produced less delay time than hydrogen and air. Since having the oxidizer in a different form failed, we tried supplying some of the required hydrogen contained in ammonia.

We started with a mixture that had all of the hydrogen in the form of ammonia and found it produced a front-running detonation when subjected to a shock of the proper velocity for correct simulation. Since the ammonia sensitized the reaction, a series of tests were made to determine what proportion of ammonia and hydrogen was needed to reduce the ignition delay without igniting the incident wave. This line of testing established the fuel mixtures described previously and was used for all runs to obtain data for the combustion case.

COMBUSTION GAS ($\phi = 1.0$)

A complete description of the operation, performance, and computational procedures involved in determining the detonation tube simulator running conditions is given in Ref. 1. All the combustion gas data presented herein were obtained using the backward-running detonation technique.

As shown in Fig. 7 of Ref. 1 there are any number of gas mixtures that are apparently eligible to be used for simulation. However, we encountered considerable difficulty in getting many of these mixtures to ignite properly. Some would ignite very early, during the passage of the incident wave, and others would ignite very late, after the passage of the reflected wave. Repeatability was also a problem, with things like

the condition of the shock tube wall appearing to be a factor affecting the rate of ignition (e.g. Ref. 9). Section 5 of this report gives the details of these experimental ignition problems.

We eventually found one mixture which behaved repeatably and for which ignition delay was tolerable ($\angle 1.0$ msec.). This mixture was composed of

$$0.220 \text{ H}_2 + 0.157 \text{ O}_2 + 0.533 \text{ N}_2 + 0.063 \text{ NH}_3 + 0.007 \text{ Ar}$$
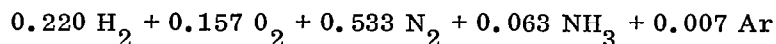
To determine the state of the test gas after the delayed ignition we carefully measured the incident and reflected shock wave speeds and formulated a one-dimensional wave diagram consistent with the wave speed measurements, the pressure time-history measurements, and previous models of delayed reflected ignitions (e.g. Ref. 10). Figure 18 shows this wave diagram.

Figure 19 is an oscilloscope picture showing the detonation tube stagnation pressure time history for this running condition. (Note the difference in the pressure time-history between this running condition with a short ignition delay and that with zero delay as shown in Fig. 13a of Ref. 2.) We were then able to calculate the state of the gas in regions 6 and 7 using the computer program of Ref. 6, by assuming that a Chapman-Jouget detonation started in region 5 and then propagated into region 2. Table 3 summarizes the results of these calculations and gives the state of the gas in the various regions involved. Note that the region 6 gas is about 60 K cooler than ideal, while the region 7 gas is about 160 K hotter than ideal. This is illustrated in the Mollier diagram sketch shown in Fig. 20. In practice these two regions would tend to mix, due to diffusion, turbulence, etc., rather than remain as two discrete regions, and the resulting flow out of the nozzle should be extremely close to the desired, ideal testing condition.

The measured static pressure at the exit of the nozzle, P_3, and on the flat portion of the cowl (before the 6 degree bend) was $1.730 \times 10^6 \text{ N/m}^2$ (251. psia). An oscilloscope picture showing this measurement is presented in Fig. 21. Based on the measured P_5/P_3 ratio, the ideal total enthalpy, and assuming an isentropic, equilibrium expansion, we computed (Ref. 6) the exit plane Mach number to be 1.706. Table 4 presents the significant running conditions obtained by the procedure outlined above.
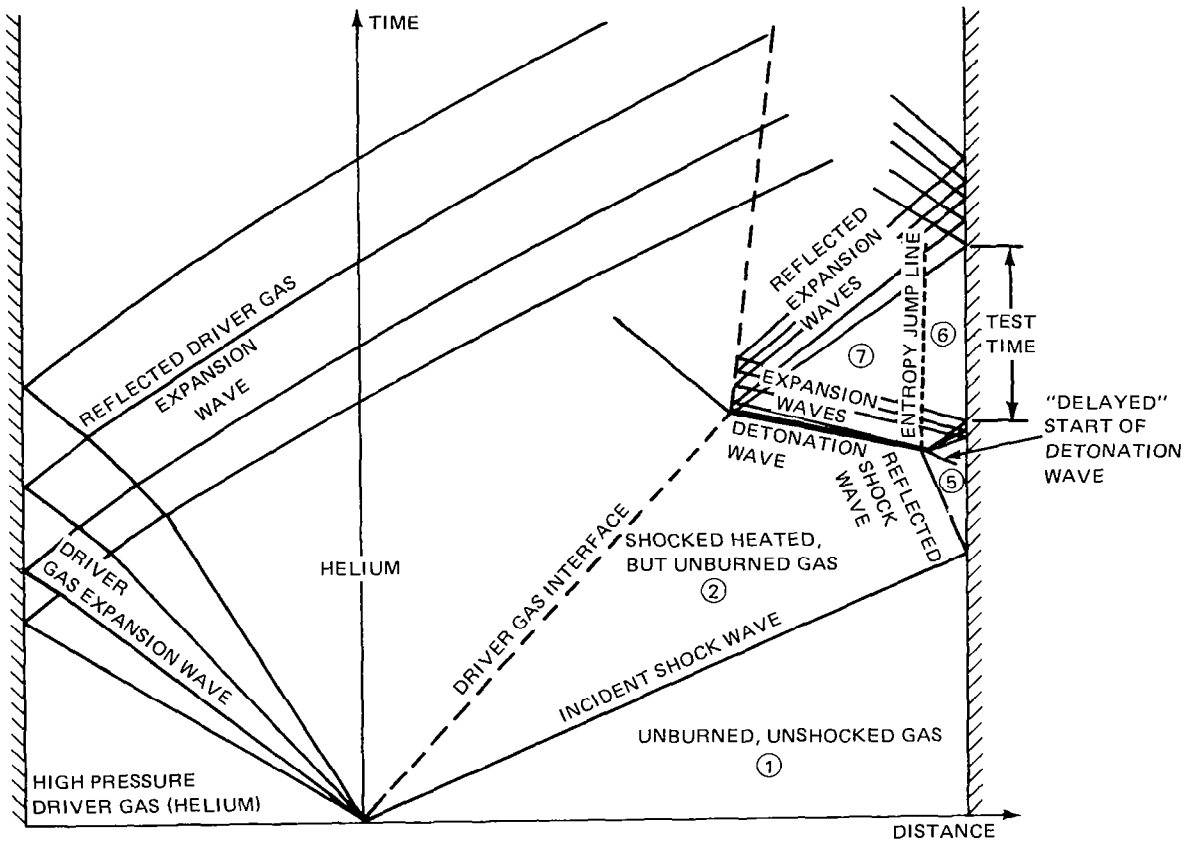
Fig. 18 Distance-Time Wave Diagram Illustrating Delayed Start of Reflected Detonation Wave
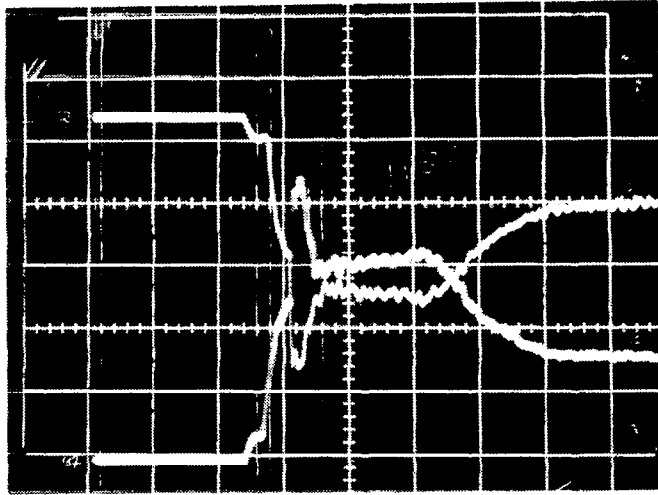
Fig. 19   Oscilloscope Record of Detonation Tube Stagnation Pressure with Delayed Reflected Ignition
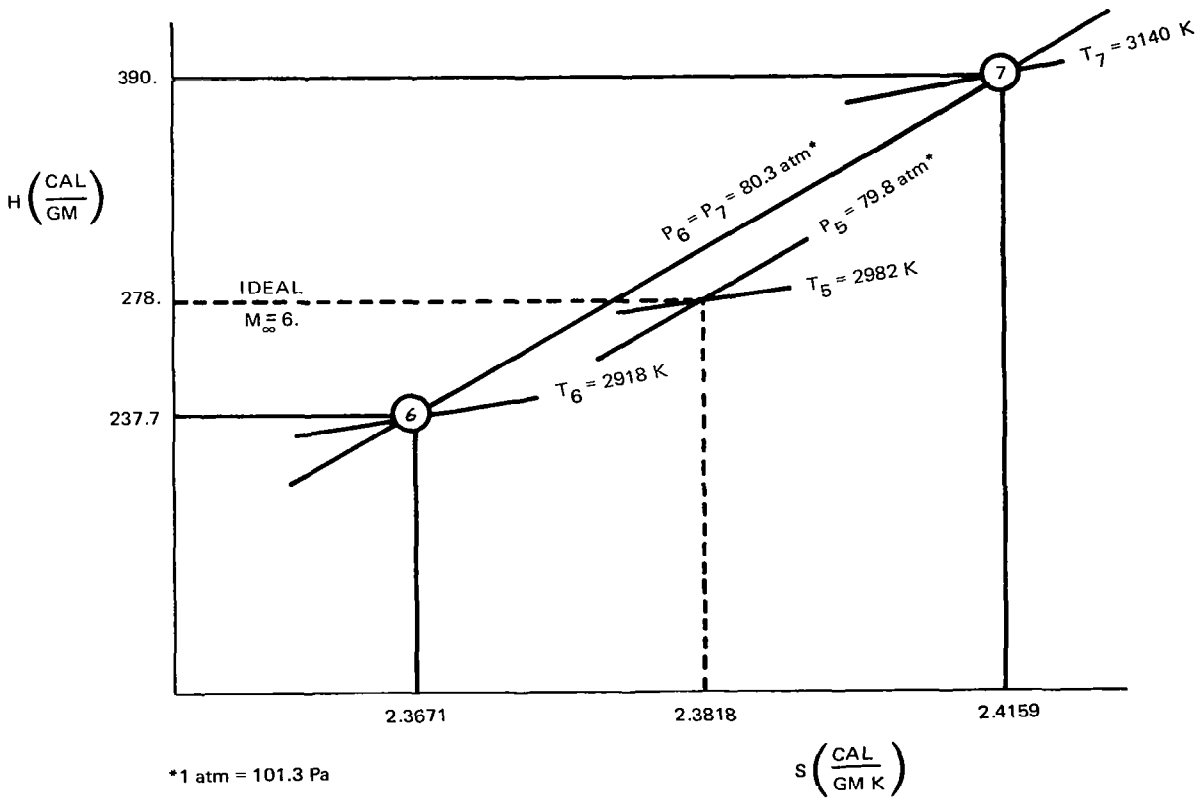
*1 atm = 101.3 Pa

Fig. 20   Mollier Diagram Sketch of Detonation Tube Stagnation Conditions
1 atm = 101.3 kPa

27
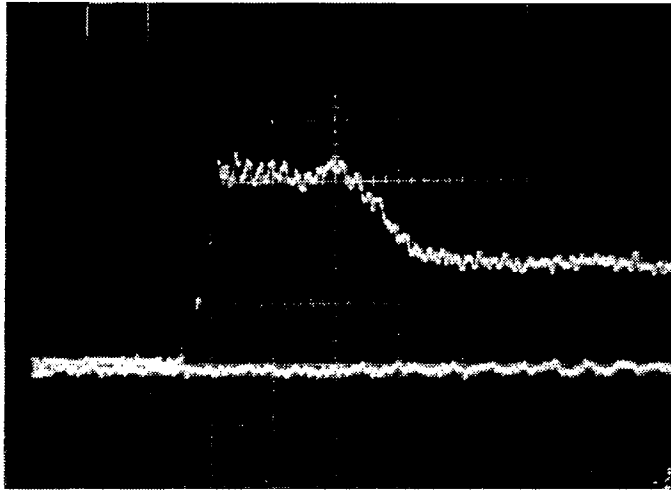
Fig. 21   Oscilloscope Record of Combustor Nozzle Exit Plane Static Pressure
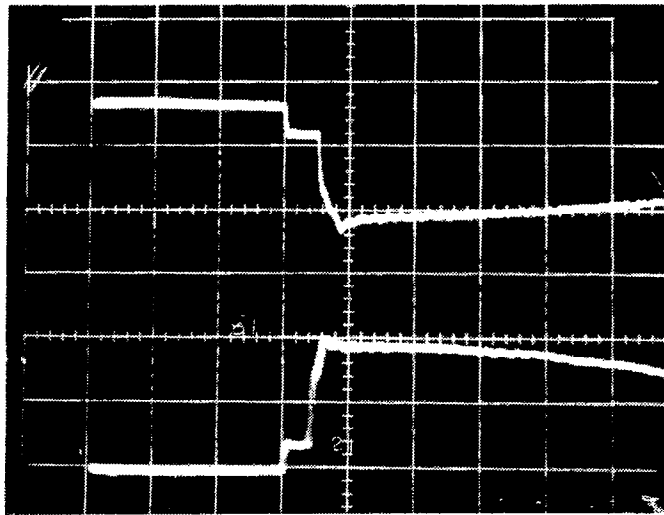
Fig. 22   Oscilloscope Record of Substitute Gas Reflected Shock Stagnation Pressure, P_5

TABLE 3 EQUILIBRIUM THERMODYNAMIC STATE PROPERTIES IN BACKWARD-RUNNING DETONATION TUBE FOR SIMULATING 1/20 SCALE SCRJ EXHAUST AT M∞ = 6 ($\phi = 1.0$)

Region 1	$0.21967\ H_2 + 0.15691\ O_2 + 0.55348\ N_2 + 0.06276\ NH_3 + 0.00719\ AR$ $P_1 = 1.364$ atm, $T_1 = 298.$ K, $U_s = 996.34$ m/sec
Region 2	same gas $P_2 = 10.043$ atm, $T_2 = 633.$ K, $U_2 = 708.84$ m/sec
Region 5	same gas $P_5 = 43.657$ atm, $T_5 = 1001.$ K, $U_R = 404.88$ m/sec
Region 6	stagnant, reacted test gas $0.63410\ N_2 + 0.31727\ H_2O + 0.01867\ H_2 + 0.00978\ OH + 0.00783\ Ar +$ $0.00568\ NO + 0.00420\ O_2 + \ldots.$ $P_6 = 80.3$ atm, $T_6 = 2918.$ K, $H_6 = 237.7$ cal/gm, $S_6 = 2.3671$ cal/gm K
Region 7	stagnant, reacted test gas $0.62586\ N_2 + 0.29744\ H_2O + 0.02995\ H_2 + 0.01709\ OH + 0.00775\ Ar +$ $0.00916\ NO + 0.00646\ O_2 + \ldots.$ $P_7 = 80.3$ atm, $T_7 = 3140.$ K, $H_7 = 390.$ cal/gm, $S_7 = 2.4169$ cal/gm K

TABLE 4 COMBUSTION GAS RUNNING CONDITIONS

$\phi = 1.0$, $\alpha + \beta = 4^o$, 1/20 Scale

	Ideal (Ref. 1)	Based on Measured P_5/P_3
P_5 (N/m^2)	8.086×10^6	8.136×10^6
H_5 (cal/gm)	278.0	278.0
T_5 (K)	2982.0	2982.0
P_3 (N/m^2)	1.861×10^6	1.730×10^6
T_3 (K)	2375.0	2343.0
M_3	1.657	1.706
γ_3	1.2122	1.2144
Rey. No. $_3$ (m^{-1})	5.02×10^7	4.895×10^7

SUBSTITUTE GAS

Thermodynamic properties of the substitute gas mixture used in the present tests were computed by the method detailed in Appendix A of Ref. 2 and are listed in Table 5. The particular mixture chosen for these tests was 50% Argon and 50% Freon 13B1 with a stagnation temperature of 533.3 K. This mixture was the gas planned to be used in the concurrent Langley Test Program (see page 4) and for which the two-dimensional contoured nozzle was designed. To achieve full scale Reynolds number at the combustor exit plane a stagnation pressure of 5.516×10^5 N/m^2 (80. psia) was required.

The detonation tube facility was operated in the reflected shock tube or shock tunnel mode (Ref. 1) in order to generate the required stagnation conditions for the substitute gas runs.

The incident shock wave strength required to produce the stagnation temperature was computed from ideal gas shock equations using an average value of γ across the incident and reflected shock waves. Figure 22 is an oscilloscope picture showing the reflected shock stagnation pressure in the shock tube. Note that as reported in our previous work at the $M \infty = 8$ flight condition (Ref. 2), the same reflected shock bifurcation phenomena occurs; this results in a somewhat gradual rise to the final stagnation pressure level. A detailed explanation of this phenomena is given in Ref. 2.

For these substitute gas runs the static pressure at the exit of the nozzle and on the flat portion of the cowl, P_3, measured 1.434×10^5 N/m^2 (20.8 psia). From the measured P_5/P_3 ratio and the calculation procedure described earlier, we determined the Mach number at the exit plane of the nozzle to be 1.63. This agrees very closely with the value calculated for our nozzle using the two-dimensional method-of-characteristics program (Ref. 5).

One of the objectives of the contract extension was to study the sensitivity of the cowl shock wave impingement location with variations in substitute gas properties. To do this we selected five additional substitute gas mixtures and/or stagnation temperatures and calculated the nozzle and afterbody flow fields with each of these gasses. The additional gas mixture/temperature combinations selected were

50% Argon + 50% Freon 13B1 @ T5 = 477.8 K

60% Argon + 40% Freon 13B1 @ T5 = 533.3 K

60% Argon + 40% Freon 13B1@ T5 = 477.8 K

60% Argon + 40% Freon 12 @ T5 = 533.3 K

60% Argon + 40% Freon 12 @ T5 = 477.8 K

The results of these calculations are discussed in the next section. Tables 6 through 10 give the thermodynamic properties of these mixtures, determined by the procedure detailed in Appendix A of Ref 2.

TABLE 5   THERMODYNAMIC PROPERTIES OF 50% ARGON –
50% FREON 13B1 SUBSTITUTE GAS MIXTURE AT T_o = 533.3°K

Mach Number	γ	T(K)	$Cp(\frac{cal}{gm\ K})$	P/Po
5.4882	1.3695	111.1	0.07799	3.6027E-04
5.0921	1.3451	127.8	0.08022	6.1281E-04
4.5523	1.3127	155.6	0.08834	1.3580E-03
4.1114	1.2877	183.3	0.09419	2.7686E-03
3.8795	1.2753	200.0	0.09749	4.1148E-03
3.4039	1.2519	238.9	0.10459	9.6545E-03
3.0470	1.2364	272.2	0.11006	1.8794E-02
2.8268	1.2278	294.4	0.11342	2.8510E-02
2.6166	1.2203	316.7	0.11656	4.2430E-02
2.4138	1.2137	338.9	0.11949	6.2070E-02
2.2155	1.2080	361.1	0.12223	8.9396E-02
2.0194	1.2028	383.3	0.12478	0.12693
1.8720	1.1994	400.0	0.12658	0.16366
1.6724	1.1952	422.2	0.12883	0.22723
1.4117	1.1906	450.0	0.13143	0.33697
1.2443	1.1882	466.7	0.13287	0.42343
1.0623	1.1859	483.3	0.13424	0.52907
0.9969	1.1852	488.9	0.13468	0.56915
0.8555	1.1838	500.0	0.13553	0.65749
0.4852	1.1813	522.2	0.13713	0.87146
0.0000	1.1801	533.3	0.13789	1.0000

TABLE 6   THERMODYNAMIC PROPERTIES OF 50% ARGON - 50% FREON 13B1 SUBSTITUTE GAS MIXTURE AT T_o = 477.8 K

Mach Number	γ	T(K)	Cp($\frac{cal}{gm\ K}$)	P/Po
5.0403	1.3695	111.1	0.07799	7.3299E-04
4.5515	1.3378	133.3	0.08333	1.4737E-03
4.0574	1.3072	161.1	0.08955	3.2047E-03
3.6462	1.2833	188.9	0.09531	6.4432E-03
3.2893	1.2644	216.7	0.1006	1.2202E-02
2.9692	1.2490	244.4	0.1055	2.2032E-02
2.6743	1.2364	272.2	0.1101	3.8238E-02
2.3959	1.2258	300.0	0.1142	6.4176E-02
2.1802	1.2186	322.2	0.1173	9.5084E-02
2.0203	1.2137	338.9	0.1195	0.12628
1.8602	1.2093	355.6	0.1216	0.16626
1.7525	1.2066	366.7	0.1229	0.19879
1.6981	1.2053	372.2	0.1235	0.21709
1.6433	1.2041	377.8	0.1242	0.23687
1.5319	1.2017	388.9	0.1254	0.28129
1.4172	1.1994	400.0	0.1268	0.33298
1.2980	1.1972	411.1	0.1277	0.39293
1.1066	1.1942	427.8	0.1294	0.50090
0.9661	1.1924	438.9	0.1304	0.58681
0.8084	1.1906	450.0	0.1314	0.68558
0.6201	1.1890	461.1	0.1324	0.79885
0.3547	1.1874	472.2	0.1333	0.92845
0.0000	1.1866	477.8	0.1338	1.00000

TABLE 7 THERMODYNAMIC PROPERTIES OF 60% ARGON-40% FREON 13B1 SUBSTITUTE GAS MIXTURE AT T_o = 533.3 K

Mach Number	γ	T(K)	$Cp(\frac{cal}{gm\ K})$	P/Po
5.1299	1.4003	111.1	0.083216	7.9151E-04
4.6384	1.3716	133.3	0.087802	1.5238E-03
4.3317	1.3534	150.0	0.091092	2.3726E-03
4.0626	1.3376	167.7	0.094257	3.5765E-03
3.7473	1.3193	188.9	0.098282	5.9346E-03
3.5357	1.3074	205.6	0.10116	8.4590E-03
3.2786	1.2936	227.8	0.10481	1.3192E-02
3.0436	1.2816	250.0	0.10825	2.0014E-02
2.7732	1.2689	277.8	0.11226	3.2614E-02
2.5215	1.2581	305.6	0.11596	5.1520E-02
2.2361	1.2472	338.9	0.12003	8.6106E-02
2.0062	1.2395	366.7	0.12311	0.12879
1.9152	1.2367	377.8	0.12427	0.15042
1.8242	1.2341	388.9	0.12538	0.17513
1.7329	1.2317	400.0	0.12646	0.20330
1.6870	1.2305	405.6	0.12698	0.21880
1.5945	1.2282	416.7	0.12800	0.25291
1.5006	1.2261	427.8	0.12899	0.29154
1.4048	1.2241	438.9	0.12994	0.33521
1.3062	1.2222	450.0	0.13085	0.38444
1.1511	1.2195	466.7	0.13216	0.47005
1.0407	1.2178	477.8	0.13299	0.53592
0.9827	1.2170	483.3	0.13340	0.57176
0.7190	1.2140	505.6	0.13495	0.73677
0.4487	1.2119	522.2	0.13604	0.88628
0.0000	1.2106	533.3	0.13674	1.00000

TABLE 8 THERMODYNAMIC PROPERTIES OF 60% ARGON – 40% FREON 13B1 SUBSTITUTE GAS MIXTURE AT T_o = 477.8 K

Mach Number	γ	T(K)	Cp($\frac{cal}{gm\ K}$)	P/Po
4.6249	1.4389	111.1	0.07799	1.6860E-03
4.0885	1.3911	138.9	0.08461	3.6120E-03
3.5824	1.3492	172.2	0.09191	8.0182E-03
3.1020	1.3138	211.1	0.09960	1.8188E-02
2.8035	1.2944	238.9	0.10459	3.0914E-02
2.5290	1.2785	266.7	0.10919	5.0676E-02
2.3212	1.2678	288.9	0.11260	7.3595E-02
2.1201	1.2585	311.1	0.11580	0.10504
1.9227	1.2504	333.3	0.11878	0.14760
1.7750	1.2450	350.0	0.12089	0.18873
1.7255	1.2433	355.6	0.12156	0.20450
1.6759	1.2416	361.1	0.12223	0.22141
1.5756	1.2385	372.2	0.12353	0.25894
1.4217	1.2341	388.9	0.12539	0.32563
1.2050	1.2289	411.1	0.12773	0.43766
1.0886	1.2264	422.2	0.12883	0.50535
1.0275	1.2253	427.8	0.12937	0.54250
0.9639	1.2242	433.3	0.12990	0.58203
0.7508	1.2210	450.0	0.13143	0.71610
0.5760	1.2190	461.1	0.13240	0.81982
0.3295	1.2171	472.2	0.13336	0.93644
0.0000	1.2162	477.7	0.13379	1.00000

TABLE 9 THERMODYNAMIC PROPERTIES OF 60% ARGON – 40% FREON 12 SUBSTITUTE GAS MIXTURE AT $\bar{T}_o = 533.3$ K

Mach Number	γ	T(K)	$Cp(\frac{cal}{gm\ K})$	P/P_o
5.2088	1.3973	111.1	0.09661	6.5371E-04
4.6104	1.3581	138.9	0.10419	1.4765E-03
4.1386	1.3281	166.7	0.11119	3.0162E-03
3.6745	1.3006	200.0	0.11886	6.4694E-03
3.1040	1.2707	250.0	0.12897	1.7694E-02
2.7751	1.2558	283.3	0.13484	3.2271E-02
2.5210	1.2458	311.1	0.13925	5.1458E-02
2.2788	1.2373	338.9	0.14325	7.9879E-02
2.0438	1.2301	366.7	0.14685	0.12109
1.8577	1.2251	388.9	0.14948	0.16632
1.7644	1.2229	400.0	0.15072	0.19399
1.7175	1.2218	405.6	0.15131	0.20927
1.6704	1.2208	411.1	0.15190	0.22559
1.5753	1.2188	422.2	0.15303	0.26158
1.4786	1.2169	433.3	0.15412	0.30246
1.3795	1.2151	444.4	0.15516	0.3488
1.1707	1.2119	466.7	0.15711	0.46026
1.0582	1.2104	477.8	0.15802	0.52677
0.9991	1.2097	483.3	0.15847	0.56305
0.8042	1.2077	500.0	0.15974	0.68520
0.5609	1.2058	516.7	0.16094	0.82973
0.3209	1.2047	527.8	0.16170	0.94016
0.0000	1.2041	533.3	0.16207	1.00000

TABLE 10 THERMODYNAMIC PROPERTIES OF 60% ARGON – 40% FREON 12 SUBSTITUTE GAS MIXTURE AT T_o = 477.8 K

Mach Number	γ	T(K)	$Cp(\frac{cal}{gm\ K})$	P/Po
4.7917	1.3973	111.1	0.09661	1.2410E-03
4.2217	1.3581	138.9	0.10419	2.8030E-03
3.6877	1.3230	172.2	0.11252	6.5438E-03
3.2505	1.2967	205.6	0.12006	1.3835E-02
2.8728	1.2764	238.9	0.12686	2.7181E-02
2.6429	1.2653	261.1	0.13100	4.1262E-02
2.4251	1.2558	283.3	0.13484	6.1262E-02
2.2158	1.2476	305.6	0.13840	8.9183E-02
2.0114	1.2405	327.8	0.14170	0.12756
1.9101	1.2373	338.9	0.14325	0.15164
1.8087	1.2343	350.0	0.14473	0.17958
1.7069	1.2314	361.1	0.14616	0.21189
1.6040	1.2288	372.2	0.14753	0.24916
1.4463	1.2251	388.9	0.14948	0.31573
1.3376	1.2229	400.0	0.15072	0.36827
1.2247	1.2208	411.1	0.15190	0.42826
1.1060	1.2188	422.2	0.15303	0.49658
0.9788	1.2169	433.3	0.15412	0.57419
0.8389	1.2151	444.4	0.15516	0.62614
0.5843	1.2127	461.1	0.15664	0.86599
0.3341	1.2112	472.2	0.15757	0.93502
0.0000	1.2104	477.8	0.15802	1.0000

4. AFTERBODY FLOW FIELD PREDICTIONS

For the calculations presented all combustion gas thermodynamic data were de-
rived from the computer program of Ref. 6. Substitute gas thermodynamic data were
generated by the procedure described in Appendix A of Ref. 2. The flow fields, in-
cluding the presence of shock waves, were calculated using the two-dimensional, MOC
program of Ref. 5. The geometry of the afterbody and cowl surfaces is fiven below.
The coordinate system is shown in Figs. 23 and 24.

Cowl

$\bar{Y} = 1.0$ $0 \leq \bar{X} \leq 1.11$

$\bar{Y} = 0.4204 \bar{X}^2 - 0.933 \bar{X} + 1.518$ $1.11 \leq \bar{X} \leq 1.235$

$\bar{Y} = 0.1051 \bar{X} + 0.8768$ $1.235 \leq \bar{X} \leq 3.12$ (no wedge)

$\bar{Y} = 0.1051 \bar{X} + 0.8768$ $1.235 \leq \bar{X} \leq 2.6$ (wedge for 20° afterbody)

$\bar{Y} = -0.3443 \bar{X} + 2.0453$ $2.6 \leq \bar{X} \leq 4.0$

$\bar{Y} = 0.1051 \bar{X} + 0.8768$ $1.235 \leq \bar{X} \leq 2.6$ (wedge for 0° afterbody)

$\bar{Y} = -0.05241 \bar{X} + 1.2863$ $2.6 \leq \bar{X} \leq 3.5$

20° Afterbody

$\bar{Y} = (0.1736 - \bar{X}^2)^{\frac{1}{2}} - 0.4167$ $0 \leq \bar{X} \leq 0.1425$

$\bar{Y} = -0.3640 \bar{X} + 0.02674$ $0.1425 \leq \bar{X} \leq 21.67$

0° Afterbody

$\bar{Y} = 0.0$ $0 \leq \bar{X} \leq 21.67$

where $\bar{Y} = Y/Y_3$, $\bar{X} = X/Y_3$, and Y_3 is the height of the combustor exit. For our model $Y_3 = 1.524$ cm (0.6 inch). For the full scale vehicle we assumed $Y_3 = 30.48$ cm (1.0 foot).

As a result of these calculations we found that the basic afterbody flow field
and its pressure distribution were relatively insensitive to small changes in combus-
tion gas thermodynamic properties and combustor exit Mach number. This point was
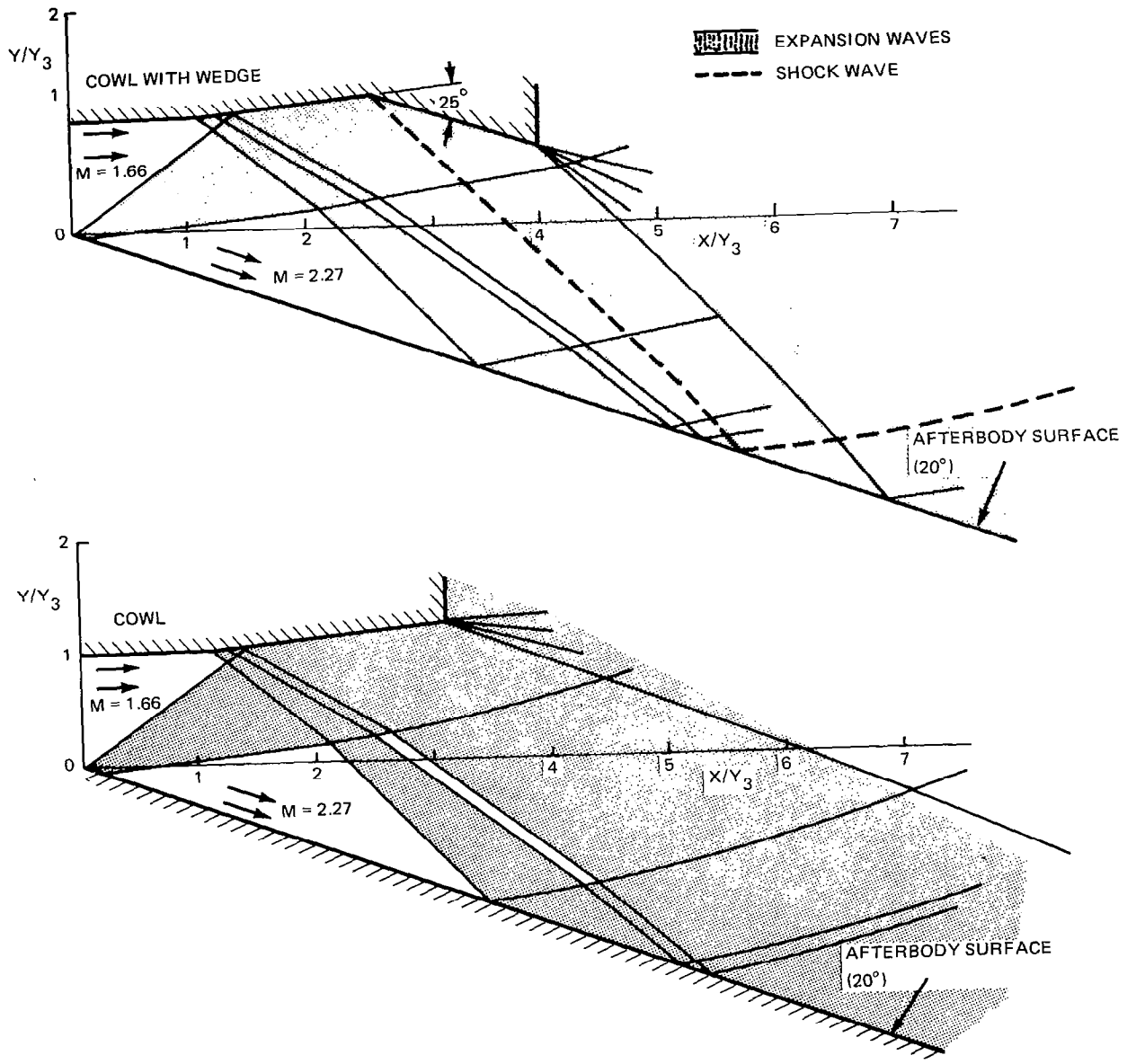
Fig. 23   Two-Dimensional Flow Field for 20° Afterbody with and without Shock Generator. Combustion Gas, $\alpha + \beta =$ 4°, $M_\infty = 6$
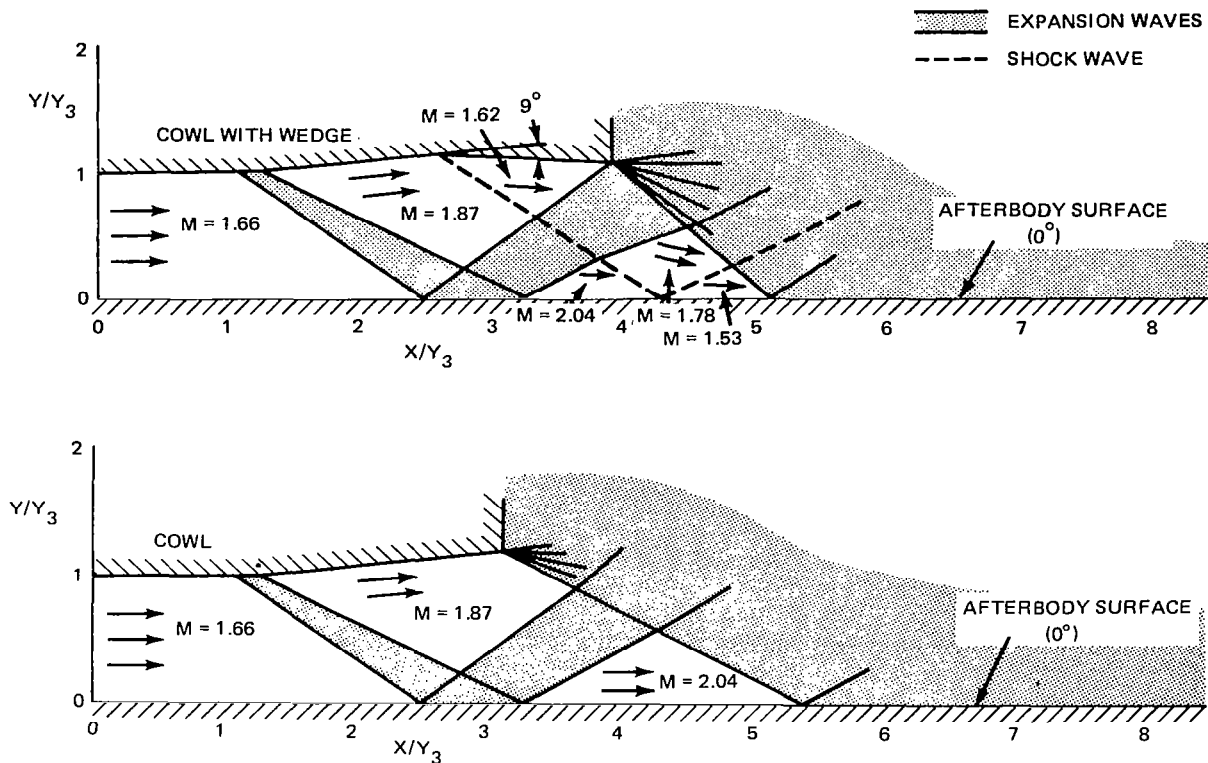
Fig. 24 Two-Dimensional Flow Field for $0°$ Afterbody with and without Shock Generator. Combustion Gas, $\alpha + \beta = 4°$, $M_\infty = 6$

clearly illustrated in Fig. 15 of our previous contractor report (Ref. 2). The same was true of small changes in substitute gas properties. We also found that the pressure distribution for the substitute gas chosen for the present tests (50% Freon 13B1 + 50% Argon) and for the combustion gas were in extremely close agreement. Therefore, in Figs. 23 and 24 we show only one flow field calculation for each geometry involved and in Figs. 26 through 58, where the experimental data are also plotted, only one theoretical, two-dimensional pressure distribution is shown. Figure 25 shows an oscilloscope record of detonation tube stagnation pressure with burning behind reflected shock and overly delayed detonation.

Because this model had a reflection plane extending the entire length of one side and a side plate extending to the end of the cowl on the other side, almost all of the data were obtained in two-dimensional flow regions and no theoretical corrections for side expansion effects are shown.

Theoretical heat transfer distributions for the afterbody without externally generated shocks were calculated for us by the NASA Langley Research Center using the computer code of Price and Harris (Ref. 11) for turbulent boundary layers, and assuming combustion gas products with the pressure distributions shown in Figs. 26 through 58. The calculations are shown in Figs. 59 through 73. Calculations assuming a laminar boundary layer predicted heating rates an order of magnitude lower than the turbulent cases.

As part of the contract extension, afterbody flow fields with the cowl shock impinging on the 20° afterbody were computed for the five additional substitute gases listed on pages 13 and 14. The objective here was to predict the sensitivity of the shock impingement location with variations in substitute gas properties and then verify the results experimentally. Since we would be testing with a fixed contour combustor nozzle, variations in substitute gas properties would produce variations in the combustor nozzle exit plane Mach number and γ. These latter variations were taken into account when doing the afterbody calculations. The calculated flow fields were all very similar to those shown in Fig. 23, and the predicted changes in shock impingement location were insignificant. Table 11 presents a summary of these calculations which shows how little the major parameters of the flow field are altered with the different substitute gases.

Since the calculations predicted insignificant changes in flow parameters in the different substitute gases, we selected only one of the five mixtures for the experimental tests. That gas was the mixture of 60% argon + 40% Freon 12 @ $T_5 = 477.8$ K and is referred to as substitute gas no. 2 in the Experimental Results Section (5).

Fig. 25   Oscilloscope Record of Detonation Tube Stagnation Pressure with Burning Behind Reflected Shock and Overly Delayed Detonation
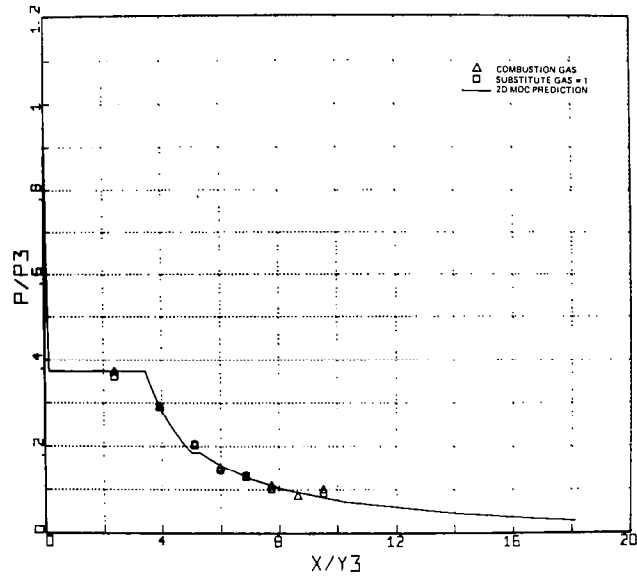
Fig. 26 Pressure Distribution: 20° Afterbody, No Shock Generators, Row A
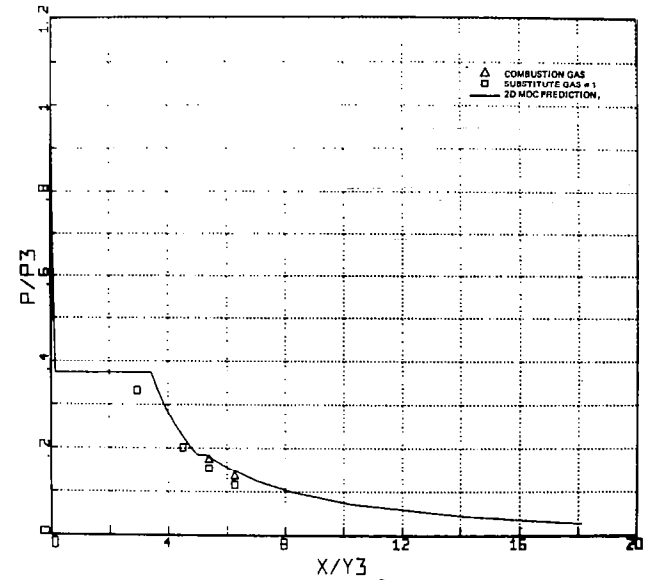
Fig. 28 Pressure Distribution: 20° Afterbody, No Shock Generators, Row C
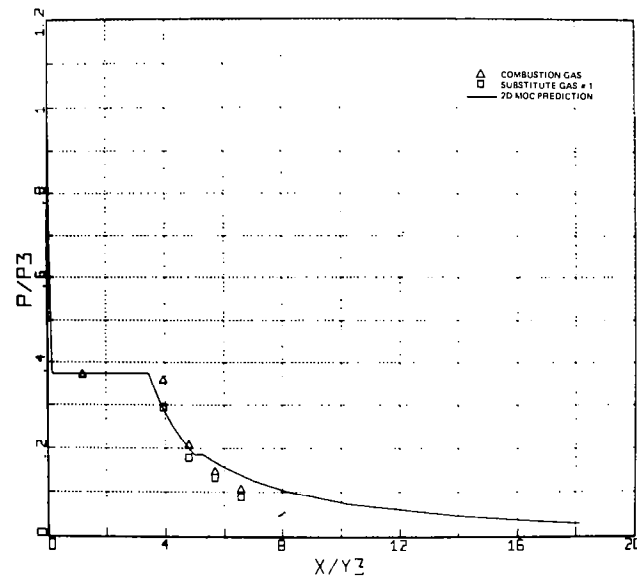
Fig. 27 Pressure Distribution: 20° Afterbody, No Shock Generators, Row B
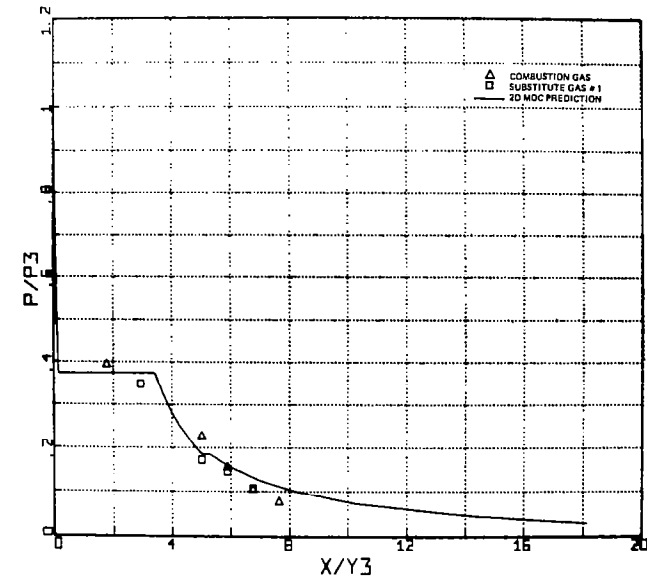
Fig. 29 Pressure Distribution: 20° Afterbody, No Shock Generators, Row D
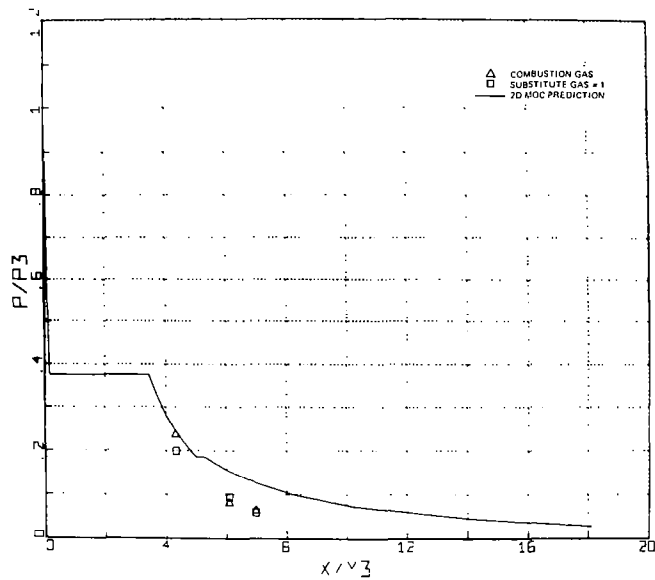
Fig. 30 Pressure Distribution: 20° Afterbody, No Shock
Generators, Row E
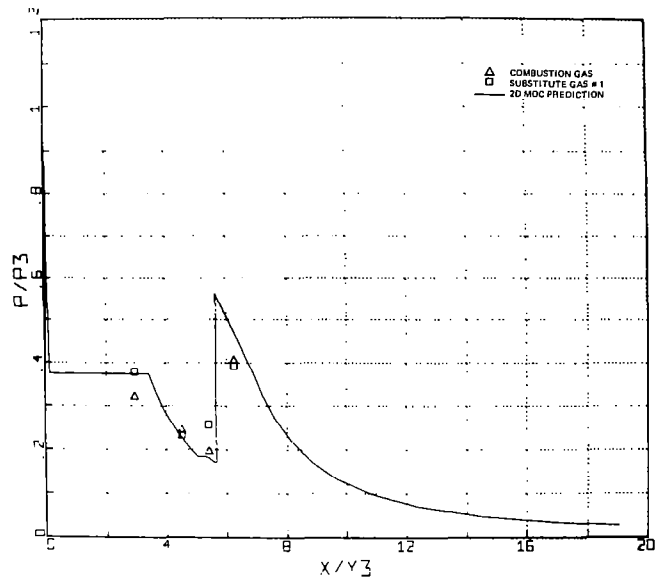
Fig. 32 Pressure Distribution: 20° Afterbody, with Top
(Cowl) Shock Generator, Row B
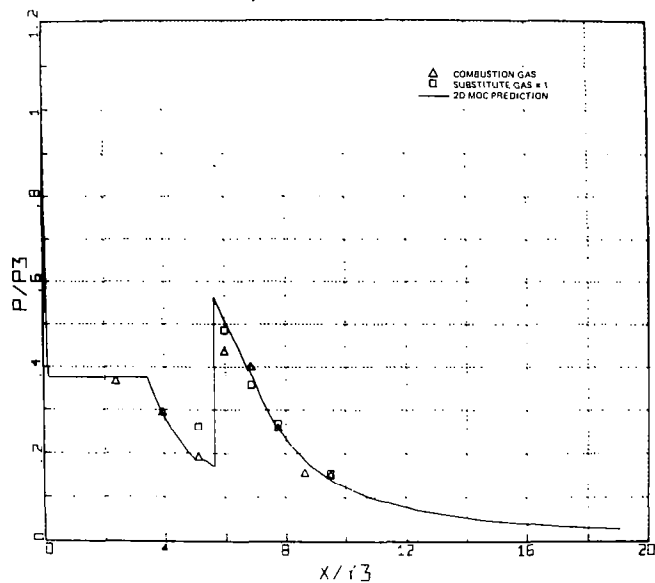
Fig. 31 Pressure Distribution: 20° Afterbody, with Top
(Cowl) Shock Generator, Row A
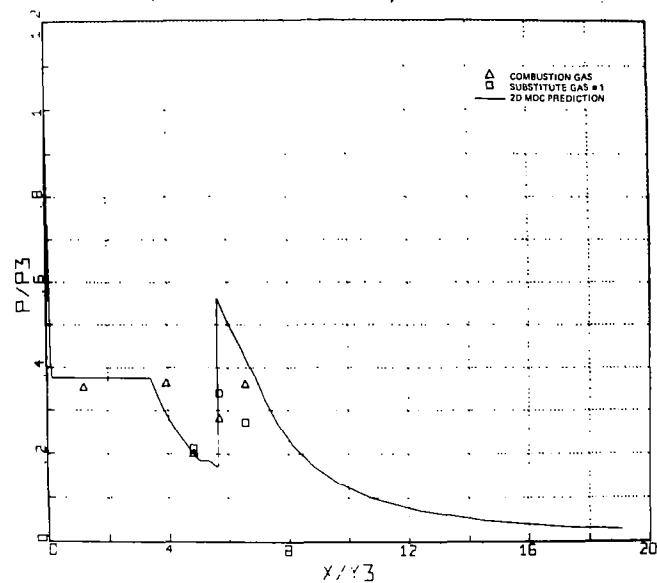
Fig. 33 Pressure Distribution: 20° Afterbody, with Top
(Cowl) Shock Generator, Row C

42
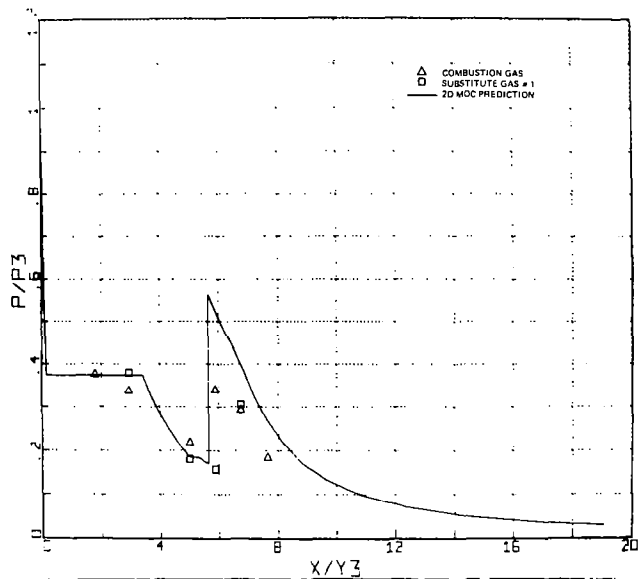
Fig. 34   Pressure Distribution: 20° Afterbody, with Top
(Cowl) Shock Generator, Row D
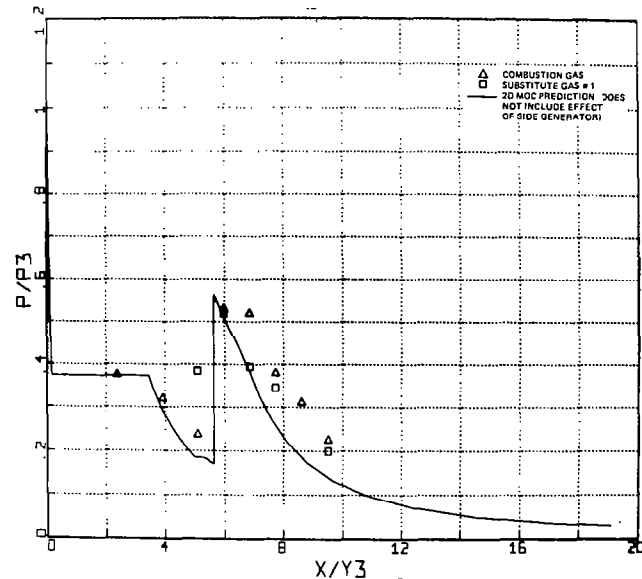
Fig. 36   Pressure Distribution: 20° Afterbody, with Top
and Side Shock Generators, Row A
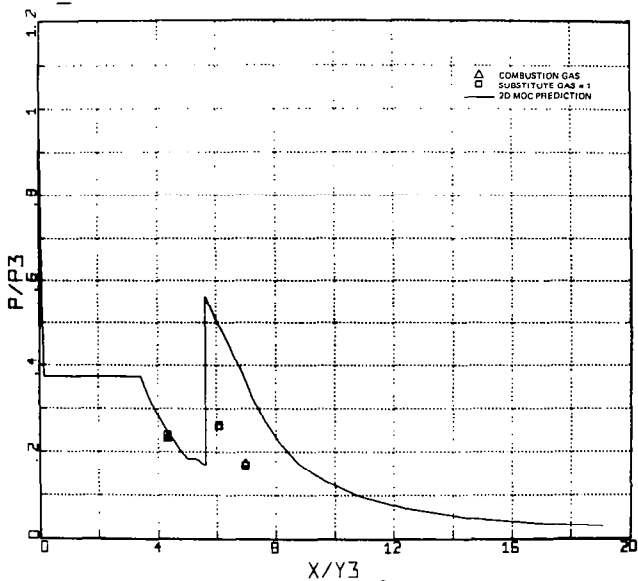
Fig. 35   Pressure Distribution: 20° Afterbody, with Top
(Cowl) Shock Generator, Row E
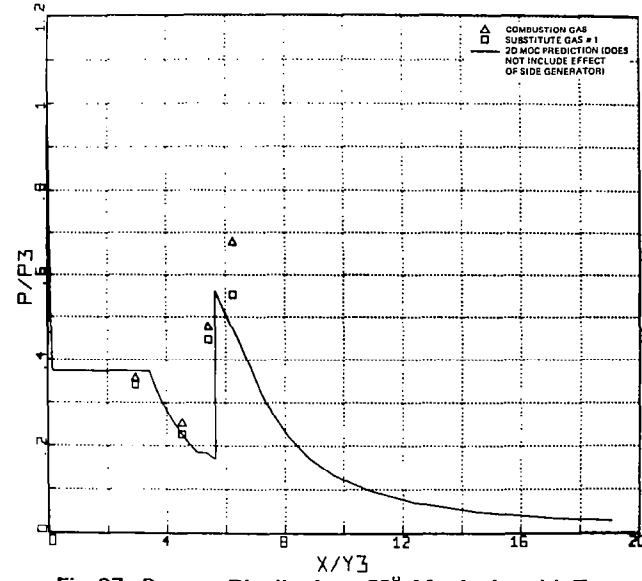
Fig. 37   Pressure Distribution: 20° Afterbody, with Top
and Side Shock Generators, Row B
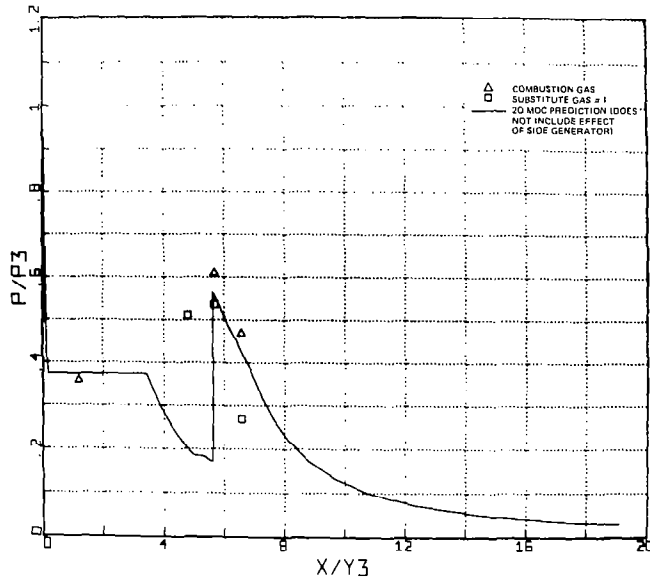
Fig. 38   Pressure Distribution: 20° Afterbody, with Top
and Side Shock Generators, Row C
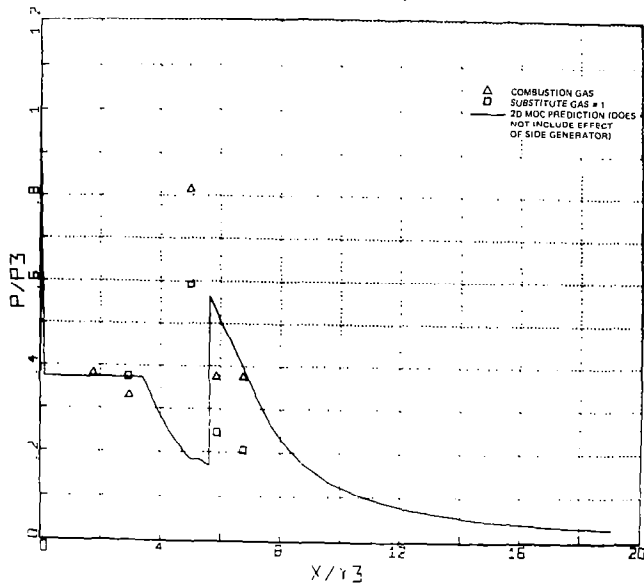
Fig. 39   Pressure Distribution: 20° Afterbody, with Top
and Side Shock Generators, Row D
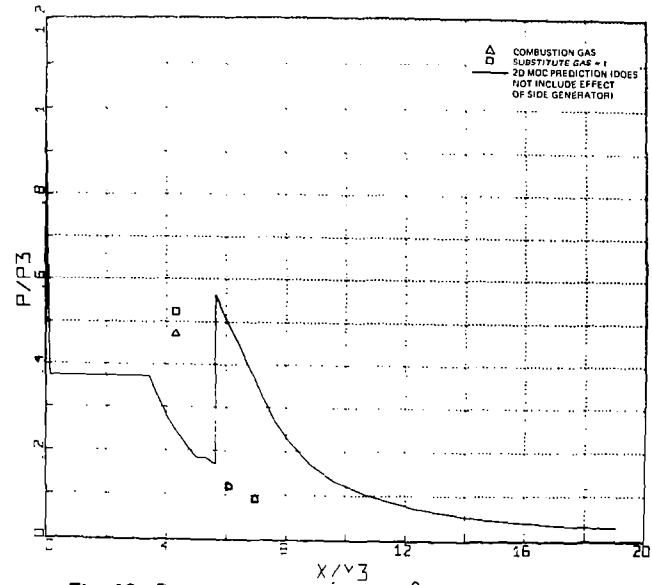
Fig. 40   Pressure Distribution: 20° Afterbody, with Top
and Side Shock Generators, Row E
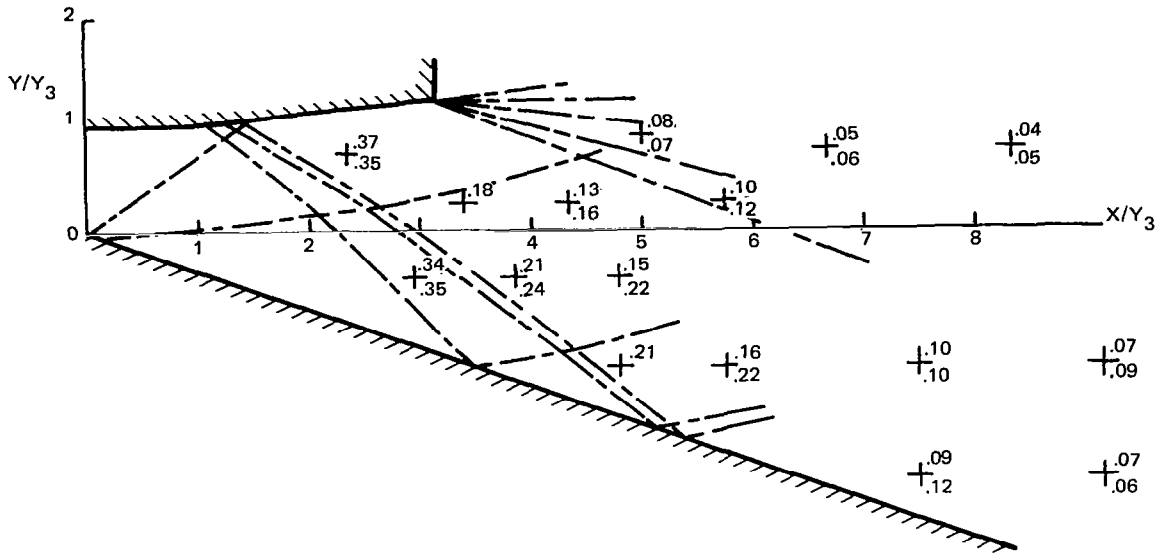
Fig. 41   Reflection Plane Normalized Pressures (P/P₃) 20° Afterbody, No Shock Generators
(Combustion Data Above Substitute Data)
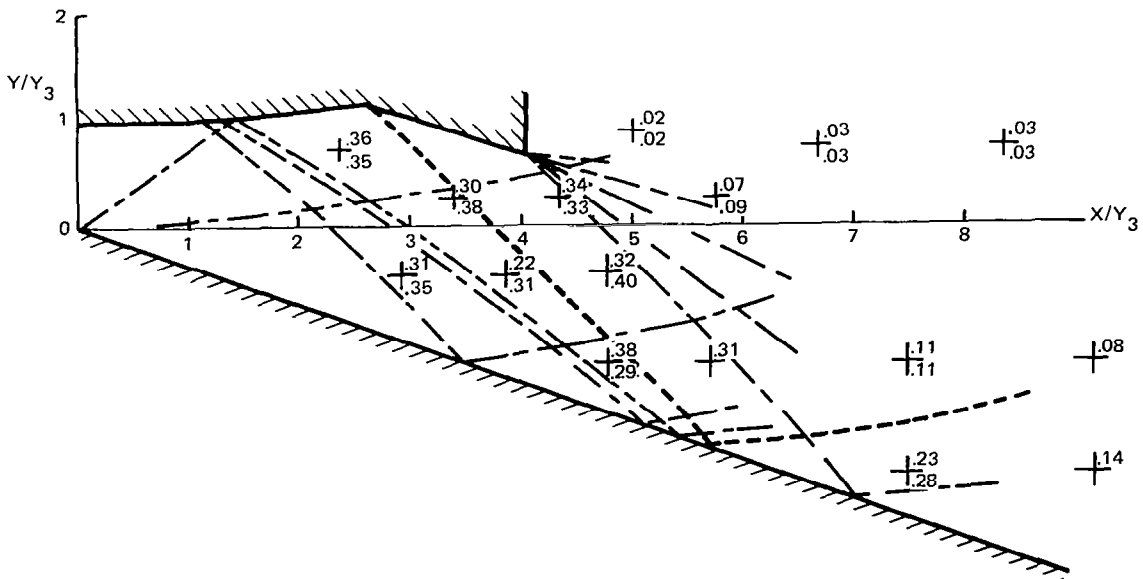
Fig. 42   Reflection Plane Normalized Pressures (P/P₃) 20° Afterbody, with Top (Cowl) Shock Generator
(Combustion Data Above Substitute Data)
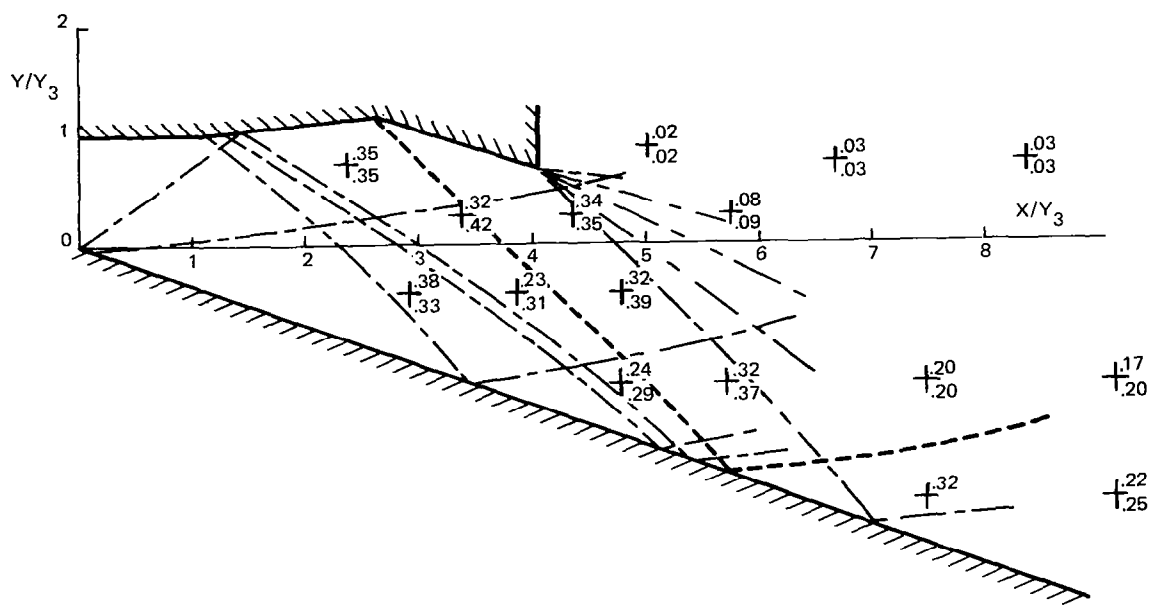
Fig. 43   Reflection Plane Normalized Pressures (P/P_3) $20°$ Afterbody, with Top and Side Shock Generators
(Combustion Data Above Substitute Data)

46
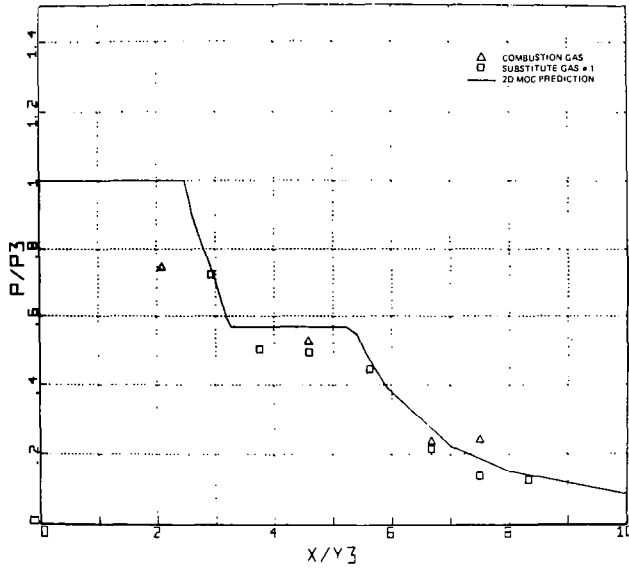
Fig. 44 Pressure Distribution: 0° Afterbody, No Shock Generators, Row A
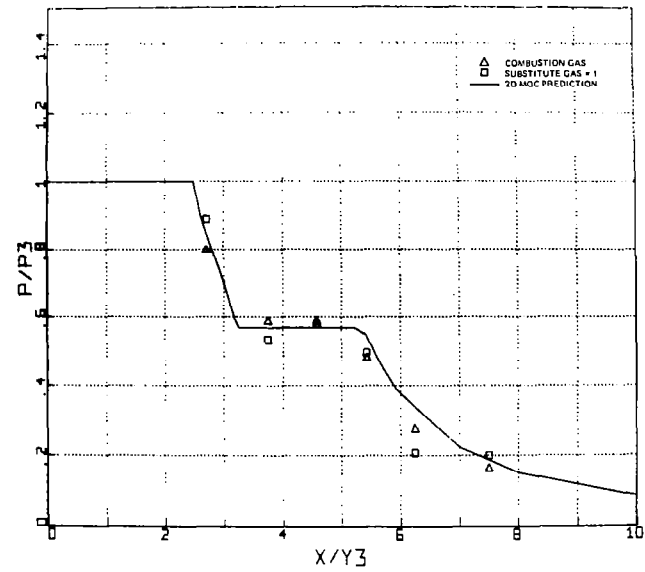
Fig. 46 Pressure Distribution: 0° Afterbody, No Shock Generators, Row C
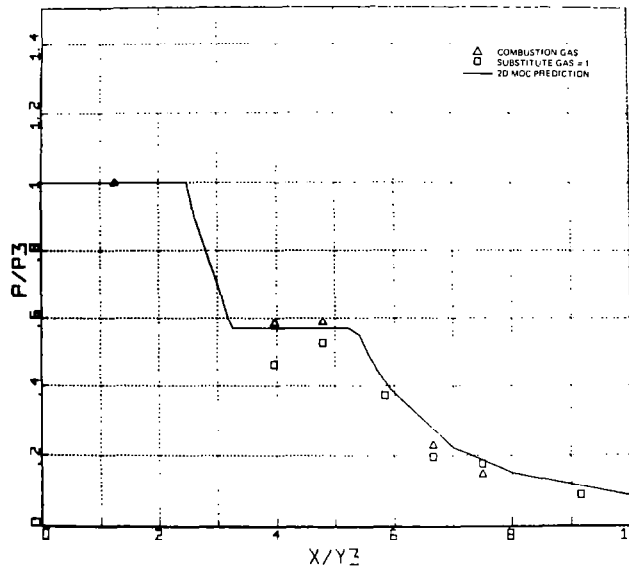
Fig. 45 Pressure Distribution: 0° Afterbody, No Shock Generators, Row B
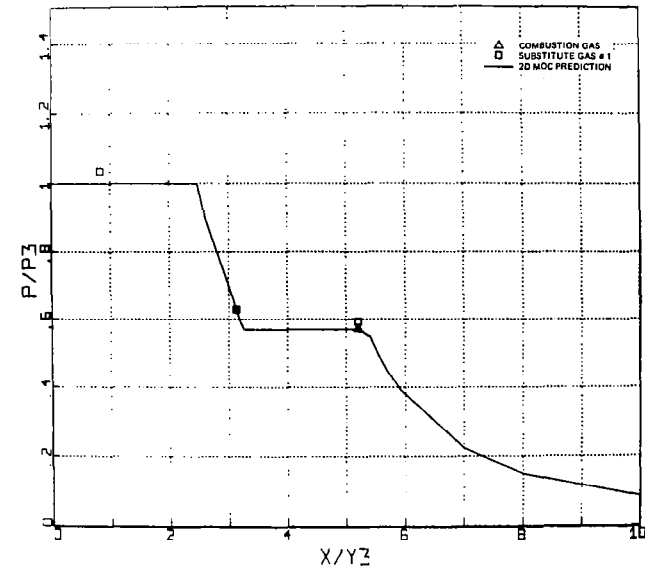
Fig. 47 Pressure Distribution: 0° Afterbody, No Shock Generators, Row D

47
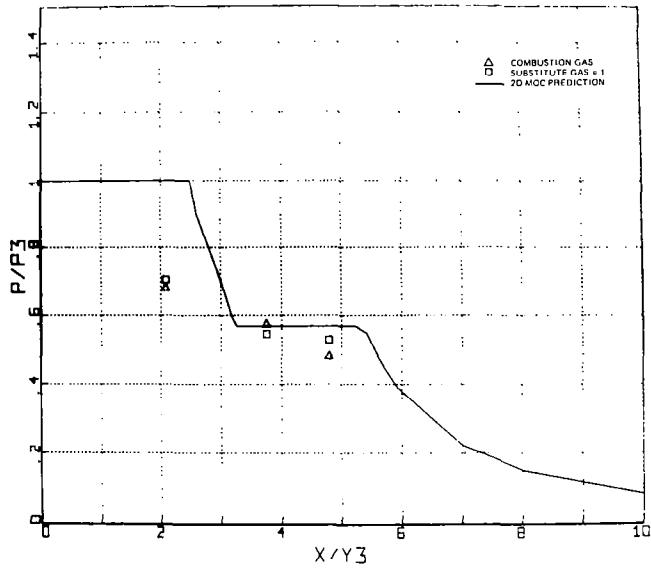
Fig. 48 Pressure Distribution: 0° Afterbody, No Shock
Generators, Row E
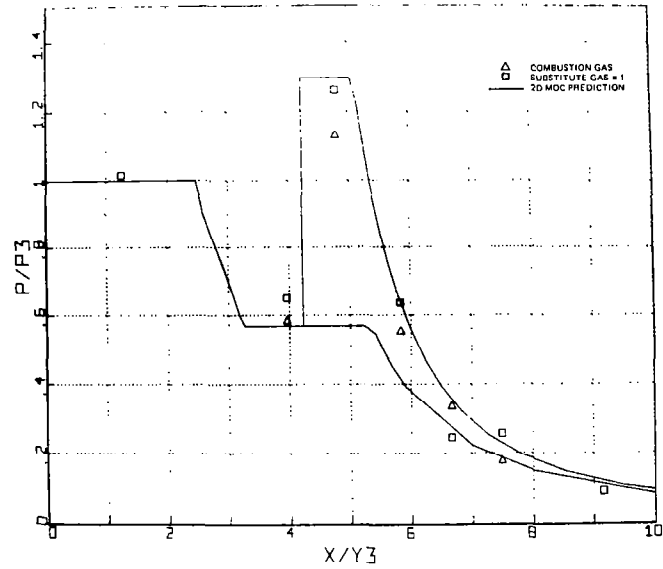
Fig. 50 Pressure Distribution: 0° Afterbody, with Top
(Cowl) Shock Generator, Row B
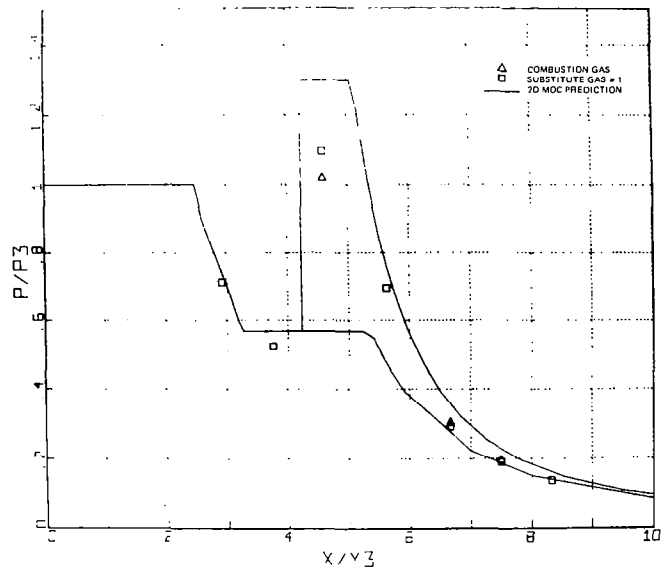
Fig. 49 Pressure Distribution: 0° Afterbody, with Top
(Cowl) Shock Generator, Row A
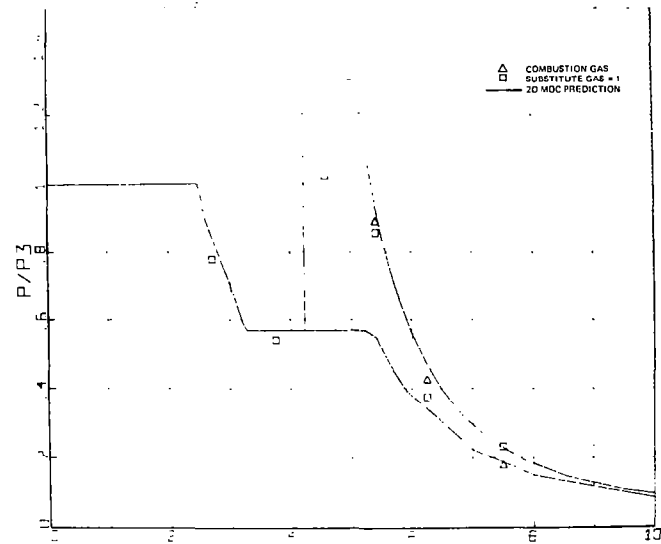
Fig. 51 Pressure Distribution: 0° Afterbody, with Top
(Cowl) Shock Generator, Row C
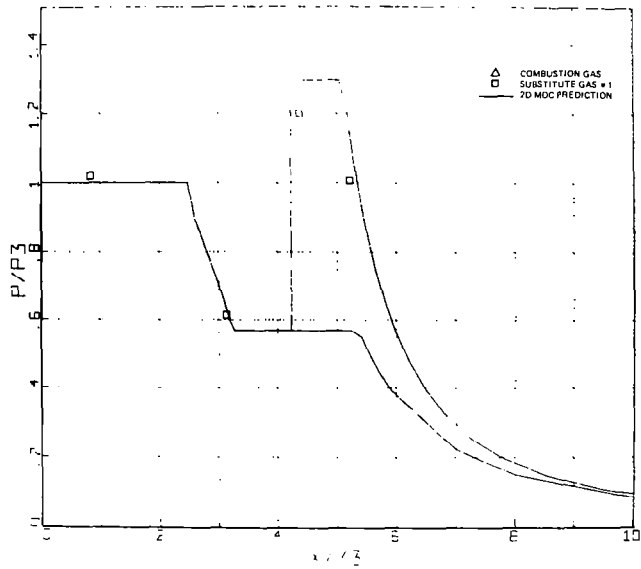
Fig. 52 Pressure Distribution: 0° Afterbody, with Top (Cowl) Shock Generator, Row D
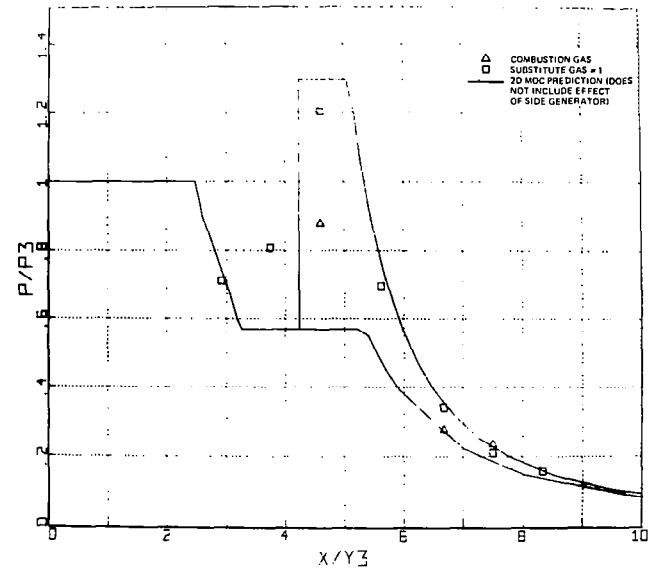
Fig. 54 Pressure Distribution: 0° Afterbody, with Top and Side Shock Generators, Row A
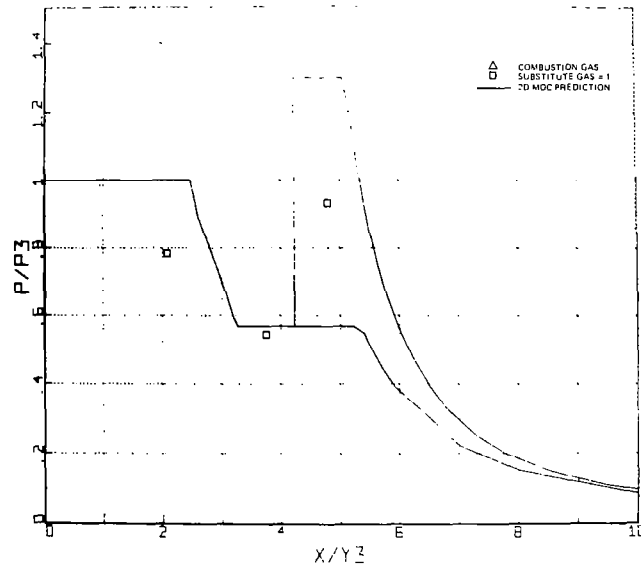
Fig. 53 Pressure Distribution: 0° Afterbody, with Top (Cowl) Shock Generator, Row E
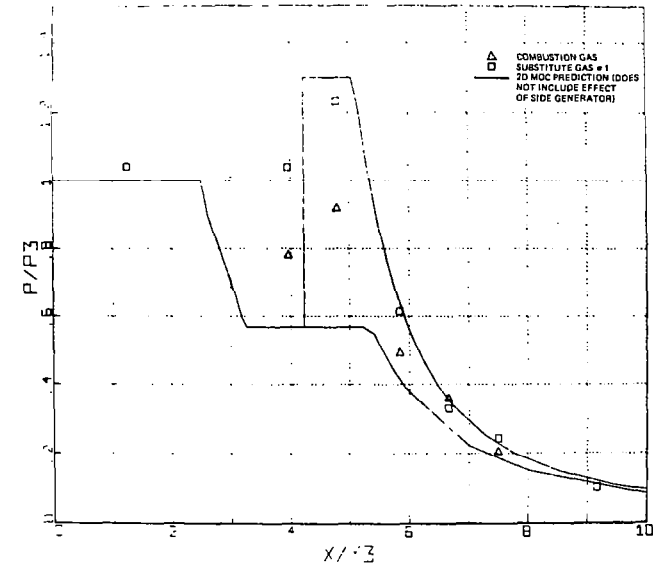
Fig. 55 Pressure Distribution: 0° Afterbody, with Top and Side Shock Generators, Row B
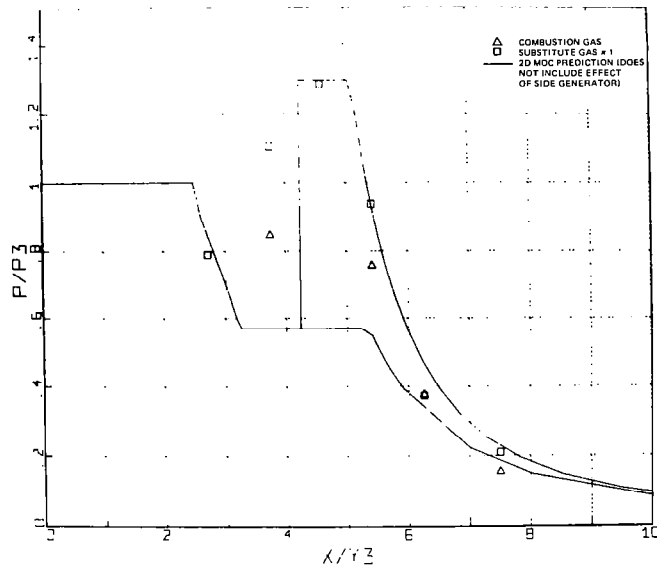
Fig. 56   Pressure Distribution: 0° Afterbody, woth Top
and Side Shock Generators, Row C
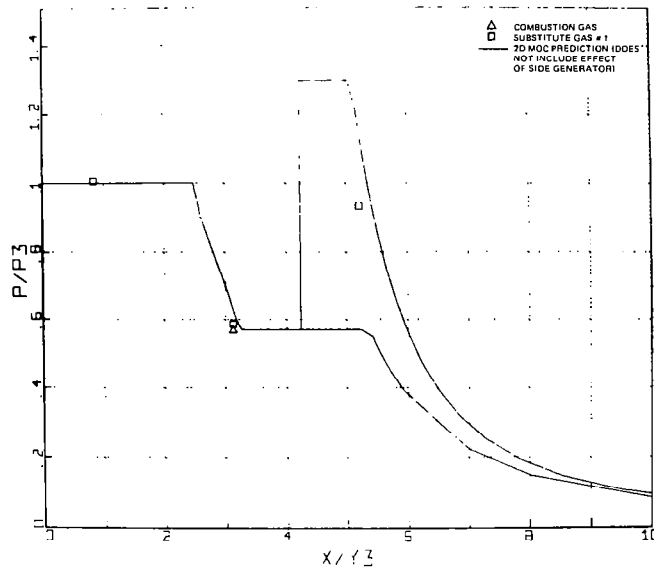
Fig. 57   Pressure Distribution: 0° Afterbody, with Top
and Side Shock Generators, Row D
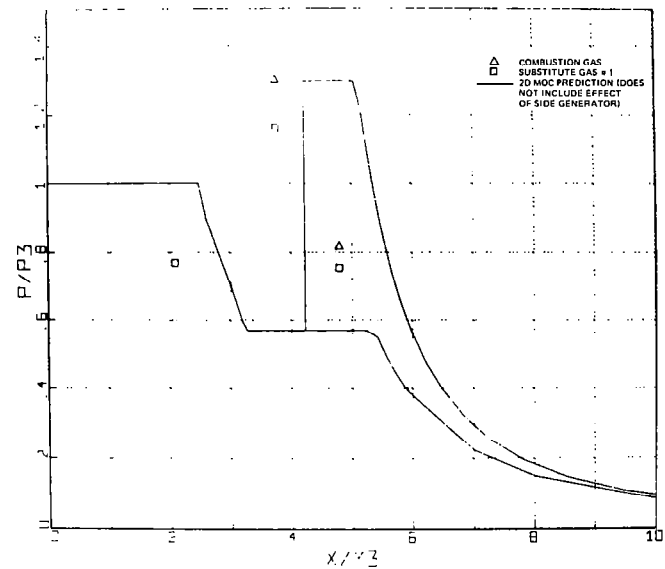
Fig. 58   Pressure Distribution: 0° Afterbody, with Top
and Side Shock Generators, Row E
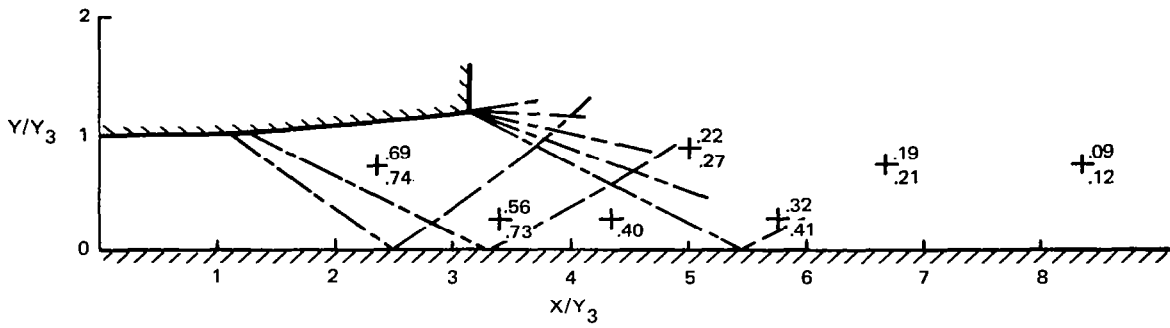
Fig. 59   Reflection Plane Normalized Pressures (P/P_3) $0°$ Afterbody, No Shock Generator
(Combustion Data Above Substitute Data)
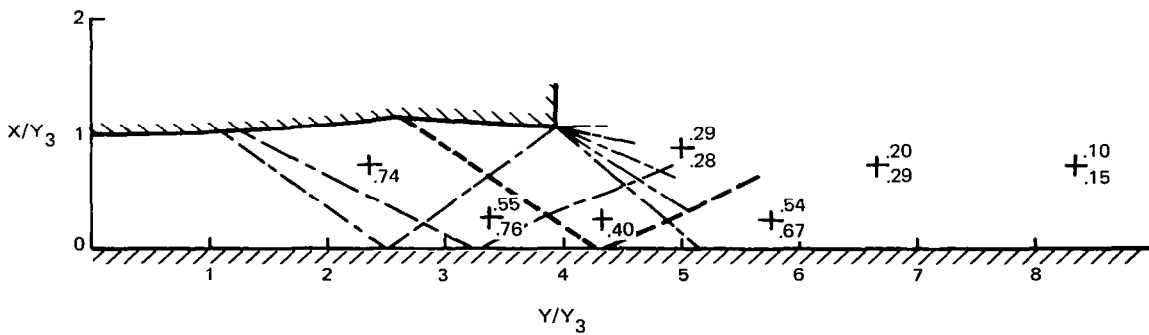
Fig. 60   Reflection Plane Normalized Pressures (P/P_3) $0°$ Afterbody, with Top (Cowl) Shock Generator
(Combustion Data Above Substitute Data)

51
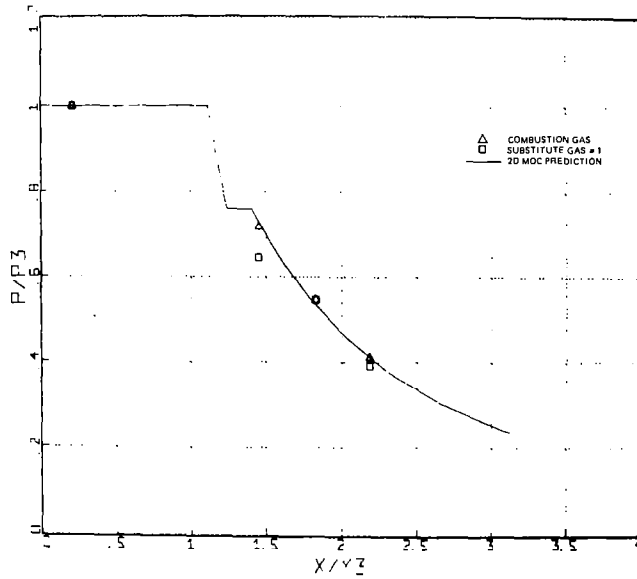
Fig. 61   Cowl Pressure Distribution with 20° Afterbody
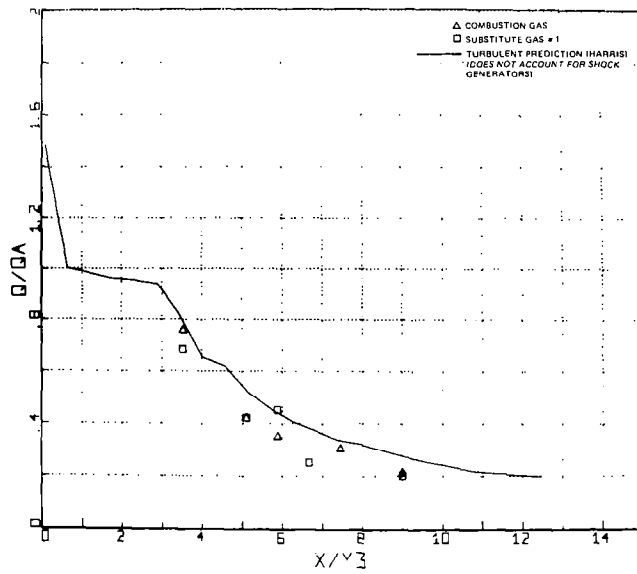
Fig. 62   Heat Transfer Rate Distribution, 20° Afterbody,
No Shock Generators, Row A

Fig. 63   Heat Transfer Rate Distribution, 20° Afterbody,
No Shock Generators, Row B
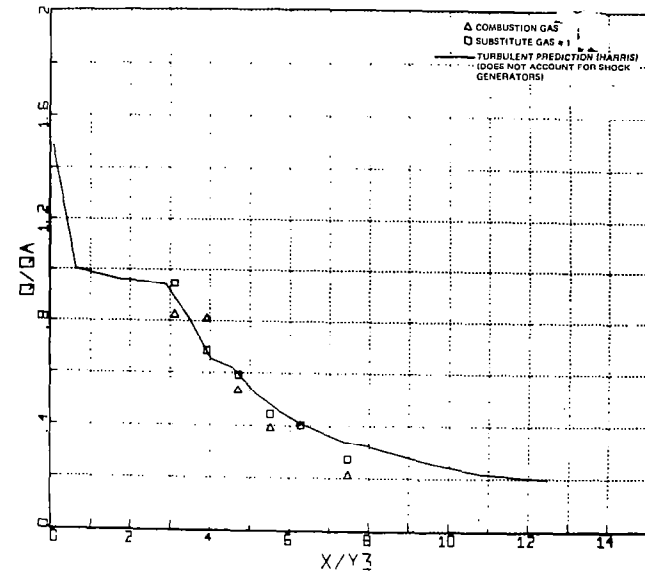
Fig. 64   Heat Transfer Rate Distribution, 20° Afterbody,
No Shock Generators, Row C
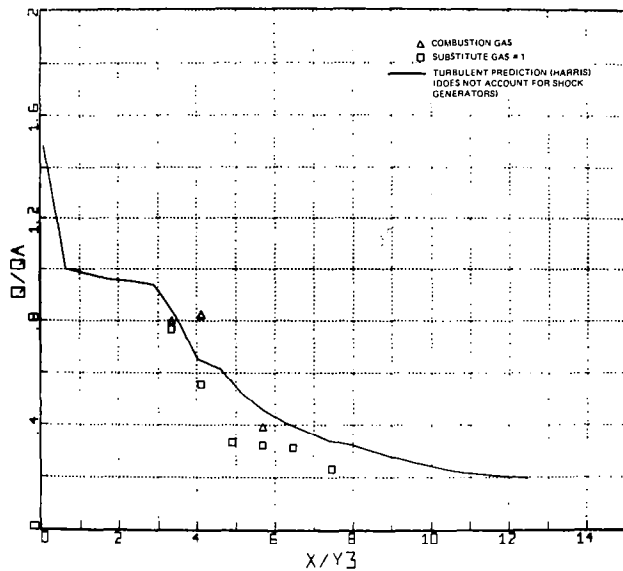
Fig. 65 Heat Transfer Rate Distribution, 20° Afterbody,
No Shock Generators, Row D

Fig. 66 Heat Transfer Rate Distribution, 20° Afterbody,
No Shock Generators, Row E
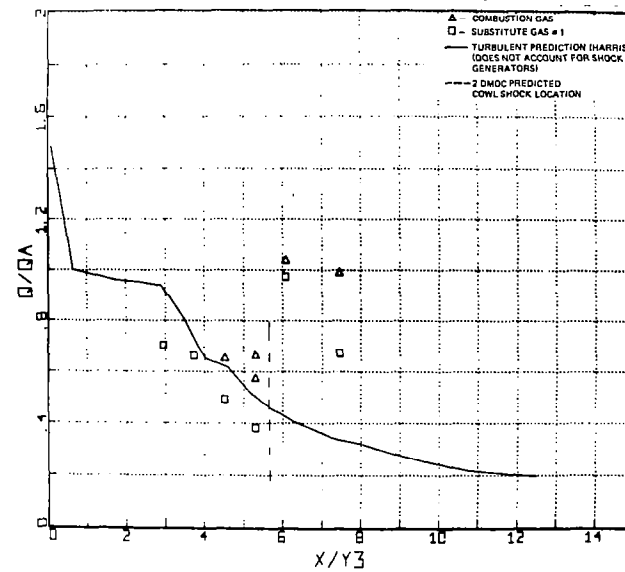
Fig. 67 Heat Transfer Rate Distribution, 20° Afterbody,
with Top (Cowl) Shock Generator, Row A

Fig. 68 Heat Transfer Rate Distribution, 20° Afterbody,
with Top (Cowl) Shock Generator, Row B
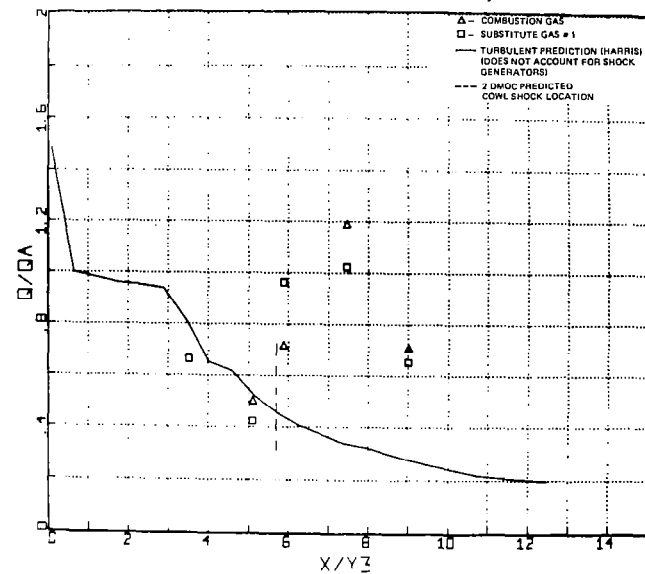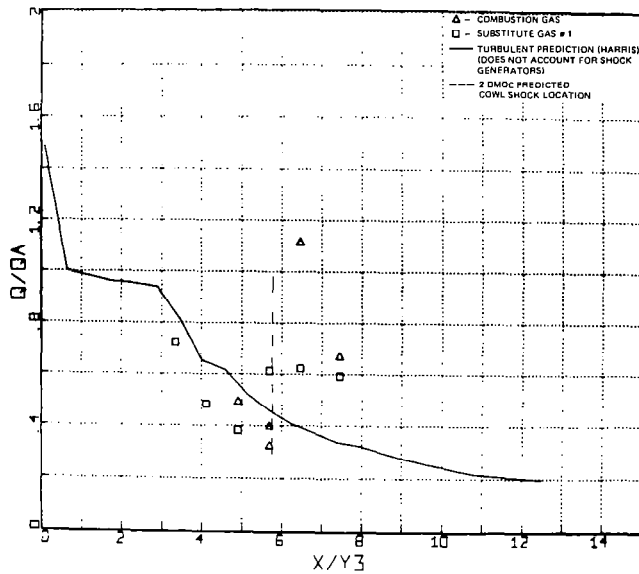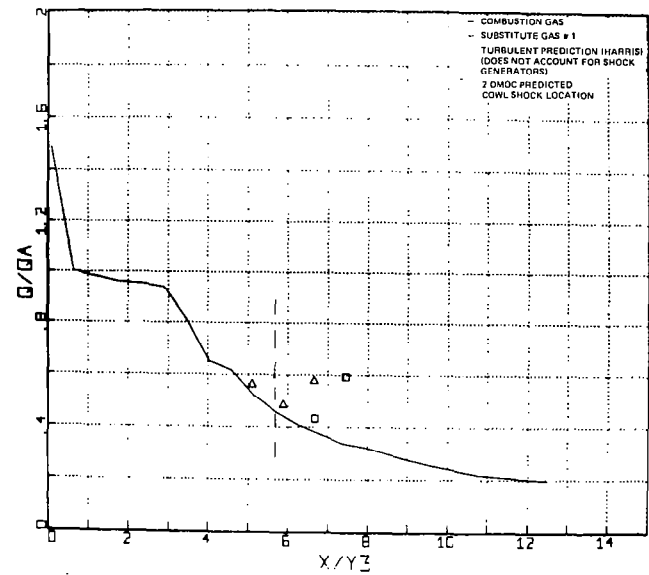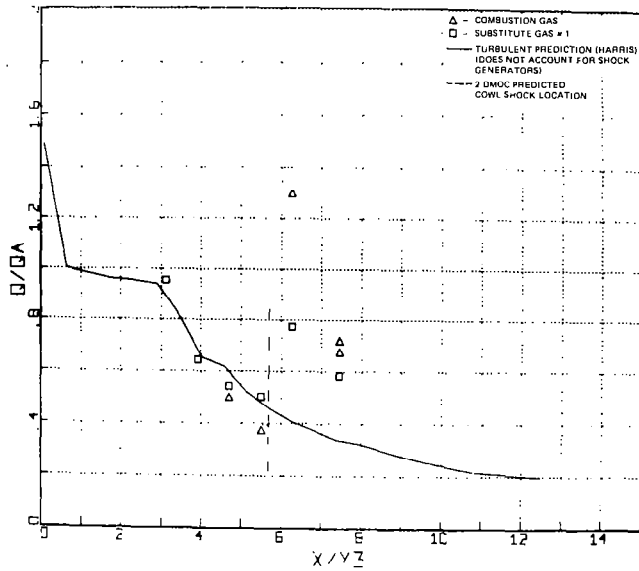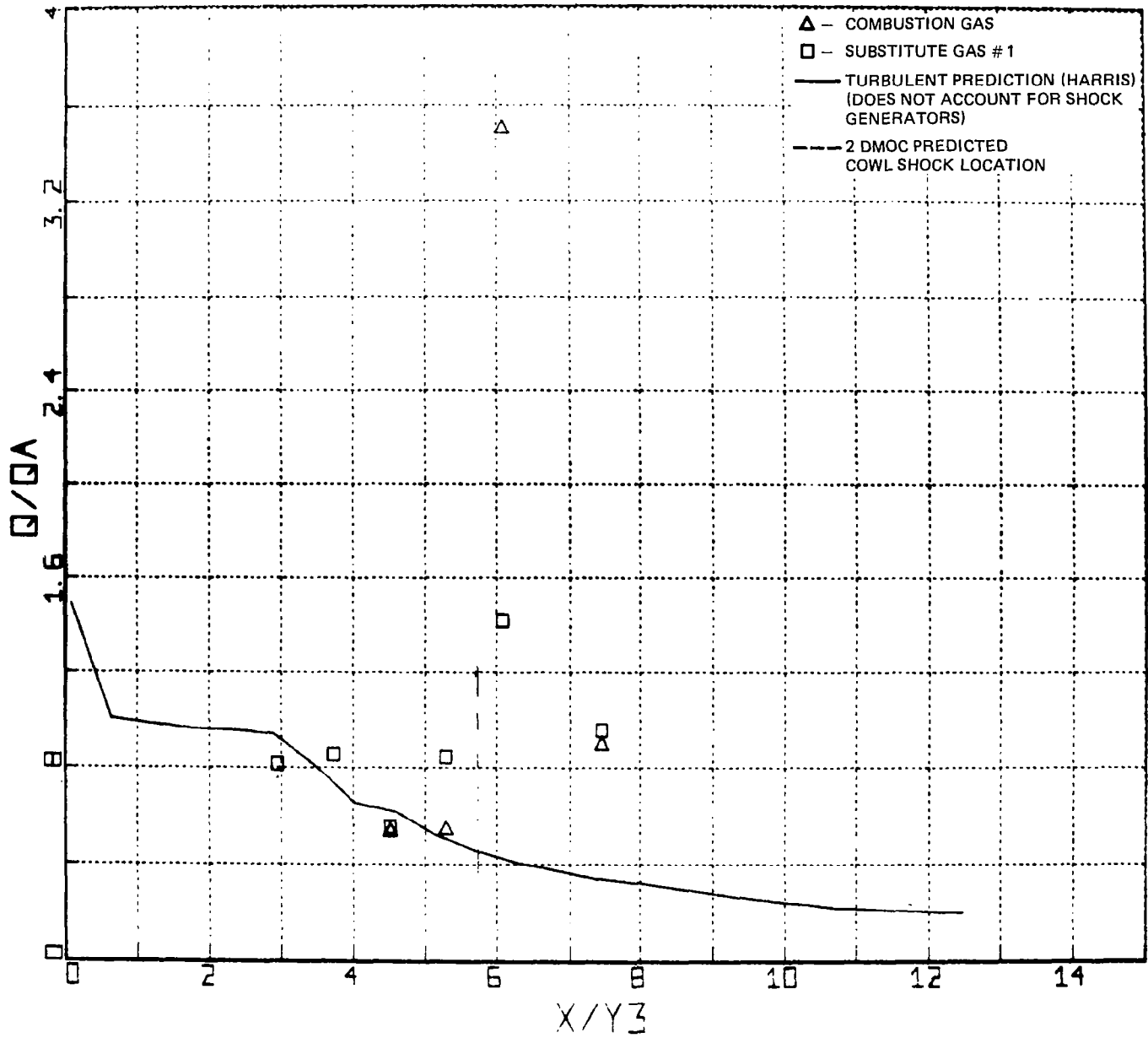
Fig. 69 Heat Transfer Rate Distribution, 20° Afterbody, with Top (Cowl) Shock Generator, Row C

Fig. 70 Heat Transfer Rate Distribution, 20° Afterbody, with Top (Cowl) Shock Generator, Row D

Fig. 71 Heat Transfer Rate Distribution, 20° Afterbody, with Top (Cowl) Shock Generator, Row E

Fig. 72 Heat Transfer Rate Distribution, 20° Afterbody, with Top and Side Shock Generators, Row A

Fig. 73 Heat Transfer Rate Distribution, 20° Afterbody, with Top and Side Shock Generators, Row B

NOZZLE EXIT PLANE
COWL
25°
SHOCK GENERATOR
6°
REGION ③
SHOCK WAVE
REGION ④
20°
AFTERBODY
Y
X
REFLECTED SHOCK REGION
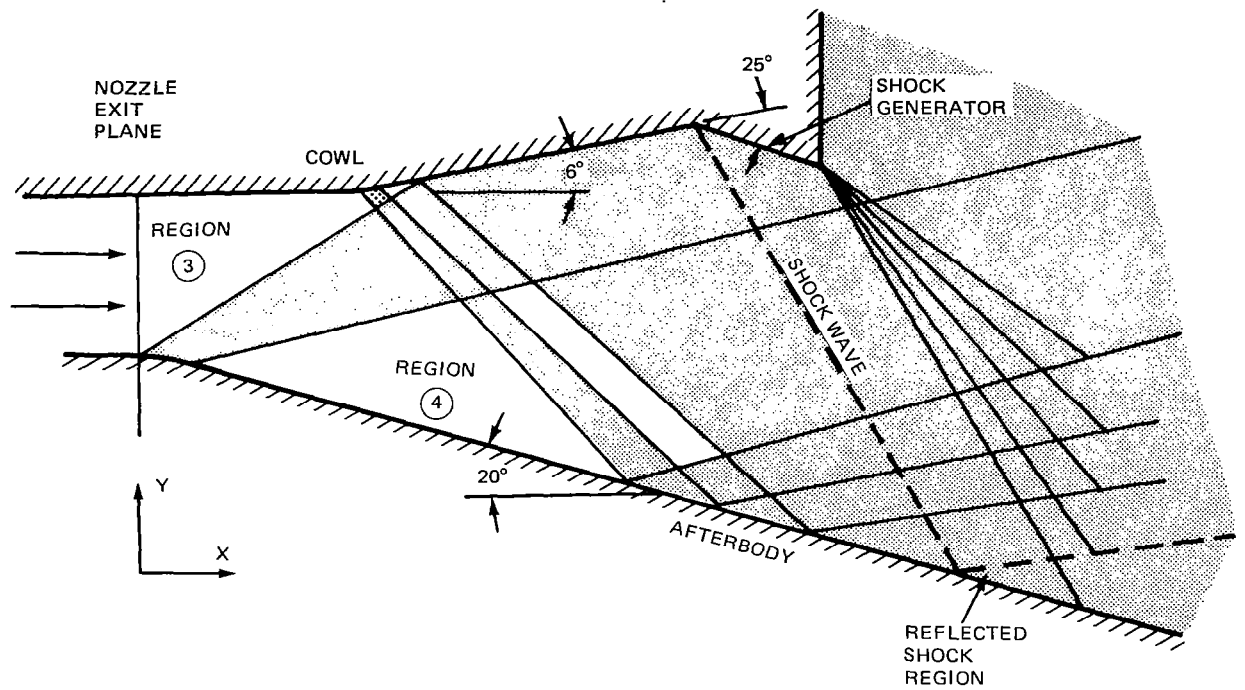
TABLE 11 COMPARISON OF VARIOUS FLOW FIELD PARAMETERS
FOR DIFFERENT SUBSTITUTE GASES AND COMBUSTION GAS

|	1/8 Scale Combustion Gas $+ \beta = 4°$		0.5F-13B1 + 0.5Ar Substitute Gas No. 1		0.4F-12 + 0.6Ar Substitute Gas No. 2		0.4F-13B1 + 0.6Ar Substitute Gas No. 5	
	Desired Equilibrium	Nozzle Equilibrium	To (K)					
			477.8	533.3	477.8	533.3	477.8	533.3
M_3	1.657	1.702	1.705	1.702	1.713	1.711	1.716	1.713
$\dfrac{P_4}{P_3}$	0.3792	0.3730	0.3773	0.3812	0.3667	0.3708	0.3620	0.3670
M_4	2.220	2.270	2.269	2.259	2.299	2.289	2.309	2.299
$\dfrac{P_{R.S.}}{P_3}$	0.5364	0.5619	0.5651	0.5639	0.5713	0.5698	0.5735	0.5718
$M_{R.S.}$	1.996	2.011	2.014	2.013	2.016	2.016	2.016	2.016
$\dfrac{X_{R.S.}}{Y_3}$	5.6435	5.6417	5.6424	5.6410	5.6502	5.6475	5.6488	5.6494

NOTE: Subscript R.S. refers to the reflected shock region

56

5. EXPERIMENTAL RESULTS

PRESSURE DATA

All afterbody pressure data are presented by rows and normalized to P_3, the nozzle exit static pressure, which is different for combustion and substitute gas. Figures 26-30 show the pressure distribution for the 1/20 scale 20° afterbody with no shock generators. These data show excellent agreement between the substitute and combustion gases. There is also good agreement with the 2-D prediction for gauge rows close to the reflection plane. The gauge rows farthest from the reflection plane deviate most from the 2-D prediction, particularly at large values of X/Y_3 (length along afterbody normalized by combustor nozzle exit height). This is the expected behavior since it is in this region that deviation from 2-D behavior will be greatest. Reflection plane data for this configuration, Fig. 41, are presented in schematic form. The combustion data are the upper numbers while the substitute gas data are the lower. These data show the same good agreement between substitute and combustion gases as the afterbody data.

Pressure distributions for the 20° afterbody with the cowl generator and both test media are shown in Fig. 31-35. The agreement between substitute and combustion gas data is good but the shock arrival is slightly farther downstream for the combustion gas. The substitute gas shock arrival is in close agreement with the 2-D prediction and both pressure distributions show the same kind of deviation from 2-D behavior as in the no-generator case. The reflection plane data, Fig. 42, show the same agreement between test media and indicate the shift in cowl shock location for the combustion gas.

Figures 36-40 show the 20° afterbody pressure distributions with both shock generators and both gases. The 2-D distribution on these figures is included only for reference, since it does not allow for the side shock. The data for this condition appear to show poorer agreement between gases than for the previous configurations,

but these differences are due to differences in cowl shock location for different gauge stations. The intersection of the two shocks gives rise to the highest pressures measured on the 20° afterbody; however the absolute level of these pressures is the average pressure on the gauge diaphragm and not a true "point" maximum. Since all pressure measurements are averaged over the 3.175 mm diameter diaphragm, flow fields with strong pressure gradients, i.e. shocks, will yield measured pressures different from the actual pressure at a point. Both these data and the reflection plane data, Fig. 43, indicate a merging of the side and cowl shocks at their point of intersection since there is no localized pressure increase after the cowl shock in row A or on the reflection plane.

The data in Figs. 44-60 are for the 0° afterbody. These data show reasonably good agreement between the two test media and also between both gases and the 2-D prediction. There is more scatter for these data than for the 20° afterbody because of the very high heating rates for the combustion gas. Even though the pressure transducer diaphragms were protected by an ablative silicone coating, many gauges were destroyed in these tests, particularly those close to the nozzle exit plane. Data from gauges that were destroyed by these heating rates could still be reduced provided the gauges were intact for the greater part of the steady flow time (3 msec). Destruction of a gauge is easily recognized on the signal. Pressure distributions for the combustion gas on the 0° afterbody are not as complete as for the 20° afterbody because of severe gauge attrition; however Figs. 49-53 indicate the cowl shock for the combustion gas is farther downstream than the substitute gas cowl shock, as was the case with the 20° afterbody.

Cowl pressure data (Fig. 61) show very good agreement between experiments and prediction as well as good agreement between the two gases. Pressure data in tabular form as a function of X/Y_3 for both the 20° and 0° afterbody models in both combustion and substitute gas are presented in Tables 12 through 15.

During the contract extension pressure measurements with substitute gas no. 2 were made on the afterbody to determine shock location. No separators were installed for these runs. The afterbody pressures appear in Table 16 and show good agreement with the No. 1 substitute gas pressures since both the shock location and normalized pressure levels agree with the previous tests. Cowl pressures with substitute gas no. 2 were measured on the nozzle separator center lines just aft

58

TABLE 12 Ṗ/P3 20 DEG AFT BODY COMBUSTION GAS

----ROW A----

NO GENERATORS		TOP GENERATOR		BOTH GENERATORS	
X/Y3	P/P3	X/Y3	P/P3	X/Y3	P/P3
2.36	0.37	2.36	0.36	2.36	0.37
3.92	0.29	3.92	0.29	3.92	0.32
5.10	0.20	5.10	0.19	5.10	0.24
5.98	0.15	5.98	0.43	5.98	0.53
6.86	0.13	6.86	0.40	6.86	0.52
7.74	0.11	7.74	0.26	7.74	0.38
8.62	0.08	8.62	0.15	8.62	0.31
9.50	0.10	9.50	0.15	9.50	0.22

----ROW B----

NO GENERATORS		TOP GENERATOR		BOTH GENERATORS	
X/Y3	P/P3	X/Y3	P/P3	X/Y3	P/P3
5.39	0.17	2.95	0.32	2.95	0.36
6.26	0.13	4.51	0.24	4.51	0.25
		5.39	0.19	5.39	0.48
		6.26	0.40	6.26	0.68

----ROW C----

NO GENERATORS		TOP GENERATOR		BOTH GENERATORS	
X/Y3	P/P3	X/Y3	P/P3	X/Y3	P/P3
1.18	0.37	1.18	0.35	1.18	0.36
3.92	0.36	3.92	0.36	5.68	0.61
4.80	0.21	4.80	0.20	6.57	0.47
5.68	0.14	5.68	0.28		
6.57	0.10	6.57	0.36		

----ROW D----

NO GENERATORS		TOP GENERATOR		BOTH GENERATORS	
X/Y3	P/P3	X/Y3	P/P3	X/Y3	P/P3
1.77	0.39	1.77	0.37	1.77	0.38
2.95	0.35	2.95	0.34	2.95	0.33
5.00	0.23	5.00	0.22	5.00	0.81
5.88	0.16	5.88	0.34	5.88	0.37
6.76	0.10	6.76	0.29	6.76	0.37
7.64	0.07	7.64	0.18		

----ROW E----

NO GENERATORS		TOP GENERATOR		BOTH GENERATORS	
X/Y3	P/P3	X/Y3	P/P3	X/Y3	P/P3
4.32	0.23	4.32	0.23	4.32	0.47
6.09	0.08	6.09	0.26	6.09	0.12
6.96	0.06	6.96	0.17	6.96	0.09

TABLE 13 P/P3 20 DEG AFT BODY SUBSTITUTE GAS

----ROW A----

NO GENERATORS		TOP GENERATOR		BOTH GENERATORS	
X/Y3	P/P3	X/Y3	P/P3	X/Y3	P/P3
2.36	0.36	5.10	0.26	5.10	0.38
3.92	0.29	5.98	0.48	5.98	0.52
5.10	0.20	6.86	0.36	6.86	0.39
5.98	0.14	7.74	0.27	7.74	0.35
6.86	0.13	9.50	0.15	9.50	0.20
7.74	0.10				
9.50	0.09				

----ROW B----

NO GENERATORS		TOP GENERATOR		BOTH GENERATORS	
X/Y3	P/P3	X/Y3	P/P3	X/Y3	P/P3
2.95	0.33	2.95	0.38	2.95	0.34
4.51	0.20	4.51	0.23	4.51	0.23
5.39	0.15	5.39	0.26	5.39	0.45
6.26	0.11	6.26	0.39	6.26	0.55

----ROW C----

NO GENERATORS		TOP GENERATOR		BOTH GENERATORS	
X/Y3	P/P3	X/Y3	P/P3	X/Y3	P/P3
3.92	0.29	4.80	0.21	4.80	0.51
4.80	0.18	5.68	0.34	5.68	0.53
5.68	0.13	6.57	0.27	6.57	0.27
6.57	0.09				

----ROW D----

NO GENERATORS		TOP GENERATOR		BOTH GENERATORS	
X/Y3	P/P3	X/Y3	P/P3	X/Y3	P/P3
2.95	0.35	2.95	0.38	2.95	0.37
5.00	0.17	5.00	0.18	5.00	0.59
5.88	0.15	5.88	0.16	5.88	0.25
6.76	0.11	6.76	0.31	6.76	0.20

----ROW E----

NO GENERATORS		TOP GENERATOR		BOTH GENERATORS	
X/Y3	P/P3	X/Y3	P/P3	X/Y3	P/P3
4.32	0.20	4.32	0.24	4.32	0.52
6.08	0.09	6.08	0.26	6.08	0.12
6.96	0.06	6.96	0.17	6.96	0.09

TABLE 14 P/P3 0 DEG AFT BODY SUBSTITUTE GAS

----ROW A----

NO GENERATORS		TOP GENERATOR		BOTH GENERATORS	
X/Y3	P/P3	X/Y3	P/P3	X/Y3	P/P3
2.92	0.72	2.92	0.71	2.92	0.71
3.75	0.50	3.75	0.52	3.75	0.81
4.58	0.50	4.58	1.10	4.58	1.20
5.63	0.44	5.63	0.70	5.63	0.69
6.67	0.21	6.67	0.29	6.67	0.34
7.50	0.14	7.50	0.19	7.50	0.21
8.33	0.12	8.33	0.14	8.33	0.16

----ROW B----

NO GENERATORS		TOP GENERATOR		BOTH GENERATORS	
X/Y3	P/P3	X/Y3	P/P3	X/Y3	P/P3
3.96	0.46	1.25	1.02	1.25	1.04
4.79	0.52	3.96	0.65	3.96	1.04
5.83	0.37	4.79	1.26	4.79	1.23
6.67	0.20	5.83	0.64	5.83	0.61
7.50	0.18	6.67	0.24	6.67	0.33
9.17	0.09	7.50	0.26	7.50	0.24
		9.17	0.09	9.17	0.10

----ROW C----

NO GENERATORS		TOP GENERATOR		BOTH GENERATORS	
X/Y3	P/P3	X/Y3	P/P3	X/Y3	P/P3
2.71	0.89	2.71	0.78	2.71	0.79
3.75	0.53	3.75	0.54	3.75	1.11
4.58	0.58	4.58	1.15	4.58	1.29
5.42	0.50	5.42	0.86	5.42	0.94
6.25	0.21	6.25	0.37	6.25	0.37
7.50	0.20	7.50	0.23	7.50	0.21

----ROW D----

NO GENERATORS		TOP GENERATOR		BOTH GENERATORS	
X/Y3	P/P3	X/Y3	P/P3	X/Y3	P/P3
0.83	1.04	0.83	1.02	0.83	1.01
3.12	0.63	3.12	0.61	3.12	0.59
		4.37	1.20	4.37	1.85
5.21	0.59	5.21	1.01	5.21	0.93

----ROW E----

NO GENERATORS		TOP GENERATOR		BOTH GENERATORS	
X/Y3	P/P3	X/Y3	P/P3	X/Y3	P/P3
2.08	0.70	2.08	0.78	2.08	0.77
3.75	0.54	3.75	0.54	3.75	1.16
4.79	0.53	4.79	0.93	4.79	0.75

TABLE 15 P/P3 0 DEG AFT BODY COMBUSTION GAS

----ROW A----

NO GENERATORS		TOP GENERATOR		BOTH GENERATORS	
X/Y3	P/P3	X/Y3	P/P3	X/Y3	P/P3
2.08	0.74	4.58	1.02	4.58	0.88
4.58	0.52	6.67	0.30	6.67	0.28
6.67	0.24	7.50	0.20	7.50	0.24
7.50	0.24				

----ROW B----

NO GENERATORS		TOP GENERATOR		BOTH GENERATORS	
X/Y3	P/P3	X/Y3	P/P3	X/Y3	P/P3
1.25	1.00	3.96	0.58	3.96	0.78
3.96	0.58	4.79	1.13	4.79	0.92
4.79	0.59	5.83	0.55	5.83	0.49
6.67	0.23	6.67	0.34	6.67	0.36
7.50	0.14	7.50	0.18	7.50	0.20

----ROW C----

NO GENERATORS		TOP GENERATOR		BOTH GENERATORS	
X/Y3	P/P3	X/Y3	P/P3	X/Y3	P/P3
2.71	0.80	4.58	1.02	3.75	0.84
3.75	0.59	5.42	0.89	5.42	0.76
4.58	0.59	6.25	0.42	6.25	0.37
5.42	0.48	7.50	0.18	7.50	0.16
6.25	0.27				
7.50	0.16				

----ROW D----

NO GENERATORS		TOP GENERATOR		BOTH GENERATORS	
X/Y3	P/P3	X/Y3	P/P3	X/Y3	P/P3
5.21	0.57	7.50	0.18	3.12	0.57

----ROW E----

NO GENERATORS		TOP GENERATOR		BOTH GENERATORS	
X/Y3	P/P3	X/Y3	P/P3	X/Y3	P/P3
2.08	0.68	7.50	0.18	3.75	1.30
3.75	0.57			4.79	0.82

TABLE 16 P/P3 20 DEG AFT BODY SUBSTITUTE GAS 2

X/Y3	Z/Y3	NO GENERATOR P/P3	TOP GENERATOR P/P3
4.31	-.338	.231	
5.29	-.459	.153	.143
5.48	1.328	.097	.319
5.87	.338		.389
6.26	-1.328		.104
6.85	-.495		.094

of the nozzle exit and, when scaled by P5 and compared to the scaled pressure without the separators, did not show any significant changes. Note that the active gauge area is large compared to the wake for this X/Y_3 location.

Cowl pressure measurements were attempted using the combustion gas with nozzle separators. However, the first run in this configuration had a very large ignition delay and all of the gauges were destroyed without yielding useful data. These were the only gauges provided in this pressure range and we could not continue with this measurement.

IMPACT PRESSURE MEASUREMENTS

We were unable to obtain meaningful impact pressure measurements because of the large size of our probe relative to this nozzle. We suggest future free-stream measurements of this type be made with a Laser Doppler Velocimeter system, since it does not require a probe which disturbs the flow.

HEAT TRANSFER DATA

Distributions of heating rates for both substitute gas and combustion products on the 20° afterbody show fairly good agreement with the turbulent predictions calculated for us by NASA using the program of Price and Harris (Ref. 11). All runs made with combustion products burned out many heat transfer gauges because the high heating rates gave rise to gauge temperatures high enough to melt the solder holding the leads to the gauge. Gauge destruction was particularly bad close to the nozzle exit for the 0^0 afterbody case, and in areas where the cowl and or side shock crossed the model. Even in cases where a gauge was destroyed by the run, useful measurements were obtained as long as the gauge was intact for the greater part of the test time. The high attrition rate curtailed our testing of the 0° afterbody with combustion gas; however, enough points were taken on the 0° afterbody to show the cowl shock location and to supply an increased basis for correlation of heating rates between combustion and substitute gases.

All of our testing was performed at a single Reynolds number, matched to the flight of a vehicle with a nozzle height of 30.5 cm (1 ft), for Mach 6 flight at a nominal altitude of 24,207 m (79,400 ft). Our tests were 1/20th scale. Because the Reynolds numbers are matched and the gas properties and Mach number distributions are matched for the combustion case, one can expect measured Stanton number (i.e.,

·q/ρu ΔT) to be the same as flight if the ratio of wall temperature to flow total temperature is matched (Ref. 1). Wall temperature effects will be discussed below. For matched Stanton number (in the high Mach number, high gas temperature cases of interest) one calculates flight absolute heating rates by dividing measured model heating rates by the ratio of flight to model dimensions to correct for the density ratio. This is because Reynolds number invariance requires the product ρ D to be invariant between model and flight.

In order to show a comparison between substitute and combustion gas data, the levels shown in Figs. 74 and 62–78 are levels measured on the model which have been normalized by 388 cal/cm^2 sec for the combustion data and the Price and Harris prediction. The substitute gas data have been normalized by 2.71 cal/cm^2 sec. The 388 cal/cm^2 sec value was chosen as a convenient scale factor while the 2.71 cal/cm^2 sec value was computed from the 388 cal/cm^2 sec divided by an average of combustion data points, multiplied by an average of substitute data for the same locations.

Figures 62–66 show the distribution for the 20° afterbody with no generator. The agreement between the combustion data and prediction is quite good considering the expected accuracy of heat transfer data in this range and the nature of turbulent heating predictions in general. The substitute gas data agree with both the combustion data and the prediction in shape (the average levels are forced to agree by the scaling used). Heat transfer distributions for the 20° afterbody with the cowl generator are given in Figs. 67–71. In this case the solid curve is intended for reference only since it does not consider any shocks. The arrival of the cowl shock for the 2-D prediction ($\overline{X}$ = 5.63) is very close to the substitute gas arrival ($\overline{X}$ = 5.68) and somewhat ahead of the combustion gas arrival ($\overline{X}$ = 5.87). In Figs. 72–75 the distributions for the 20° afterbody indicate a "merging" of the cowl and side shock at their intersection. The intersection of these shocks (Fig. 73) gives rise to the highest combustion gas heating rate measured on the 20° afterbody model (1358 cal/cm^2 sec). The heat transfer data for the 20° afterbody are presented in tabular form as a function X/Y_3 in Tables 17 and 18.

The heating rates for the 0° afterbody obtained in both substitute and combustion gases appear in Tables 19 and 20. Data for the 0° afterbody with the combustion gas are somewhat sparse due to the aforementioned gauge destruction problems. However, the cowl shock impingement location for the combustion case is again seen to be aft
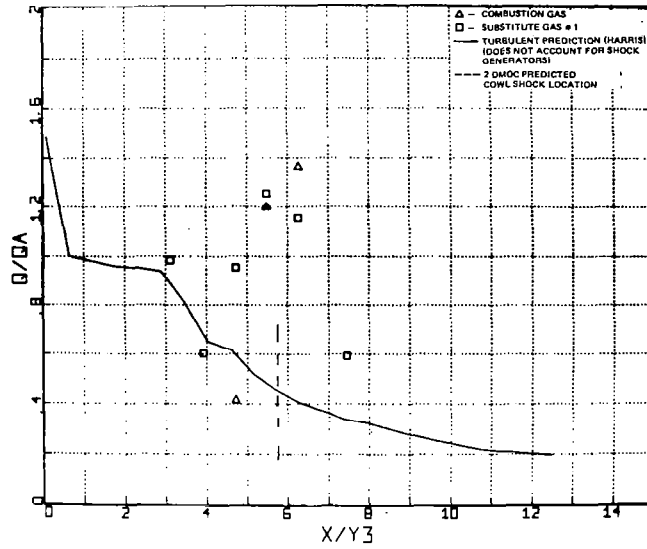
Fig. 74   Heat Transfer Rate Distribution, 20° Afterbody, with
Top and Side Shock Generators, Row C
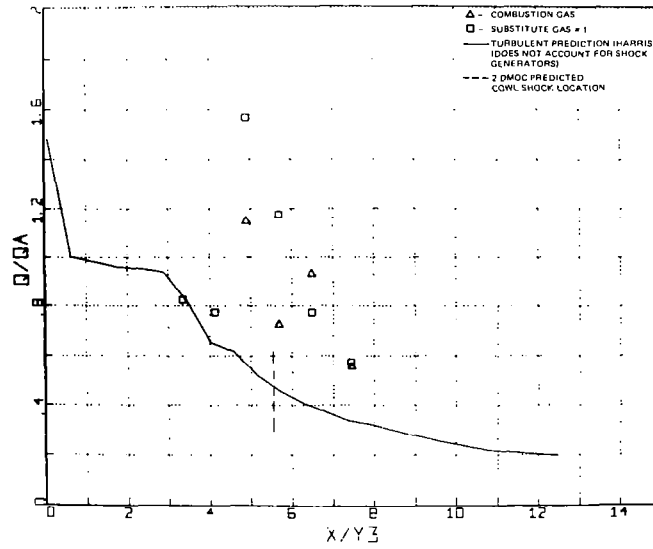
Fig. 75   Heat Transfer Rate Distribution, 20° Afterbody, with
Top and Side Shock Generators, Row D

65
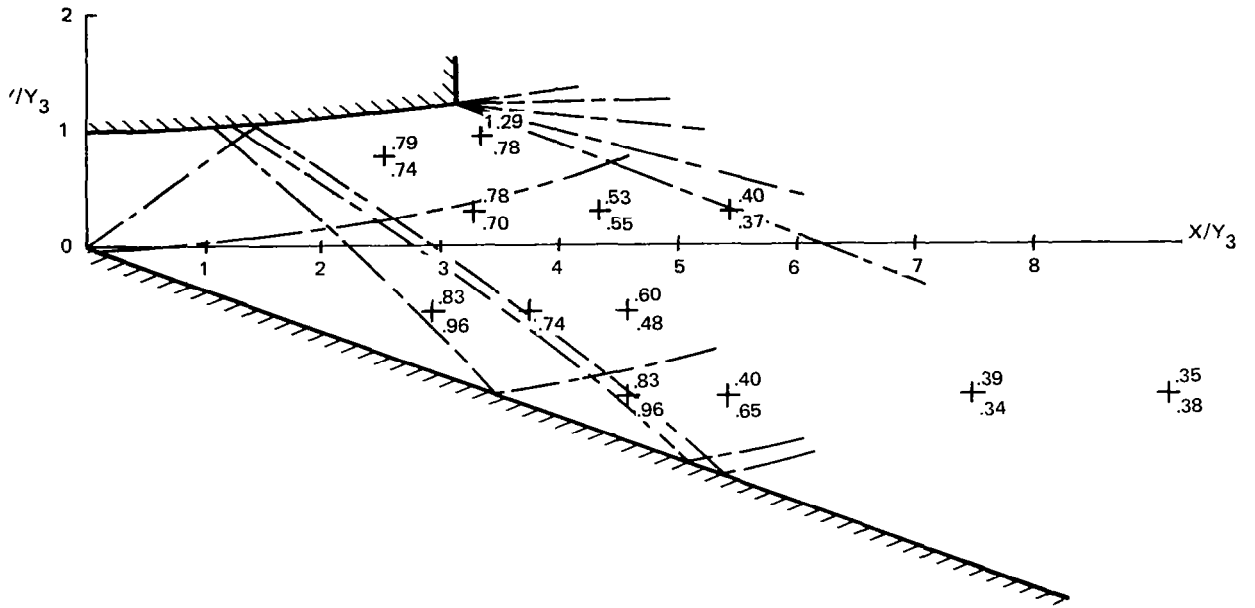
Fig. 76 Reflection Plane Normalized Heating Rates (Q/QA), 20° Afterbody, No Shock Generators (Combustion Data Above Substitute Data)
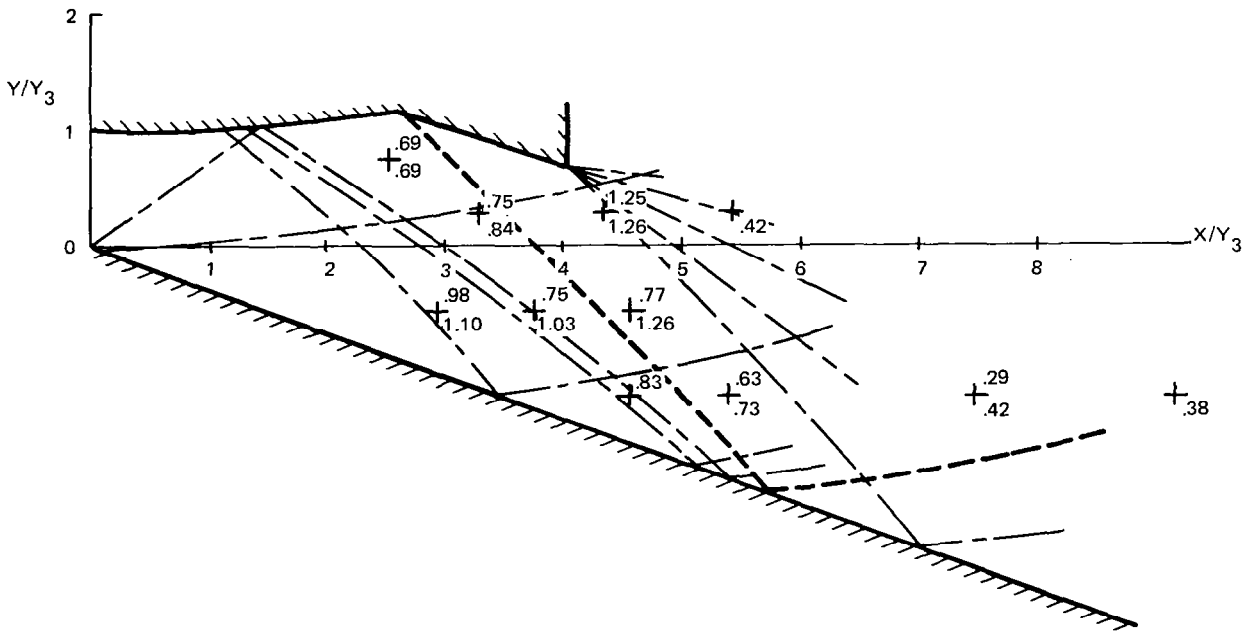
Fig. 77 Reflection Plane Normalized Heating Rates (Q/QA), 20° Afterbody, with Top (Cowl) Shock Generator (Combustion Data Above Substitute Data)

66
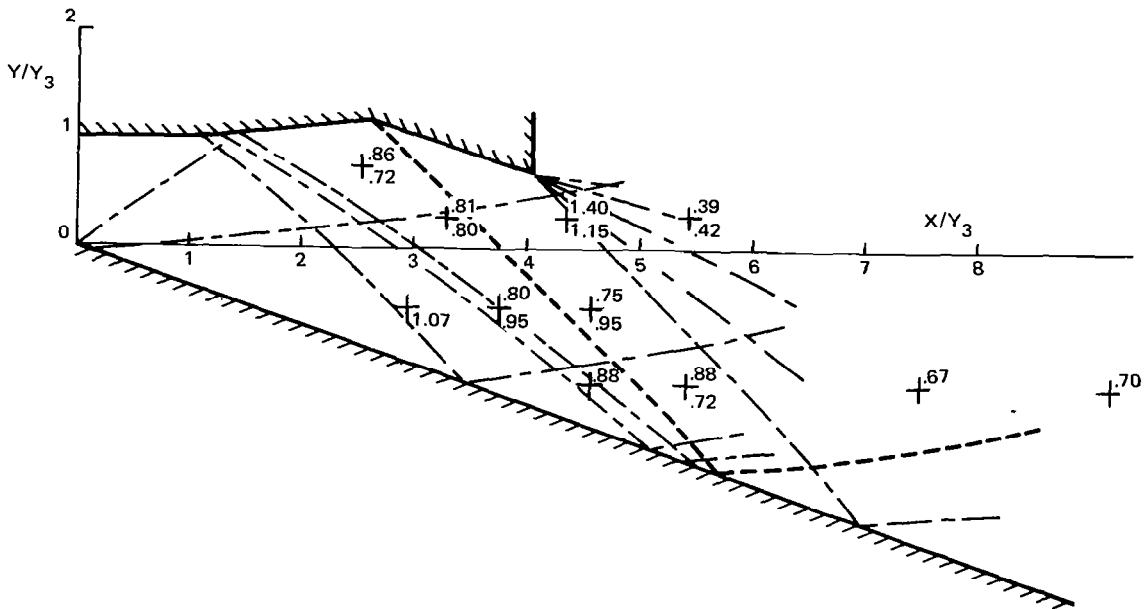
Fig. 78 Reflection Plane Normalized Heating Rates (Q/QA), 20° Afterbody, with Top and Side Generators
(Combustion Data Above Substitute Data)

TABLE 17 Q/QA 20 DEG AFT BODY COMBUSTION GAS
(QA = 388. cal/cm^2 sec)

----ROW A----

NO GENERATORS		TOP GENERATOR		BOTH GENERATORS	
X/Y3	Q/QA	X/Y3	Q/QA	X/Y3	Q/QA
3.53	0.76	3.53	0.61	5.10	0.50
5.10	0.42	5.10	0.45	5.88	0.71
5.88	0.35	5.10	0.51	7.45	1.19
7.45	0.30	5.88	0.95	9.01	0.70
9.01	0.21	7.45	0.59		
		9.01	0.39		

----ROW B----

NO GENERATORS		TOP GENERATOR		BOTH GENERATORS	
X/Y3	Q/QA	X/Y3	Q/QA	X/Y3	Q/QA
3.73	0.82	4.51	0.65	4.51	0.53
5.29	0.45	5.29	0.66	5.29	0.54
6.08	0.22	5.29	0.57	6.08	3.50
7.45	0.24	6.08	1.04	7.45	0.89
		7.45	0.99		

----ROW C----

NO GENERATORS		TOP GENERATOR		BOTH GENERATORS	
X/Y3	Q/QA	X/Y3	Q/QA	X/Y3	Q/QA
3.11	0.82	4.71	0.50	4.71	0.41
3.92	0.81	5.49	0.37	5.49	1.20
4.71	0.53	6.27	1.29	6.27	1.36
5.49	0.39	7.45	0.72		
7.45	0.21				

----ROW D----

NO GENERATORS		TOP GENERATOR		BOTH GENERATORS	
X/Y3	Q/QA	X/Y3	Q/QA	X/Y3	Q/QA
3.34	0.79	4.90	0.49	4.90	1.15
4.12	0.82	5.69	0.40	5.69	0.72
5.69	0.39	5.69	0.32	6.47	0.93
		6.47	1.11	7.45	0.55

----ROW E----

NO GENERATORS		TOP GENERATOR		BOTH GENERATORS	
X/Y3	Q/QA	X/Y3	Q/QA	X/Y3	Q/QA
3.53	0.86	5.10	0.56		
5.88	0.44	5.88	0.48		
		6.66	0.58		

TABLE 18 Q/QA 20 DEG AFT BODY SUBSTITUTE GAS

$$(QA = 2.71 \text{ cal/cm}^2 \text{ sec})$$

----ROW A----

NO GENERATORS		TOP GENERATOR		BOTH GENERATORS	
X/Y3	Q/QA	X/Y3	Q/QA	X/Y3	Q/QA
3.53	0.68	3.53	0.65	3.53	0.66
5.10	0.42	5.10	0.38	5.10	0.42
5.88	0.45	5.88	0.76	5.88	0.96
6.67	0.25	7.45	0.59	7.45	1.02
9.01	0.20	9.01	0.33	9.01	0.65

----ROW B----

NO GENERATORS		TOP GENERATOR		BOTH GENERATORS	
X/Y3	Q/QA	X/Y3	Q/QA	X/Y3	Q/QA
2.95	0.89	2.95	0.70	2.95	0.81
3.73	0.76	3.73	0.66	3.73	0.85
4.51	0.48	4.51	0.49	4.51	0.55
5.29	0.42	5.29	0.38	5.29	0.84
6.08	0.35	6.08	0.97	6.08	1.42
7.45	0.32	7.45	0.67	7.45	0.95

----ROW C----

NO GENERATORS		TOP GENERATOR		BOTH GENERATORS	
X/Y3	Q/QA	X/Y3	Q/QA	X/Y3	Q/QA
3.11	0.94	3.11	0.95	3.11	0.98
3.92	0.68	3.92	0.64	3.92	0.60
4.71	0.59	4.71	0.54	4.71	0.95
5.49	0.44	5.49	0.50	5.49	1.26
6.27	0.40	6.27	0.77	6.27	1.15
7.45	0.27	7.45	0.58	7.45	0.59

----ROW D----

NO GENERATORS		TOP GENERATOR		BOTH GENERATORS	
X/Y3	Q/QA	X/Y3	Q/QA	X/Y3	Q/QA
3.34	0.76	3.34	0.72	3.34	0.82
4.12	0.55	4.12	0.48	4.12	0.77
4.90	0.33	4.90	0.38	4.90	1.57
5.69	0.32	5.69	0.61	5.69	1.17
6.47	0.31	6.47	0.62	6.47	0.77
7.45	0.23	7.45	0.59	7.45	0.57

----ROW E----

NO GENERATORS		TOP GENERATOR		BOTH GENERATORS	
X/Y3	Q/QA	X/Y3	Q/QA	X/Y3	Q/QA
3.53	0.90	6.67	0.43	3.53	1.27
5.88	0.51	7.45	0.59	5.88	0.75

TABLE 19 Q 0 DEG AFT BODY COMBUSTION GAS

NO GENERATORS		----ROW B---- TOP GENERATOR	
X/Y3	CAL	X/Y3	CAL
2.29	603.00	4.79	537.00
3.13	595.00	5.63	693.00
3.96	387.00	6.46	374.00
4.79	539.00	7.29	241.00
5.63	347.00		
6.46	262.00		
6.46	274.00		
7.29	182.00		
7.29	181.00		

NO GENERATORS		----ROW C---- TOP GENERATOR	
X/Y3	CAL	X/Y3	CAL
2.50	613.00	5.00	867.00
5.00	494.00	5.83	619.00
5.83	386.00	7.71	180.00
7.71	134.00		
7.71	132.00		

NO GENERATORS		----ROW D---- TOP GENERATOR	
X/Y3	CAL	X/Y3	CAL
1.67	651.00	4.37	421.00
2.71	602.00	5.21	960.00
3.54	534.00	6.25	287.00
4.37	320.00		
5.21	517.00		
6.25	256.00		
6.25	266.00		
7.50	129.00		
7.50	139.00		

TABLE 20 Q 0 DEG AFT BODY SUBSTITUTE GAS

```
                             ----ROW A----
NO GENERATORS                 TOP GENERATOR          BOTH GENERATORS
  X/Y3          CAL          X/Y3          CAL         X/Y3          CAL
                             2.08          3.83        2.08          4.76
                             2.92          3.48        2.92          4.35


                             ----ROW B----
NO GENERATORS                 TOP GENERATOR          BOTH GENERATORS
  X/Y3          CAL          X/Y3          CAL         X/Y3          CAL
  2.29          4.89        2.29          4.89        2.29          4.78
  3.13          4.13        3.13          3.89        3.13          3.77
  3.96          2.80        3.96          2.93        3.96          2.96
  4.79          3.26        4.79          6.44        4.79          4.89
  5.63          2.39        5.63          3.40        5.63          3.67
  6.46          1.68        6.46          2.36        6.46          2.07
  7.29          1.01        7.29          1.25        7.29          1.20


                             ----ROW C----
NO GENERATORS                 TOP GENERATOR          BOTH GENERATORS
  X/Y3          CAL          X/Y3          CAL         X/Y3          CAL
  2.50          3.97        2.50          4.18        2.50          4.10
  3.33          3.78        4.17          3.48        3.33          3.04
  4.17          2.15        5.00          5.05        4.17          4.02
  5.00          2.72        5.83          2.72        5.00          5.84
  5.83          1.68        7.71          1.00        5.83          3.37
  7.71          0.98                                  7.71          1.36


                             ----ROW D----
NO GENERATORS                 TOP GENERATOR          BOTH GENERATORS
  X/Y3          CAL          X/Y3          CAL         X/Y3          CAL
  1.67          4.24        1.67          3.96        2.71          3.32
  2.71          3.48        2.71          3.32        3.54          3.42
  3.54          2.69        3.54          2.47        4.37          7.15
  4.37          2.42        4.37          3.51        5.21          5.76
  5.21          3.15                                  6.25          4.02
  6.25          1.71        5.21          4.54        7.50          0.33
  7.50          0.90        6.25          2.09
                           7.50          0.98
```

of the location given by both 2-D prediction and the substitute gas, as was the case with 20° afterbody. The same merging of shocks, as with the 20° afterbody, is indicated by the data.

As can be seen from all of these data, the heating rates in the combustion products are very high. For the 20° afterbody shock free case (the configuration most closely resembling the actual flight article), calculated heating rates in the vicinity of the nozzle exit are on the order of 300 cal/cm^2 sec (53 BTU/ft^2 sec) on a full scale vehicle. Corresponding zero degree model rates (6000 cal/cm^2 sec) are too high to measure. Near the intersection of the shocks from the cowl and side genera-ʒ tors the rates go as high as 1358 cal/cm^2 sec on the model, or 68 cal/cm^2 sec on the.cle. full scale vehicle.

NOZZLE SEPARATOR WAKES

In order to study the effect of nozzle separators on the heat transfer distribution a series of experiments was made using the no. 2 substitute and combustion gases. The first of these experiments was made without the nozzle separators in order to extablish a basis for comparison. Heat transfer data were obtained at locations closer to the nozzle exit than in the previous work. These data, when plotted against Z/Y_3, Fig. 79a, show a depression of heating rates for both gases toward the nozzle corners. We believe that these depressed rates indicate vorticies formed by nozzle corner flows and are probably responsible for the early departure from 2-D behavior noted in our $M_\infty = 8$ experiments (Ref. 2).

The flow on the internal nozzle side wall is generally at a higher pressure than the flow on the floor at the same streamwise station. When this occurs in a supersonic flow, there must be a crossflow leakage in the streamwise corner boundary layer, from the sidewall out across the floor of the nozzle. The surface streamlines on the afterbody are therefore likely to be inclined toward the centerline at the spanwise corners of the nozzle exit. Since the Mach waves emanating from the ends of the nozzle side walls travel relative to the local streamlines, it seems likely that this process could produce the observed reduction in pressure below the two-dimensional case ahead of the Mach wave emanating from an undeflected streamline. This postulate is reinforced by the behavior of tests with extended side plates, in which the two-dimensional region was extended by the plates, but the infiltration of the lateral expansion was much more rapid at the end of the extended plates than it had been for the case of the nozzle alone. In this case the corner crossflow would get
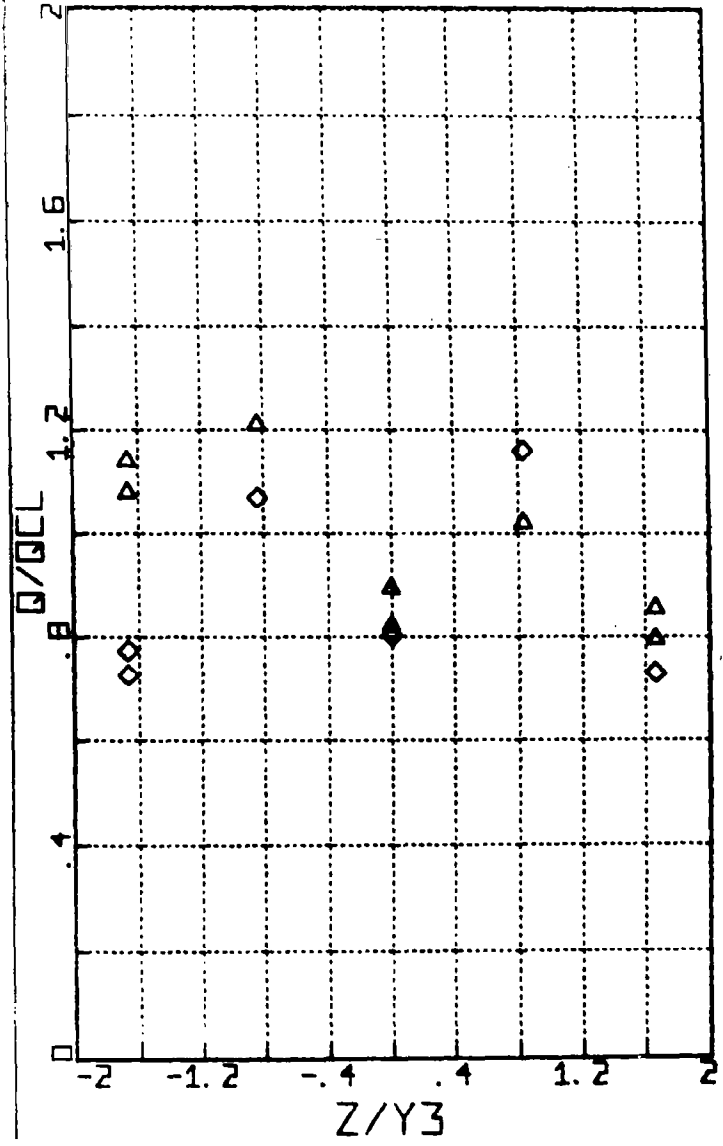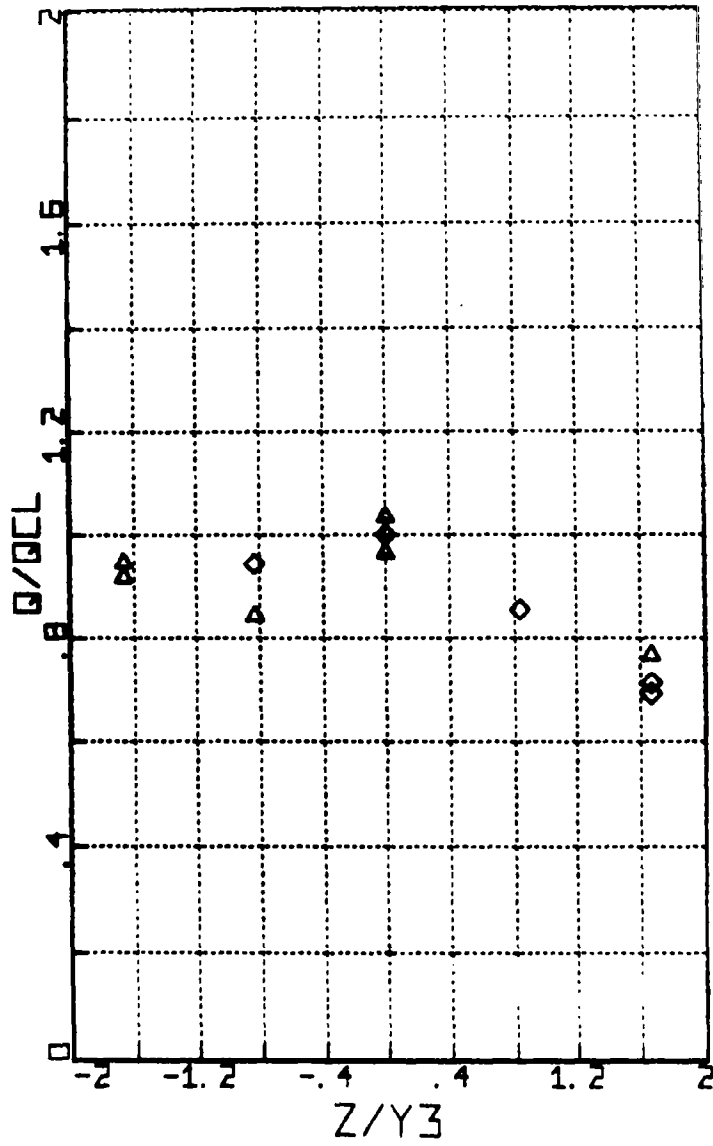
Fig. 79 Heat Transfer Rate Distribution, 20° Afterbody, Q/Q_{C_L} vs. Z/Y_3

much stronger along the plates because the floor (afterbody ramp) pressure is greatly reduced by the 20° turn at the nozzle exit.

The data without separators also show a difference between the No. 2 substitute and combustion gas heating rates. The difference is apparent in Fig. 80 for the row of gauges at $X/Y_3 = 0.781$, a location just aft of the nozzle exit. For this first row of heat transfer instrumentation the combustion gas heating rates are lower than either the No. 1 substitute gas rates or the turbulent Price and Harris prediction. Our first thought on this phenomenon was that we had vibrational freezing of N_2 with the combustion gas so we made calculations of that effect. Although the amount of energy in vibration is probably enough to account for the effect (30% of the gas enthalpy), the relaxation time for N_2 in the presence such large quantities of H_2O is not long enough. The relaxation time would have to be on the order of 10μ sec rather than the calculated levels of 2μ sec). A second explanation of the observed data is that there is a difference in the tendency toward relaminarization of the turbulent boundary layer under the influence of the strong favorable pressure gradient at the intersection of the nozzle exit and the 20° afterbody.

Several authors (Kearney, et al, Ref. 12) have found that the Stanton number of incompressible flows is reduced markedly by local zones of favorable pressure gradient. Kearney, et al, show that the reduction is truly local, in that for the case they studied the Stanton number returned rapidly to the flat plate level (as if there had been no upstream favorable gradient section) downstream of point at which the pressure gradient was again zero. This behavior is remarkably similar to that of the combustion gas relative to the substitute gas, the accepted critical value of the relaminarization parameter $(K \equiv \frac{-\nu}{u^3 \rho} \frac{dp}{dx})$ is 3.7×10^{-6}. This was established by S. Kline in 1967, since endorsed by many (e.g., Ref. 12). At this critical value the "violent eruptions away from the wall near the edge of this viscous sublayer ceased when $K = 3.7 \times 10^{-6}$." Even at values less than critical, skin friction and heat transfer levels have been shown to drop well below their corresponding flat plate levels (Refs. 12, 14).

Three new questions are posed by our measurements: 1) what is the effect of compressibility on relaminarization criteria? 2) what is the effect of an impulsive change in pressure level, rather than a finite section of finite pressure gradient? 3) what is the effect of cooling or relaminarization? Without pretending to answer

ROW C NO GENERATOR
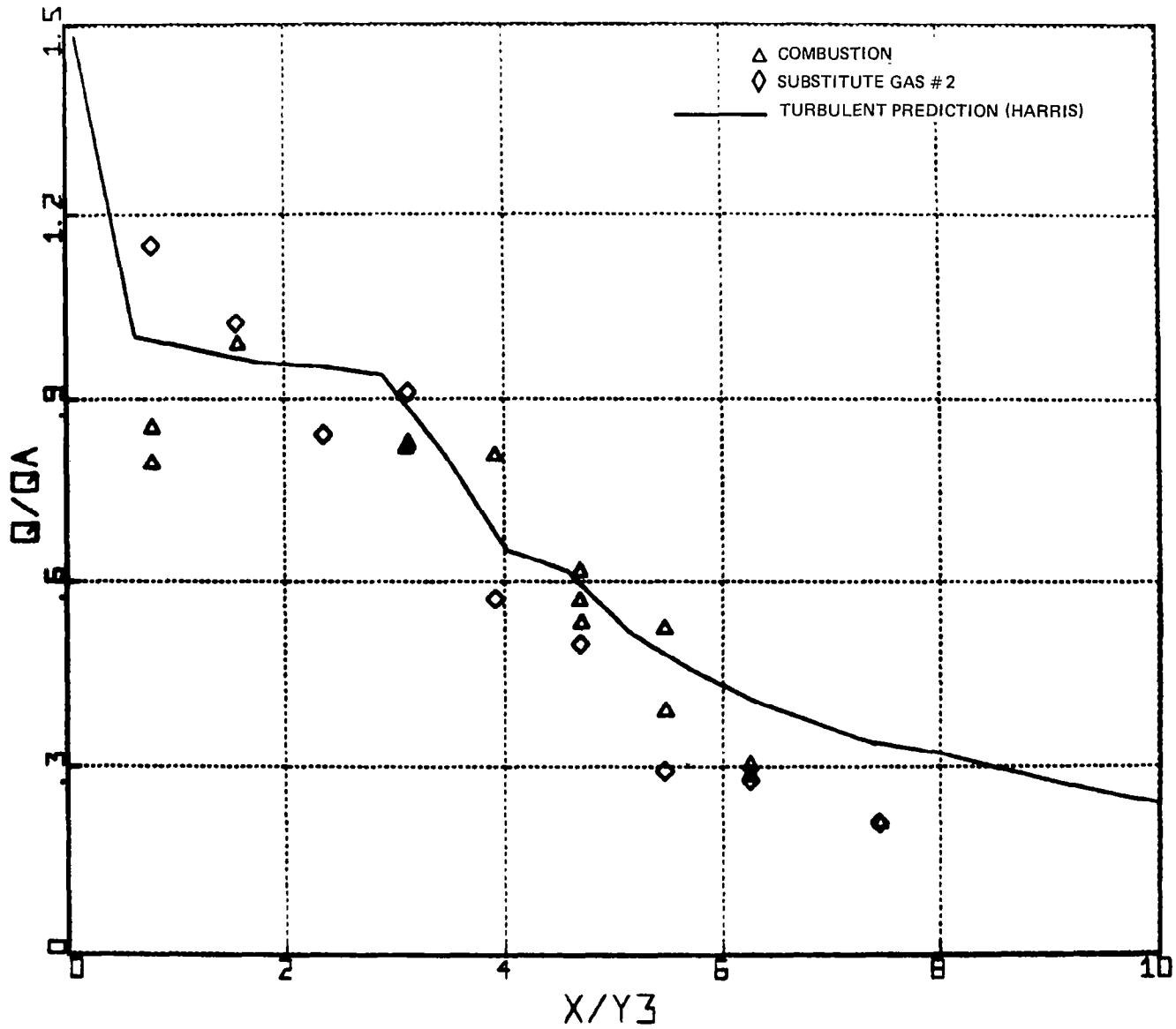
Fig. 80 Heat Transfer Rate Distribution, 20° Afterbody, Q/Q_A vs X/Y_3

these questions, we do know that there is ample precedent for cooling of high Mach number boundary layers delaying transition, which is also a phenomenon related to the bursts of turbulence referred to above. We also know that the similitude requirements of our testing ensure that K is invariant among all three cases: flight, combustion and substitute gases, because K can be written as

$$K = \frac{1}{R_e} \frac{d\ (p/q)}{d\ (X/D)}$$

In view of the above discussion, it is reasonable to postulate that the substantial reduction in heating rate at the start of the afterbody expansion seen for the combustion gas is primarily due to the effect of wall cooling in enhancing the proven ability of favorable pressure gradients in reducing turbulent transport phenomena. It is probably due only in small part to slow relaxation of N_2 vibrational states, because the water vapor concentration is high enough to make that process more rapid than the observed decay. These postulates should be verified by future testing, as the correct understanding of cause and effect will have a large effect on the required thermal protection on a scramjet afterbody.

The addition of nozzle separators has the effect of reducing the area ratio of the individual nozzle sections. This in turn increases the exit Mach number and lowers the exit density. All plotted separator heating rates have been scaled upward by the ratio of exit plane density without separators to exit plane density with separators so that comparisons can be made to the experiments without separators. The tabulated data have not been adjusted to account for this effect. It should be noted that the change in area ratio is different for the individual, nozzle channels. For instance, the center section of the nozzle with the separators placed to divide it into three sections has a density 18% lower than the outer sections. The data in Fig. 79b show the heating rate distribution versus spanwise distance (Z/Y_3) for this configuration. Heating rates just downstream of the separators are increased about 20% over their value without separators while the center line values are decreased by nearly 20%. The depression of centerline rates disappears after $X/Y_x = 2.35$, with heating rates returning to values at or above the rates with no segments.

Fig. 81 a, b, c shows the heating rate distribution versus Z/Y_3 relative to nozzle separator for one nozzle separator. These data are scaled by the centerline heating rate at the respective values of X/Y_3 with no nozzle separators. They were
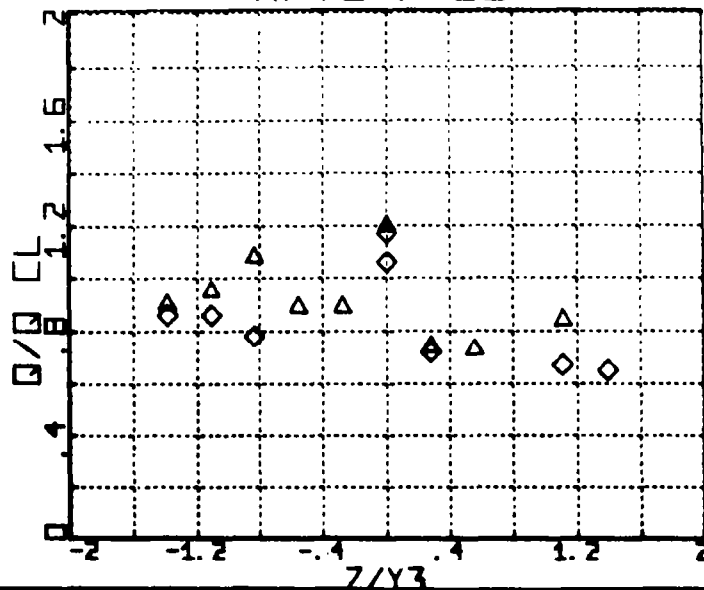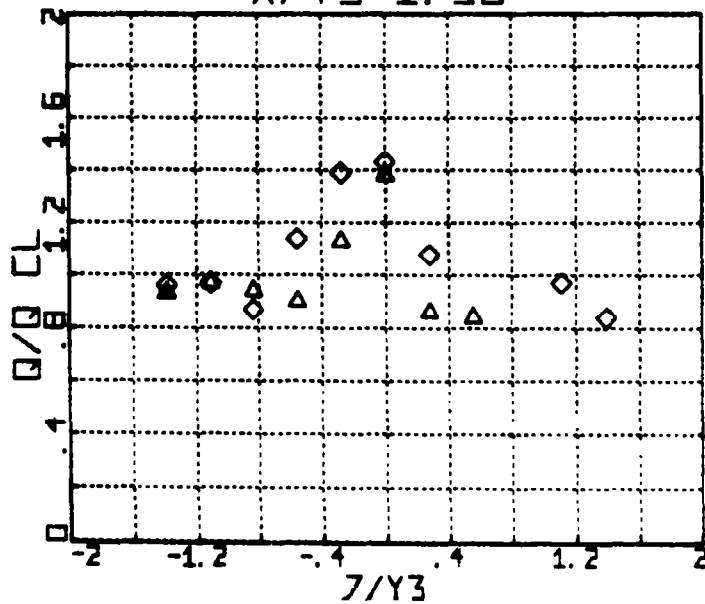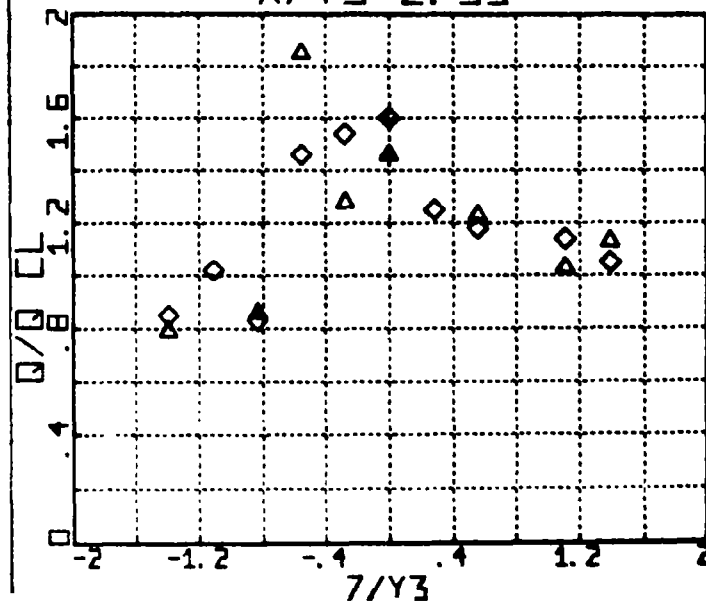
Fig. 81 Heat Transfer Rate Distribution, 20° Afterbody, Q/Q_{C_L} vs Z/Y_3

taken by moving the separator to several slightly different spanwise locations, so that the fixed gauge locations could be at different displacements from the separator. For these tests the density at the exit of each nozzle section is different, causing the wake to turn in the $-Z/Y_3$ direction so it is not surprising that the heat transfer rates in the separator wake regions are not symmetric. The data at $X/Y_3 = 1.76$ and $X/Y_3 = 2.35$ show a definite structure with a maximum heating rate between 20 and 40% higher than the centerline value. The data at $X/Y_3 = 0.781$ do not show a clear-cut structure, but are depressed below their levels without separators. These observations imply that the wake region is very narrow relative to the gauge width at upstream locations and broadens downstream to a resolvable width at the gauge spatial resolution (see previous discussion under Instrumentation in section 2).

The observed peaks of the heating distributions are not always at the separator location but further to the nozzle side. This shift may be caused by the wake turning or may be an artifact of the spatial resolution. The important point is that the measurements show a rapidly varying level of heating; a structure that is consistent with a strong streamwise vortex (or vortex-like crossflow) along the root corners of the separators, spreading slowly as it passes out over the afterbody surface.

In order to investigate the effect of trailing edge bluntness one separator's trailing edge was ground off so that it was 0.508 mm wide, i.e., 4 times the initial width. Figure 82 shows these data plotted against Z/Y_3 relative to the separator position and normalized as before. At X/Y_3 of 1.56 the wake structure is slightly more pronounced than for the same location with the thin trailing edge, while at $X/Y_3 = 2.35$ the rates are lower than in the previous case. The first observation is due to a wake that is wider relative to the gauge size. The lower rates at $X/Y_3 = 2.35$ may be an indication that the maximum relative heating rate now occurs further upstream which would also be a function of increased wake size. The data at $X/Y_3 = 0.781$ are also lower in this case and it not as logical to assume that this is caused by a blunt trailing edge. This effect is probably a relaminarization. If the boundary layer is on the verge of relaminarization any small stabilizing effect could cause it to relaminarize.

The heat transfer data for these nozzle separator wake tests are tabulated as functions of X/Y_3 in Tables 21 through 24.
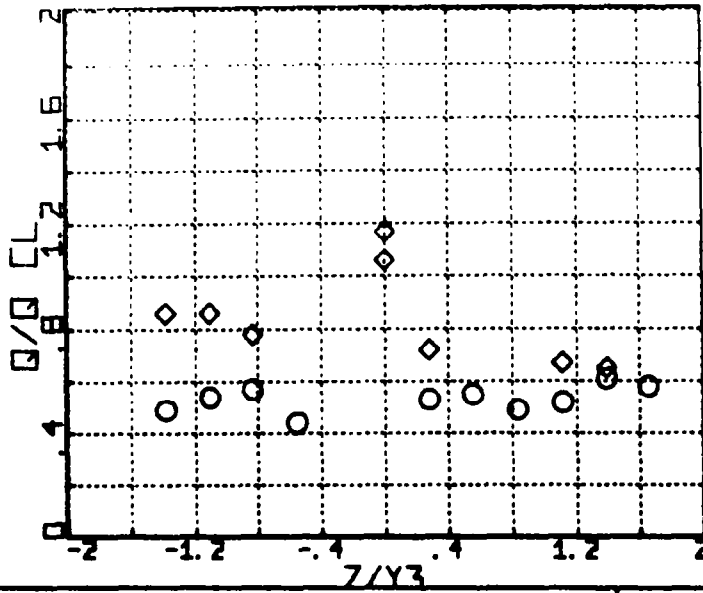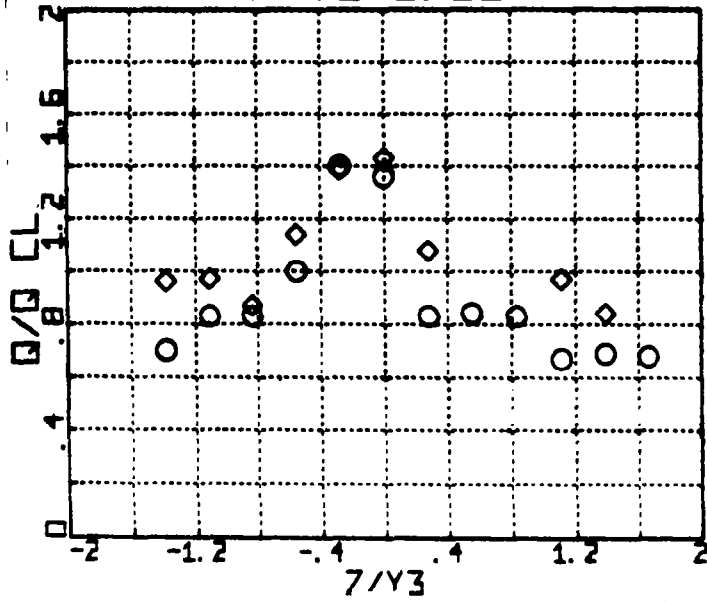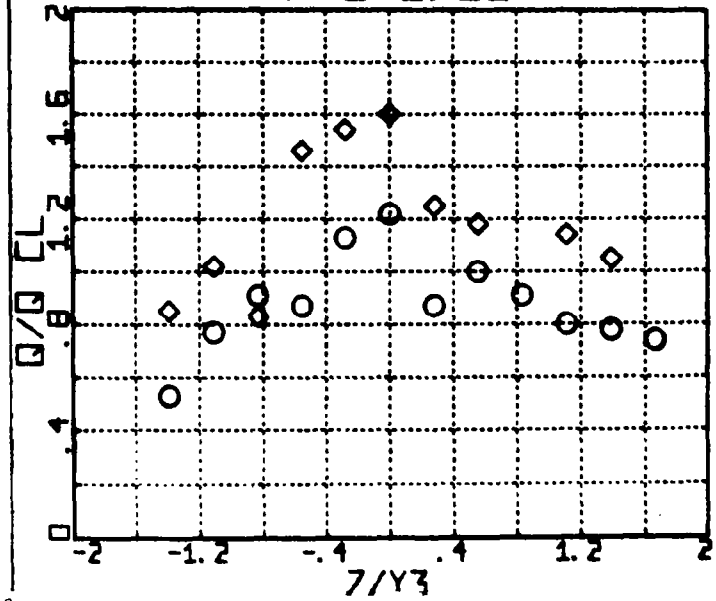
Fig. 82 Heat Transfer Rate Distribution, 20° Afterbody, Blunted Separator, Q/Q_{C_L} vs. Z/Y_3

TABLE 21 Q/QA SUBSTITUTE GAS 2

BOTH SEGMENTS

0.78	0.71
1.57	0.56
1.57	0.54
2.74	0.45
3.53	0.41
3.53	0.45
4.31	0.57
5.09	0.35
5.87	0.32

----ROW A----

BOTH SEGMENTS

0.78	1.06
1.57	1.15
2.35	1.05
2.94	0.62
3.78	0.41
3.78	0.84
4.50	0.43
4.50	0.43
5.29	0.36
6.07	0.39

----ROW B----

BOTH SEGMENTS

0.78	0.66
1.56	0.64
2.35	0.62
3.13	0.92
3.92	0.52
4.70	0.51
5.48	0.36
6.26	0.23
7.44	0.21

----ROW C----

BOTH SEGMENTS

0.78	0.75
0.78	0.96
1.56	0.91
2.35	0.84
3.33	0.54
4.11	0.69
4.11	0.69
5.68	0.66
6.46	0.30

----ROW D----

BOTH SEGMENTS

0.78	0.71
0.78	0.75
1.56	0.75
1.56	0.72
2.35	0.59
2.35	0.58
3.52	0.51
4.31	0.45
4.31	0.34
5.87	0.36
6.66	0.38
6.66	0.34

----ROW E----

TABLE 22 Q/QA COMBUSTION HEATING

----ROW A----

NO SEGMENTS		CENTER SEGMENT		BOTH SEGMENTS	
0.78	0.63	0.78	0.67	0.78	0.61
1.57	0.65	1.57	0.62	0.78	0.56
1.57	0.65	1.57	0.62	1.57	0.44

----ROW B----

NO SEGMENTS		CENTER SEGMENT		BOTH SEGMENTS	
1.57	1.03	0.78	0.66	0.78	0.67
2.35	0.74	1.57	0.77	1.57	1.09
2.35	0.74	2.35	0.79	2.35	0.61

----ROW C----

NO SEGMENTS		CENTER SEGMENT		BOTH SEGMENTS	
0.78	0.85	0.78	0.64	0.78	0.49
0.78	0.79	1.57	1.48	0.78	0.54
1.57	0.99	2.35	0.67	1.57	0.52
3.13	0.83	3.92	0.69	1.57	0.51
4.70	0.62	4.70	0.71	2.35	0.77
4.70	0.57	6.26	0.36	2.35	0.77
5.48	0.52	6.26	0.36	3.13	0.66
6.26	0.30	6.26	0.36	3.92	0.60

----ROW D----

NO SEGMENTS		CENTER SEGMENT		BOTH SEGMENTS	
0.78	0.69	0.78	0.72	0.78	0.79
1.56	1.01	1.56	0.70	1.56	0.75
1.56	1.04	2.35	1.17	2.35	1.06
2.35	0.73	3.33	0.40	3.33	0.45
2.35	0.83	3.33	0.40	3.33	0.45

----ROW E----

NO SEGMENTS		CENTER SEGMENT		BOTH SEGMENTS	
0.78	0.78	0.78	0.65	0.78	0.81
0.78	0.75	1.56	0.67	0.78	0.77
1.56	0.91	2.35	0.39	1.56	0.81
2.35	0.58	2.35	0.39	2.35	0.43

TABLE 23 Q/QA COMBUSTION GAS

SEGMENT @-.274		SEGMENT @ -.552	
0.78	0.74	0.78	0.66
1.57	0.91	0.78	0.73

SEGMENT @-.274		SEGMENT @ -.552	
0.78	0.68	0.78	0.62
0.78	0.58	2.35	0.53
2.35	0.59	2.35	0.53

SEGMENT @-.274		SEGMENT @ -.552	
0.78	0.55	0.78	0.55
0.78	0.53	0.78	0.54
1.57	0.76	1.57	0.77
2.35	0.67	4.70	0.63
3.92	0.56	4.70	0.61
4.70	0.62	5.48	0.34
5.48	0.41	6.26	0.30
6.26	0.28	6.26	0.30

SEGMENT @-.274		SEGMENT @ -.552	
0.78	0.64	0.78	0.65
0.78	0.63	1.56	0.79
1.57	0.87	2.35	0.94
1.57	0.96	3.33	0.63
2.35	0.69	3.33	0.53
3.33	0.55	3.33	0.53
3.33	0.54	3.33	0.53

SEGMENT @-.274		SEGMENT @ -.552	
0.78	0.67	0.78	0.65
0.78	0.64	1.56	0.76
1.56	0.83	1.56	0.81
1.56	0.65	1.56	0.81
2.35	0.37	1.56	0.81

TABLE 24 HEAT TRANSFER RATE SUBSTITUTE GAS 2

----ROW A----

NO SEGMENT		SEGMENT @ -.274		SEGMENT @ -.552	
0.78	0.79	0.78	0.73	0.78	0.66
0.78	0.82	2.74	0.55	2.74	0.50
1.57	0.77	3.53	0.68	3.53	0.60
1.57	0.72	4.31	0.48	4.31	0.37
2.74	0.62	5.09	0.37	5.09	0.33
3.53	0.73	5.87	0.36	5.87	0.32
3.53	0.75	5.87	0.36	5.87	0.32
4.31	0.47	5.87	0.36	5.87	0.32
4.31	0.59	5.87	0.36	5.87	0.32
5.09	0.49	5.87	0.36	5.87	0.32
6.66	0.41	5.87	0.36	5.87	0.32
7.44	0.32	5.87	0.36	5.87	0.32
8.22	0.25	5.87	0.36	5.87	0.32
9.01	0.21	5.87	0.36	5.87	0.32

----ROW B----

NO SEGMENT		SEGMENT @ -.274		SEGMENT @ -.552	
0.78	0.98	0.78	0.68	0.78	0.69
1.57	0.91	1.57	0.79	1.57	0.89
2.35	0.81	2.35	0.81	2.35	0.87
2.94	0.71	2.94	0.78	2.94	0.69
3.72	0.74	4.50	0.39	3.78	0.70
4.50	0.32	5.29	0.47	4.50	0.38
4.50	0.34	6.07	0.33	5.29	0.50
5.29	0.50	6.07	0.33	6.07	0.38

----ROW C----

NO SEGMENT		SEGMENT @ -.274		SEGMENT @ -.552	
0.78	1.15	2.35	0.91	0.78	0.74
1.56	1.02	3.13	0.99	1.56	1.00
2.35	0.84	3.92	0.70	2.35	0.95
3.13	0.91	4.70	0.70	3.92	0.69
3.92	0.57	5.48	0.51	4.70	0.72
4.70	0.50	6.26	0.33	5.48	0.52
5.48	0.29	7.44	0.31	6.26	0.35
6.26	0.28	7.44	0.31	7.44	0.30

----ROW D----

NO SEGMENT		SEGMENT @ -.274		SEGMENT @ -.552	
0.78	1.09	1.56	1.24	0.78	0.42
1.56	0.96	2.35	1.13	1.56	1.04
3.33	0.89	3.33	0.44	2.35	1.09
4.11	0.62	4.11	0.65	3.33	0.86
4.89	0.44	4.89	0.47	4.11	0.68
5.68	0.43	5.68	0.72	4.89	0.52
6.46	0.28	6.46	0.45	5.68	0.62
7.44	0.31	6.46	0.45	5.68	0.62

----ROW E----

NO SEGMENT		SEGMENT @ -.274		SEGMENT @ -.552	
1.56	0.67	0.78	0.86	0.78	0.87
2.35	0.66	1.56	0.86	1.56	0.83
4.31	0.51	2.35	0.74	2.35	0.63
5.09	0.38	3.52	0.81	3.52	0.83
6.66	0.34	4.31	0.49	4.31	0.52
7.44	0.34	5.09	0.43	5.09	0.43
7.44	0.34	5.87	0.39	5.87	0.32
7.44	0.34	6.66	0.51	6.66	0.48

COWL SHOCK IMPINGEMENT LOCATION

The calculation of the cowl shock impingement location showed very little change with gas composition. The data in Fig. 83 show the heat transfer distributions for both substitute gases with the cowl shock generator. These data agree with the calculations and show essentially the same shock location. It should be remembered that the No. 2 substitute gas experiments were made with an extended nozzle side to increase the 2-D region and that this accounts for some of the apparent scatter.

As a result of those experiments and the calculations it is apparent that the aft cowl shock location for the combustion gas is caused either by a relaxation effect (about 1μ sec of relaxation time required) or a shock boundary layer interaction. Which of these two candidates is correct could be determined by changing the combustion gas temperature to see if the cowl shock impingement location moves.

Explaining the difference in shock location between combustion and substitute gases is important, even though it is small in magnitude. We must understand the limitations of the substitute gas method if it is to be used with confidence in development testing. Since it is clear from the above that the differences are not due to small differences in substitute gas properties, we look to boundary layer and nonequilibrium effects for their origin. We believe the answer lies in the effect of wall cooling on shock boundary layer interaction, but it is also possible that there is an effect of finite vibrational relaxation time in the combustion gas that is not present in the substitute gas. The impingement of an incoming shock on a boundary layer has a well characterized pressure distribution, the streamwise extent of which depends on the boundary layer and shock characteristics. The difference in wall cooling between substitute and combustion gas would act to make a separated zone around the impingement more compact in the combustion case by increasing the density in the separated zone. The pressure and heat transfer rises would therefore not extend as far upstream as in the substitute gas case. This explanation is plausible because the shifts in position of the heat transfer rise between combustion and substitute gases are small compared to the streamwise distance over which the rise takes place. Although the cooling effect on separated flows has been observed in previous investigations of cooled separating flows at high Mach number (e.g., Kaufman, et al, Ref. 13), it is quite speculative in this case. Kaufman, et al, found that "In general, cooling the wall delayed separation and reduced its extent, except when the cooling was
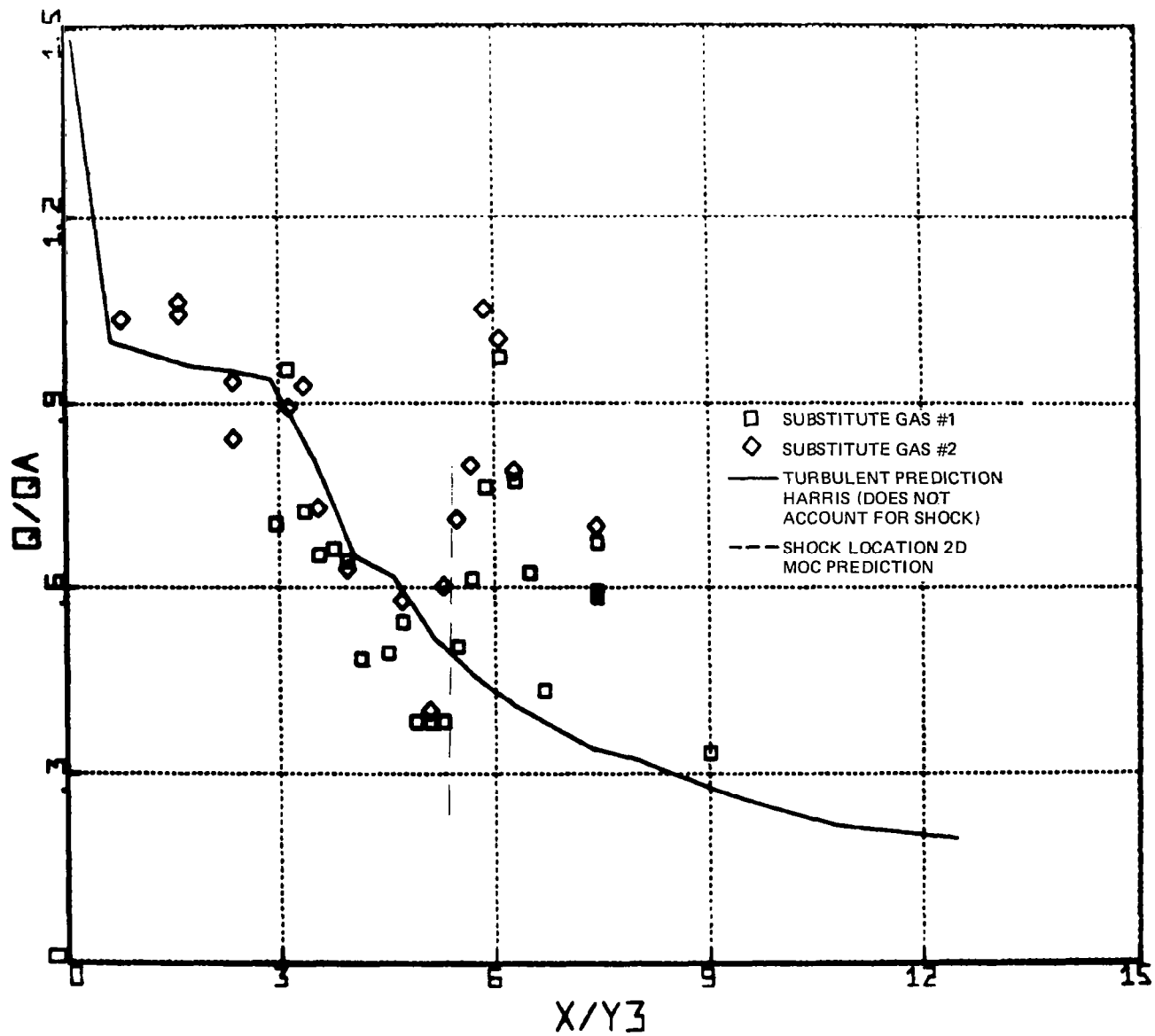
84

Fig. 83 Heat Transfer Rate Distribution, 20° Afterbody, with Top (Cowl) Generators, All Rows

sufficient to change the character of the boundary layer." Their tests were for a configuration very similar to the present shock generator, so the probability also exists that some of the shift in shock location is attributable to the shock generator boundary layer interaction.

6. CONCLUSIONS AND RECOMMENDATIONS

The detonation tube has provided a good simulation of the exhaust flow from a hydrogen/oxygen scramjet engine at a free stream Mach number of 6. Pressure distributions obtained on a cowl and afterbody model with the flow of simulated combustion products and the flow from a substitute gas mixture of 50 percent Argon and 50 percent Freon 13B1 were in good agreement in the two-dimensional regions of the flow.

Extensive heat transfer measurements were in very good agreement with theoretical calculations for a turbulent boundary layer. This is in contrast to our measurements at the $M_\infty = 8$ flight condition (Ref. 2), where the measurements compared well with laminar boundary layer calculations. The extremely high heating rates measured in the present tests should be well noted. Because these data were obtained at full scale Reynolds number and total enthalpy, they can be directly converted to full scale vehicle values by dividing by 20, the model scale factor. They show full scale heating rates the order of 18 cal/cm^2 sec at a distance of 3 combustor exit heights downstream of the combustor exit on the 20° afterbody (as close to the exit as we measured) and close to 70 cal/cm^2 sec further downstream where two artificially generated shocks crossed. Because the actual scramjet vehicle will have several engine modules and the module separators will generate wakes and crossing shocks, we recommended additional testing, more closely duplicating actual vehicle geometry, to determine the effects of such disturbances. Our additional testing showed that separator wakes do have significant effects on the afterbody heating distributions. There were local increases in heating rate as much as 60% above the centerline value with no separators. The peaks were strong gradients in the heating rate which must be accounted for in vehicle design. Furthermore, due to limited spatial resolution, the actual peak heating rates on gradients may be much higher than the indicated values. The experiments suggest that there are vortical crossflows induced

at the corners and that these are responsible for the large changes in the heating distribution. The combination of these vortices and the separator wakes make the actual vehicle afterbody heating distributions difficult to predict. We recommend additional testing with a model equipped with heat transfer instrumentation specially made to give high spatial resolution in both streamwise and spanwise directions. The model should be close to the actual vehicle geometry as possible.

The experiments performed under the extended contract suggest that a greater tendency toward relaminarization of the turbulent boundary layer occurs with rapid expansion of the combustion gas than with the substitute gas. The difference is probably caused by the stabilizing effect of the relatively colder wall in the combustion case. Additional experimentation and calculation along these lines could show the way to reduce the afterbody heating rates on the actual vehicle by confirming that this is the real cause of observed heating rate differences.

One anomaly left unexplained by the first tests at $M_\infty = 6$ was the slight difference in the cowl shock impingement location on the afterbody for the substitute gas compared to the combustion gas. This particular substitute gas mixture was chosen because it was the same as that to be used in a concurrent test program at the NASA Langley Research Center, and our two-dimensional M-O-C calculations showed that it very closely matched the calculated flow field using equilibrium combustion gas products. We recommended that additional calculations and tests be made with slightly modified substitute gas mixtures in order to bring the shock positions into more perfect agreement.

The results of additional experiments and calculations showed that the cowl shock impingement location is only very weakly related to the substitute gas composition. Therefore, the anomaly is not caused by differences in pressure ratio or shock angle. The aft arrival of the combustion gas cowl shock must be caused by either a relaxation effect in the combustion gas or shock boundary layer interaction, which can differ in the two cases because of the wall cooling effect.

We encountered a problem in this test program when we tried to measure impact (Pitot) pressures in the exhaust flows. The purpose of the measurements was to calibrate the flow to further verify the simulation technique. Basically, our probes were too large for the gradients and size of the flow fields and meaningful measurements

couldn't be obtained.   For diagnosing small flow fields such as these we would recommend that non-flow-disturbing instrumentation techniques, such as laser-Doppler-velocimetry, be used.

7. REFERENCES

1. Oman, R., Foreman, K., Leng, J., and Hopkins, H., "Simulation of Hypersonic Scramjet Exhaust," NASA CR-2494, March 1975.

2. Hopkins, H., Konopka, W., and Leng, J., "Validation of Scramjet Exhaust Simulation Technique", NASA CR-2688, June 1976.

3. Dash, S. and DelGuidice, P., "Numerical Methods for the Calculation of Three-Dimensional Nozzle Exhaust Flow Fields," in Aerodynamic Analyses Requiring Advanced Computers, Part I, NASA SP-347, March 1975.

4. Hopkins, H., Konopka, W., Leng, J., and Oman, R., "Simulation Experiments Using Hydrogen/Oxygen Gas Mixtures in a High-Pressure Detonation Tube," NASA CR-128955, 1973.

5. Ratliff, A., Smith, S., and Penny, M., "Rocket Exhaust Plume Computer Program Improvement, Vol. I - Final Report, Summary Volume, Method-of-Characteristics Nozzle and Plume Programs," NASA CR-125601, 1972.

6. Svehla, R. and McBride, B., "FORTRAN IV Computer Program for Calculation of Thermodynamic and Transport Properties of Complex Chemical Systems," NASA TN-D-7056, January 1973.

7. Konopka, W., "Heat Transfer Instrumentation for the Grumman Hypersonic Shock Tunnel," Grumman Research Department Memorandum RM-287, July 1965.

8. Hartunian, R., and Varwig, R., "On Thin-Film Heat-Transfer Measurements in Shock Tubes and Shock Tunnels", The Physics of Fluids, Vol. 5, No. 2, February 1962; also Aerospace Corporation Report TDR-594 (1217-01)TN-2, May 1961.

9. Neer, M., "Autoignition of Flowing Hydrogen-Air Mixtures", AIAA Journal, Vol. 13, No. 7, July 1975, pp 924-928.

10. Gilbert, R. and Strehlow, R., "Theory of Detonation Initiation Behind Reflected Shock Waves", AIAA Journal, Vol. 4, No. 10, October 1966, pp 1777-1783.

11. Price, J. and Harris, J., Computer Program for Solving Compressible Non-similar-Boundary-Layer Equations for Laminar, Transitional, or Turbulent Flows of a Perfect Gas, NASA TM X-2458, April 1972.

12. Kearney, D.W., Kays, W.M., and Moffat, R.J.; "Heat Transfer to a Strongly Accelerated Turbulent Boundary Layer: Some Experimental Results, Including Transpiration," Int'l. J. Heat and Mass Transfer, Vol. 16, pp 1289-1305.

13. Kaufman, L.G. II, Meckler, L., and Hartofilis, S.A.; "An Investigation of Flow Separation and Aerodynamic Controls at Hypersonic Speeds", J. Aircraft, Vol. 3, Nov.-Dec. 1966, pp 555-561.

14. Blaskwelder, R.F., and Kovasznay, L.S.G.; "Large-Scale Motion of a Turbulent Boundary Layer During Relaminarization", J. Fluid Mech, Vol. 53, Part 1, 1972, pp 61-83.

1. Report No.	2. Government Accession No.	3. Recipient's Catalog No.
NASA CR-3003		

4. Title and Subtitle	5. Report Date
Validation of Scramjet Exhaust Simulation Technique at Mach 6	April 1979
	6. Performing Organization Code

7. Author(s)	8. Performing Organization Report No.
H. B. Hopkins, W. Konopka, and J. Leng	RE-547
	10. Work Unit No.
9. Performing Organization Name and Address	505-11-31-02-00
Grumman Aerospace Corporation Bethpage, New York 11714	11. Contract or Grant No.
	NAS1-14152
	13. Type of Report and Period Covered
12. Sponsoring Agency Name and Address	Contractor Report
National Aeronautics and Space Administration Washington, D. C. 20546	14. Sponsoring Agency Code

15. Supplementary Notes
Langley Technical Monitor: James L. Hunt Final Report

16. Abstract

Current design philosophy for hydrogen-fueled, scramjet-powered hypersonic aircraft results in configurations with strong couplings between the engine plume and vehicle aerodynamics. This report describes the experimental verification of the scramjet exhaust simulation devised by Grumman Research. The scramjet exhaust was reproduced for the Mach 6 flight condition by the detonation tube simulator. The exhaust flow pressure profiles, and to a large extent the heat transfer rate profiles, were then duplicated by cool gas mixtures of Argon and Freon 13B1 or Freon 12. Cool substitute gas mixtures such as these could be used in conventional wind tunnels. The results of these experiments indicate that a cool gas simulation of the hot scramjet exhaust is a viable simulation technique except for phenomena which are dependent on the wall temperature relative to flow temperature.

17. Key Words (Suggested by Author(s))	18. Distribution Statement
Engine/Airframe Integration Hypersonics Simulation Scramjet	Unclassified-Unlimited Subject Category 05

19. Security Classif. (of this report)	20. Security Classif. (of this page)	21. No. of Pages	22. Price*
Unclassified	Unclassified	102	$6.50